Response assessment with quantitative FLT PET/CT imaging

By

Matthew Scarpelli

A dissertation submitted in partial fulfillment of

the requirements for the degree of

Doctor of Philosophy

(Medical Physics)

at the

UNIVERSITY OF WISCONSIN-MADISON

2018

Date of oral examination: 11/15/2018

The dissertation is approved by the following members of the Final Oral Committee:

Bradley Christian, Professor, Medical Physics
Sean Fain, Professor, Medical Physics
Robert Jeraj, Professor, Medical Physics
Glenn Liu, Professor, Medicine
Scott Perlman, Professor, Radiology

Table of Contents

Acknowledgements

I am forever grateful for support from lab members, collaborators, friends, and family during my graduate studies. In particular, I am thankful for the advice from former lab members including: Urban Simoncic, Stephen Yip, Vikram Adhikarla, Matt La Fontaine, Peter Scully, Surendra Prajapati, Tyler Bradshaw, Natalie Weisse, Song Chen, Sheng-Li Tzeng, and Stephanie Harmon. I am also thankful for advice from current lab members: Tim Perk, Christie Lin, Alison Roth, Amy Weisman, Peter Ferjancic, Damijan Valentinuzzi, Marusa Turk, Enrique Cuna, Mauro Namias, Victor Fernandez and Daniel Huff.

I am grateful for the insights and ideas generated by my advisor Robert Jeraj and UW physicians and scientists including: Glenn Liu, Scott Perlman, Doug McNeel, Justine Bruce, Samantha Loeber, and Jens Eickhoff. I want to give a special thanks to the WIMR PET imaging staff including: Chris Jaskowiak, Sara Buslaff, Katelin Beaman, Mark McNall, and Will Natividad – for acquiring the PET/CT scans for this dissertation. I also want to thank the UW cyclotron gang for producing the PET tracer and additional support staff who have contributed to this work including: Suzanne Hanson, Jamie Wiepz, Katie Kovacich, and Jennifer Engel-Diaz. Finally, I would like to thank my friends and family for providing continued support and guidance throughout my many years of graduate study.

Abstract

The defining characteristic of malignant tumors is excessive, uncontrolled cell proliferation, suggesting that measurements of cell proliferation would be useful for characterizing tumors and tumor responses to therapy. Molecular imaging with the experimental modality 3'-Deoxy-3'-^{18}F-fluorothymidine (FLT) positron emission tomography (PET) can be used to non-invasively measure longitudinal changes in cell proliferation. The overall goal of this dissertation is to investigate the clinical value of FLT PET as a biomarker of patient response to cancer therapy. It focuses on utilization of FLT PET to improve anti-angiogenic and immunotherapies as they are promising cancer therapies but widespread efficacy has been hindered by acquired or intrinsic resistance to therapy. In this dissertation a methodology for performing dynamic PET scanning and FLT compartmental modelling in clinical studies is developed. Applying this methodology shed new insights relating to the interplay of vascular and proliferative changes occurring in tumors during anti-angiogenic therapy. It was found that increases in tumor cell proliferation occurred during week-long breaks in anti-angiogenic therapy. This led in part to development of a novel treatment paradigm where chemotherapy is applied sequentially during breaks in anti-angiogenic therapy to boost therapeutic efficacy. We tested this novel treatment regimen and found greater decreases in tumor FLT uptake when chemotherapy was applied during anti-angiogenic treatment breaks, indicating sequential chemotherapy enhances the pharmacodynamic effect of anti-angiogenic therapy. In the context of immunotherapy, we found increased FLT PET uptake in draining lymph nodes that provides evidence of regional activation of immune cells. During immunotherapy, changes in FLT uptake in tumors were predictive of time to progression and increased FLT uptake in thyroid lobes was predictive of the occurrence of thyroid-related adverse events. These results strongly support

continued study of FLT PET as imaging biomarker for devising improved therapeutic strategies and as an early predictor of patient response.

Chapter 1: Introduction

1.1 Motivation and specific aims

The promise of precision medicine has been spurred by the identification of new therapeutic targets specific to individual patients. While this has led to many new therapies, it has also increased demand for biomarkers that predict therapeutic efficacy. Development of biomarkers that can reliably assess whether a patient is responding favorably to therapy at early timepoints would facilitate the era of precision medicine, allowing physicians to quickly evaluate whether a targeted therapy should be continued or altered.

The rapid rise in targeted therapies has also made apparent the shortage of available biomarkers for evaluating the mechanistic actions of new drugs in clinical trials. Without knowing the biologic mechanisms of a therapeutic agent, developing improved therapies becomes inefficient. A good example of this occurred when investigators tried combining targeted anti-angiogenic therapy and chemotherapy. It was proposed that brief periods of vascular normalization brought about by anti-angiogenic therapy would allow better delivery of chemotherapy to the tumor (1). However, results of several phase III clinical trials studying the combination of anti-angiogenic therapy and concurrent chemotherapy were inconclusive, with some combination therapies showing improved outcomes (2-4) and others showing no improvement or even worse outcomes when compared with monotherapy (5-7). Results such as this demand a better understanding of drug pharmacodynamic effects during early stage clinical trials so that synergistic treatment combinations are more efficiently developed.

The preceding paragraphs highlight the need for novel response-based biomarkers that can measure the pharmacodynamic effects of new therapies and predict individual patient responses to therapy. Some of the most successful biomarkers to date are those derived from

tumor biopsies, which can be powerful tools to aid selection of therapy (8-10). However, due to the invasiveness of tissue biopsies, they are not possible for all tumor sites and repeat measurements are difficult to procure, limiting assessment of tumor heterogeneity and changes over time (11). Biomarkers derived from peripheral blood, such as liquid biopsies, offer a less invasive supplement to biomarkers derived from tissue biopsies (12). While peripheral blood markers can be measured longitudinally with relative ease, they do not offer a direct assessment of tumor sites and often cannot provide organ specific information that is necessary to fully characterize drug pharmacodynamic effects.

A third class of biomarkers, those derived from medical imaging, offer a useful complement to tissue biopsies and peripheral blood sampling. Imaging biomarkers provide an assessment of tumor sites and other organs as well as enable repeat measurements to assess changes during treatment. These advantages are part of the reason why medical imaging is the standard for evaluating therapeutic effects in clinical trials, with changes in anatomic tumor size or number of tumors measured ubiquitously for assessing patient responses (13). Anatomic imaging has proven useful for assessing response to established cytotoxic therapies such as radiation therapy or chemotherapy; however, it has proven less useful for monitoring emerging therapies for advanced cancers, where decreases in tumor size are not always indicative of response (14-16).

The five year survival rate for patients with advanced cancer remains relatively low for most cancer types (17), which has led to the recent development of two promising classes of therapy: anti-angiogenic therapy and immunotherapy. Both of these therapies have been shown to improve outcomes in subsets of patients but there are no reliable measures that can be used to identify these responding patients (18). The standard for assessing clinical response has been to

measure changes in tumor size derived from anatomic imaging modalities such as computed tomography (CT) (13,19). A limitation of this type of assessment is that changes in anatomic tumor size are slow relative to physiologic changes occurring in tumors following treatment. This is especially problematic for evaluating anti-angiogenic and immunotherapies, where immediate decreases in gross tumor size are not always present in responding patients. For example, anti-angiogenic therapies aim to slow proliferation of tumor cells by destroying tumor vasculature, which may not lead to measurable tumor shrinkage (16,20). During immunotherapy tumors may initially increase in size in responding patients due to immune cell infiltration, making assessment of progression difficult with anatomic imaging modalities (14).

Cancer is characterized by excessive, uncontrolled cell proliferation, and an earlier, potentially more useful biomarker of tumor response may be provided by measuring changes in tumor cell proliferation. Molecular imaging with the experimental modality 3'-Deoxy-3'-^{18}F-fluorothymidine positron emission tomography (FLT PET) enables non-invasive measurement of tumor cell proliferation. FLT is a radiolabeled molecular analogue of the DNA nucleoside thymidine that is preferentially taken up in proliferating cells (21). It has already been shown that FLT PET is capable of measuring tumor cell proliferation in clinical studies and that early changes in these measurements are predictive of clinical outcomes (22-39). However, few studies have evaluated FLT PET as a biomarker for emerging anti-angiogenic therapies or immunotherapies. Even fewer studies have investigated the clinical utility of dynamic PET scanning with FLT compartmental modelling, which theoretically enables improved quantification of cell proliferation and concurrent assessment of vascular changes (40,41).

Although FLT PET has shown promise in clinical trials, it remains an experimental tracer and has not been approved for assessing patient responses in routine clinical workflows; this is

partially due to limits in quantitative accuracy arising from small sample sizes and the technicality of performing dynamic PET scans. The overall goal of this dissertation is to investigate the utility of FLT PET/CT imaging as a response-based biomarker in anti-angiogenic therapy and immunotherapy. We will develop methodologies to improve the quantitative accuracy of FLT PET and when possible compare FLT PET measurements with established clinical biomarkers derived from anatomic imaging, peripheral blood samples, and tumor biopsies. The following specific aims outline the major goals of this dissertation:

Aim 1: Improve the quantitative accuracy of FLT PET. We aim to improve the quantitative accuracy of FLT PET imaging by performing dynamic scanning with FLT compartmental modelling. We also aim to identify normal data transformations that enable statistically powerful parametric modelling of PET datasets.

Aim 2: Assess the utility of FLT PET/CT imaging as a response biomarker in anti-angiogenic therapy. Greater understanding of pharmacodynamic effects of anti-angiogenic therapy may offer insight into resistance and improved treatment strategies. Pharmacodynamic effects will be assessed by analyzing serial FLT PET/CT scans during anti-angiogenic therapy; changes in tumor vasculature and cell proliferation will be summarized and correlated with other clinical biomarkers.

Aim 3: Assess the utility of FLT PET/CT imaging as a response biomarker in immunotherapy. We will investigate whether FLT PET detects changes in immune cell and tumor cell proliferation during immunotherapy. The PET data will be correlated with standard clinical markers of response and the occurrence of immune-related adverse events.

This dissertation is organized as follows: The rest of this chapter describes previous work that provides rationale for the studies in this dissertation. Section I describes efforts to improve the quantitative accuracy of FLT PET imaging, including compartmental modelling and parametric statistical modelling. Section II describes the results of studies wherein FLT PET is utilized for response assessment in anti-angiogenic therapy. Section III describes the results of studies wherein FLT PET is utilized for response assessment in immunotherapy. Section IV will provide an overall summary and conclude with future directions of this work.

1.2 Review of the FLT PET literature

A defining characteristic of cancer is excessive, uncontrolled cell proliferation; this has motivated a large body of research aiming to quantify tumor cell proliferation (42). In the 1950s, cell proliferation was measured using autoradiography of resected tissue with radiolabeled thymidine (43). As interest in measuring cell proliferation grew, driven in part by the growing interest in cancer research, new techniques for measuring it were developed. Notably, in 1983 a study reported on production of Ki67, a monoclonal antibody that binds to a nuclear antigen associated with cell proliferation (44). This antibody is now ubiquitous in clinical pathology departments and is routinely used for measuring proliferative rates of cancer cells via immunohistochemistry of resected tissue (45). However, a limitation of the Ki67 immunohistochemical method is that it requires removal of the tissue of interest, an invasive procedure. In 1988 a non-invasive technique for measuring cell proliferation was introduced that involved injection of ^{11}C-thymidine and PET scanning (46). However, the short half-life of carbon-11 (~20 minutes) and the presence of radiolabeled metabolites severely limited ^{11}C-thymidine's clinical utility as a PET tracer. In 1998 Shields et al. developed an alternative non-invasive method for measuring cell proliferation using FLT PET (21). FLT is an ^{18}F

radiolabeled thymidine analogue and its uptake into cells is increased during cell division (47). Unlike ^{11}C-thymidine, FLT has no confounding metabolic products that enter tissue, making quantification relatively straightforward (40,41). After entering cells, FLT is phosphorylated by thymidine kinase-1. FLT is not incorporated directly DNA but rather remains trapped in a phosphorylated state within cells, providing a measure of thymidine kinase-1 activity that is upregulated in proliferating cells (41,48). The clinical utility of FLT PET is supported by studies showing that tumor FLT uptake correlates with measures of tumor cell proliferation derived from Ki67 immunohistochemical staining (21,40,48-51).

A literature review revealed 202 clinical studies in human patients that have in some way utilized FLT PET. The first clinical FLT PET study was performed in 2002, which was followed by a steady rise in yearly studies until 2011 wherein the number of yearly studies plateaued at 13-18 studies per year (**Figure 1**). The most frequent utilization of FLT PET in clinical studies has been for response assessment (**Table 1**). Of these studies, FLT PET has primarily been used to assess response in chemotherapy, radiation therapy, or epidermal growth factor receptor inhibition therapy (**Table 2**). A number of these studies have showed that changes in tumor FLT uptake measured shortly after therapy are correlated with long-term clinical outcomes (22-39). These results demonstrate the potential value of utilizing FLT PET to assess effects of cancer therapies. Furthermore, dynamic FLT PET kinetic parameters derived from compartmental modeling quantify not only cell proliferation but also vascular characteristics such as perfusion and the vascular fraction of tissue (41,52). This multi-faceted assessment of multiple biological processes has potential to inform of therapeutic effects and their mechanisms that ultimately lead to a positive or negative response.

The focus of this dissertation will be FLT PET response assessment in anti-antiangiogenic therapy and immunotherapy. These are two areas where FLT PET has not been extensively utilized and both types of therapy would benefit from the development of new response-based biomarkers. A literature review of FLT PET in anti-angiogenic therapy and immunotherapy is presented at the beginning of Sections II and III, respectively.

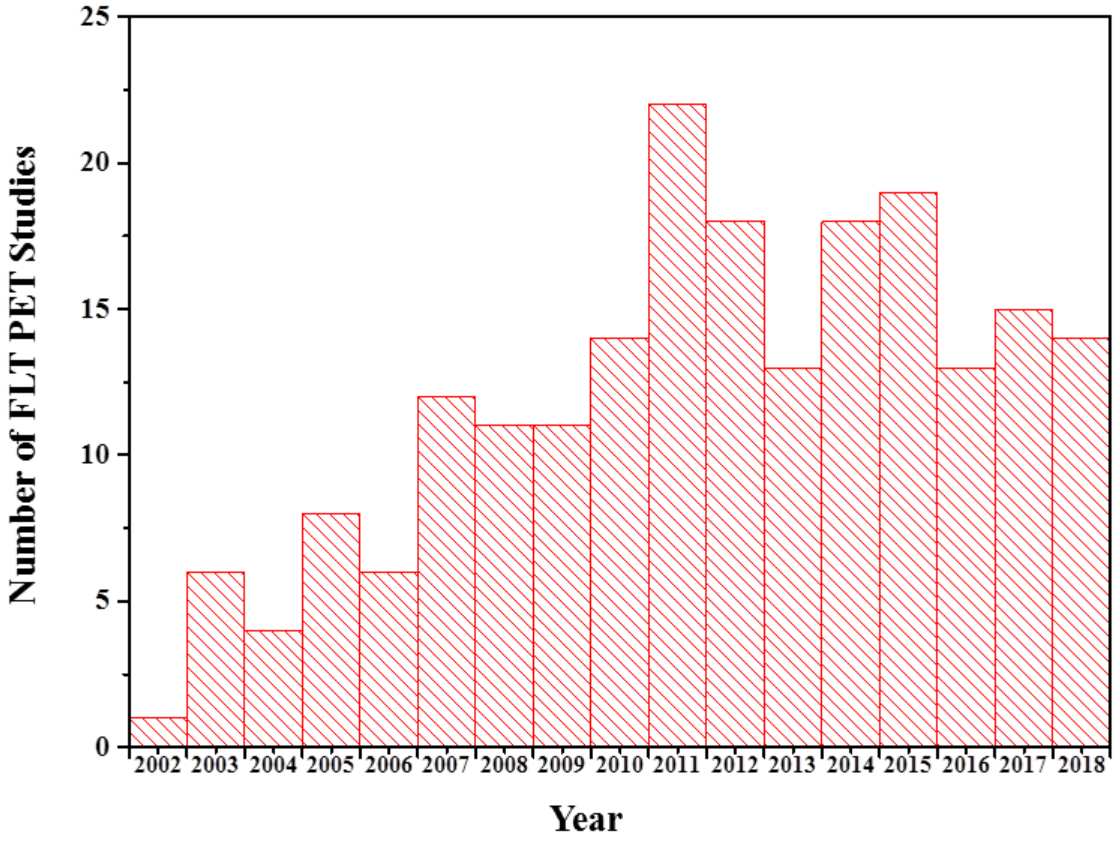

Figure 1: Number of published studies that have utilized FLT PET by year (only studies with human patients included).

Table 1: Summary of published studies that have utilized FLT PET

Study Purpose	Description	Number of studies
Response	This included studies wherein the primary goal was to	89/202

assessment	evaluate therapeutic effects using FLT PET	44%
Diagnosis	This included studies wherein the primary goal was to evaluate the ability of FLT PET for diagnosing disease (in nearly all cases cancer)	67/202 33%
Modality validation	This includes studies that correlated FLT PET with an independent reference standard (typically Ki67 immunohistochemistry), studies that assessed the safety/toxicity of FLT PET, or studies that performed test-retest FLT PET scans	27/202 13%
Development of image analysis tools	This included studies whose primary goal was development of a method/algorithm for analyzing FLT PET images e.g. compartmental modelling approaches, automated image analysis, etc.	11/202 5%
Radiotherapy treatment planning	This included studies aiming to use FLT PET to identify organs at risk (bone marrow) or define gross tumor volumes to aide in radiotherapy treatment planning	8/202 4%

Table 2: Summary of studies that have used FLT PET for response assessment

Therapy	**Number of studies**
Chemotherapy	24/89 27%
Chemotherapy and radiation	15/89 17%
Epidermal growth factor receptor inhibitor	11/89 12%
Radiation	10/89 11%
Anti-angiogenic	7/89 8%
Anti-angiogenic and chemotherapy*	6/89 7%
Mixed	6/89 7%
Other	5/89 6%
Surgery	3/89 3%
Immunotherapy	2/89 2%

* All studies in brain tumors except 1 (that study is presented in this dissertation)

Section I FLT PET quantification

Before utilizing FLT PET to investigate physiologic changes during therapy, steps must be taken to ensure measurements are quantitative. The most common metric of FLT PET quantification is the standardized uptake value (SUV). The SUV is calculated by taking the radioactivity concentration in a given region of interest (ROI) and normalizing it by the ratio of the injected dose divided by the patient weight (53). Validation of the SUV as a quantitative measure has been performed by comparing FLT SUV measurements with reference standards of cell proliferation derived from immunohistochemistry (51). The precision of FLT SUV measurements has also been assessed through test-retest studies. FLT PET repeatability coefficients for SUV_{mean} (i.e. the average SUV within an ROI) were found to be 41-53% in breast cancer tumors, 11-39% in lung cancer tumors, 23% in gliomas, and 20% in healthy bone marrow (54-60). A retrospective review of FLT PET test-retest data concluded that differences greater than 25% in FLT SUV metrics likely represents a true change in tumor uptake (61). This section will discuss our methods to further improve the quantitative accuracy of FLT PET in clinical trials. Chapter 2 will discuss a methodology for FLT PET compartmental modelling that enables concurrent assessment of vascular and proliferative changes in tumors. Chapter 3 will discuss methods to enable parametric statistical modelling of PET data.

Chapter 2: Improving the quantitative accuracy of FLT PET with compartmental modelling

2.1 Motivation

While the FLT SUV provides a robust estimate of tumor cell proliferation, only moderate correlation with measures of cell proliferation derived from reference standards such as Ki67 immunohistochemistry has been shown. This is likely due to dephosphorylation of bound FLT that causes the tracer to leave the imaging region (40,41). A more accurate estimate of cell proliferation can be derived from dynamic FLT PET images and tracer compartmental modelling. In this case, the uptake of FLT into tissue is modelled as a function of time, providing an estimate of the net flux of FLT from the blood pool to its phosphorylated state within cells. The net flux of FLT (K_i) has been shown to be more correlated with measures of cell proliferation derived from reference standards than FLT SUVs (40,49,50). An additional advantage of FLT compartmental modelling is that it provides an assessment of tumor vascular changes that are important for evaluating anti-angiogenic therapies.

However, there are a number of challenges that have hindered widespread adoption of dynamic FLT PET scanning in oncology. This includes 1) the limited axial field of view (FOV) of current PET scanners, 2) the low signal to noise ratio in the short dynamic frames, 3) the requirement of a vascular input function that has been corrected for FLT metabolites in the blood, and 4) the need for specialized software for analysis of dynamic scans. While increasing the FOV of current clinical PET scanners is outside the scope of this dissertation, other research groups aim to address this challenge (62). Our research group has however, already developed specialized software for analyzing dynamic FLT PET scans using compartmental modelling

(63,64). In this chapter we will expand on this work by incorporating a correction to account for FLT metabolism in the vascular input function.

FLT is metabolized in the liver, resulting in the metabolite FLT-glucuronide that is confined to the liver and vasculature (47,50,65). The vascular input function for FLT kinetic analysis must be corrected for this metabolite. The metabolite correction can be performed using blood samples taken during each dynamic PET frame (full blood sampling); however, this process is invasive. One study has claimed that a population-based correction (no blood sampling) is a viable method, resulting in mean absolute difference in kinetic parameter estimates of 6% from corrections derived from full blood sampling (66). In this chapter we derive our own population based correction for FLT metabolism and investigate whether metabolite correction with *limited* blood sampling at 45 and 100 minutes post-injection results in significantly different estimates of kinetic parameters relative to our population-based correction.

A FLT metabolite correction with limited or no blood sampling would reduce the invasiveness of dynamic PET imaging, providing a more clinically feasible methodology. In addition to investigating a less invasive metabolite correction, this chapter will assess the uncertainty in tumor kinetic parameter estimates due to noise in dynamic frames. Characterizing the effects of noise on kinetic parameter estimates will be useful for deciphering what may be true changes in kinetic parameter estimates during therapy. The work in this chapter will be derived from a dataset of patients undergoing anti-angiogenic therapy. The resulting FLT kinetic model discussed in this chapter will be applied to characterize the pharmacodynamic effects of anti-angiogenic therapy in Chapter 5: Dynamic FLT PET to investigate concurrent changes in tumor vasculature and cell proliferation during anti-angiogenic therapy.

2.2 Methodology

FLT PET/CT Acquisition

Thirty-three patients are included in this chapter's analysis. These patients underwent dynamic FLT PET scanning at three timepoints during the course of intermittent anti-angiogenic therapy (at baseline, after two weeks of continuous treatment, and after a one week treatment break). All dynamic PET scans were performed on a GE Discovery LS PET/CT scanner (GE, Waukesha WI). The PET/CT field of view (FOV) was chosen to include a solid tumor amenable to FLT PET analysis as well as include a major artery for extracting the vascular input function. Each patient was scanned with the same FOV for all PET/CT scans. Prior to initiating dynamic PET scans a low dose CT scan without contrast agent was acquired. Immediately following the CT scan, patients were injected with a bolus of FLT (mean 370 MBq and standard deviation 110 MBq). The first 22 PET dynamic frames were acquired from 0-40 minutes post-injection with: eight 15-s, four 30-s, six 60-s, two 5-min, and two 10-min frames. An additional 23rd frame was acquired between 60 and 90 minutes post-injection and lasted 5-min. The final (23^{rd}) frame was rigidly registered to the 22^{nd} frame using Amira software (ThermoFisher Scientific Inc., Waltham MA) and was visually verified for alignment. PET images were reconstructed using an ordered subsets expectation maximization algorithm using the CT scan for attenuation correction. The reconstruction parameters included: 2 iterations, 35 subsets, and 6-mm Gaussian axial post filter. The grid size was 128×128×47 with voxel dimensions of 5.47, 5.47, and 3.27 mm, respectively.

FLT PET/CT Segmentation

Using the combined PET/CT image and diagnostic radiology reports, tumors within the PET FOV were identified by an experienced nuclear medicine physician. Tumors were manually segmented on all scans using Amira software. For vascular input function the ascending aorta, descending aorta, or common iliac were manually segmented using early PET frames for vessel visualization and later frames to ensure absence of severe motion artifacts (67). The mean values of the vessel segmentation in each PET frame were fit to a tri-exponential function (to minimize noise) that was used as input function for FLT compartmental modelling (68,69). To minimize the impact of input function partial volume effects, we focused the analysis on assessing relative changes in FLT kinetic parameters.

FLT Metabolite Correction

Venous blood was extracted during the PET/CT scans for nine patients with an intravenous line in the arm opposite FLT injection (40,67). Blood samples were centrifuged for five minutes at 1500 rpm to separate out the plasma (**Figure 2**). For each sample, 100 μL of plasma was mixed with 4 mL of deionized water and run through a Sep-Pack (Waters Corporation, Milford MA) to collect the metabolite sample. Next 10 mL of ethanol was run through the Sep-Pak to collect the FLT sample. Samples were counted using an auto gamma counter (PerkinElmer, 2480 WIZARD^2) and the fraction of unmetabolized FLT in blood (FLT fraction) was calculated by dividing the counts for the FLT sample by the sum of the counts from the FLT and metabolite samples. A double exponential fit to each patient's FLT fraction measurements at 45 and 100 minutes was used to derive *patient-specific* FLT metabolite

corrections. A *population-based* metabolite correction was derived by fitting a double exponential to the median value of FLT fraction measurements across all measured values at 45 and 100 minutes.

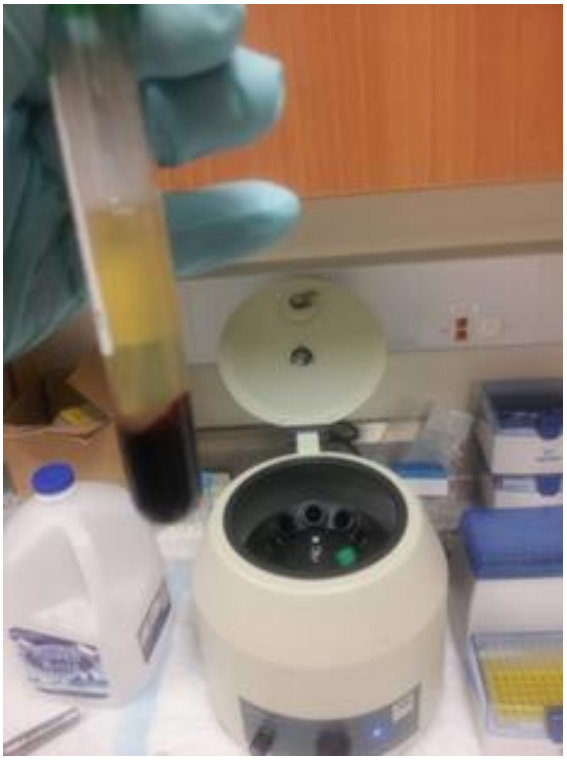

Figure 2: Tube containing patient plasma and hematocrit after centrifugation.

FLT Compartmental Modelling

FLT uptake in tumor voxels during dynamic PET scanning was used to specify voxel time activity curves (TACs). The tumor voxel TACs, vascular input function, and metabolite corrected vascular input function were used to fit the FLT compartmental model for each tumor voxel (**Figure 3** and

Table 3). Each voxel was fit to a four and a five parameter kinetic model (k_4 was set to zero in the four parameter model) and the model with the lower Akaike information criterion

(AIC) was utilized. Given high covariance between K_1 and k_2 parameters, the model was reparametrized by exchanging the k_2 parameter with the ratio of K_1 over k_2 (V_d) to improve identifiability of K_1 (41). Equations 1-3 below, describe the four parameter model and Equations 1, 4 and 5 describe the five parameter model. For both models the net flux of FLT (K_i) from vasculature into a phosphorylated state within cells was calculated to quantify cell proliferation (Equation 6) (70). All curve fitting was done using the trust-region-reflective least-squares minimization algorithm in MATLAB (63).

$$\text{Tissue concentration} = (Q_e + Q_m + V_b C_b)\rho \qquad \text{Eq 1}$$

$$\frac{dQ_e}{dt} = K_1\, C_{bFLT} - k_2\, Q_e - k_3\, Q_e \qquad \text{Eq 2}$$

$$\frac{dQ_m}{dt} = k_3\, Q_e \qquad \text{Eq 3}$$

$$\frac{dQ_e}{dt} = K_1\, C_{bFLT} - k_2\, Q_e - k_3\, Q_e + k_4\, Q_m \qquad \text{Eq 4}$$

$$\frac{dQ_m}{dt} = k_3\, Q_e - k_4\, Q_m \qquad \text{Eq 5}$$

$$K_i = \frac{K_1 k_3}{k_2 + k_3} \qquad \text{Eq 6}$$

Table 3: Variable definitions for the FLT compartmental model

^{18}F-FLT parameters	
C_b	Vascular FLT and metabolized FLT (mBq/mL)
C_{bFLT}	Vascular FLT after metabolite correction (mBq/mL)
Q_e	Exchangeable (unbound) FLT (mBq/g)
Q_m	Phosphorylated FLT (mBq/g)
ρ	Tissue specific gravity (assumed to be equal to 1 g/mL)
V_b	Blood volume or vascular fraction of tissue (mL/g)
K_1	Initial rate constant for transport of ^{18}F-FLT from vasculature into cells (mL/min/g)
k_2	Rate constant for transport of ^{18}F-FLT from cells into vasculature (min^{-1})
V_d	Early distribution volume of ^{18}F-FLT in tissue - equal to ratio of K_1 divided by k_2 (mL/g)
k_3	Rate constant for phosphorylation of ^{18}F-FLT to ^{18}F-FLT monophosphate by thymidine kinase 1 (min^{-1})
k_4	Rate constant for dephosphorylation of ^{18}F-FLT monophosphate to ^{18}F-FLT by 5′(3′)-deoxyribonucleotidase (min^{-1})
K_i	Net flux of ^{18}F-FLT from vasculature into phosphorylated state within cells (mL/min/g)

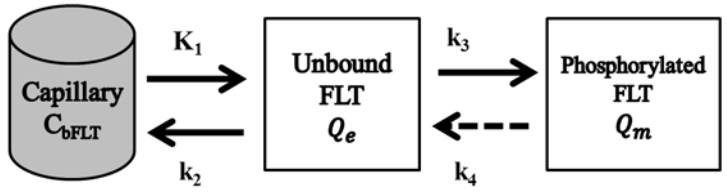

Figure 3: The two-tissue compartment FLT kinetic model following notation introduced by Muzi et al. (*27*). The model includes kinetic rate-constants (K_1, k_2, k_3, k_4) as well as additional free parameter V_b that are estimated from model fitting. The net flux of tracer (K_i) is calculated from the kinetic rate constants and has been shown to be increased in proliferating cells.

Covariance of model parameters was investigated to determine which FLT kinetic parameters could be independently estimated during the course of anti-angiogenic therapy (41,71). Monte Carlo simulations were also performed to assess the effect of noise on relative change estimates of the kinetic parameters. For each patient, the Monte Carlo simulations consisted of: 1) estimate 'true' kinetic parameter values using tumor TACs from the clinical data, 2) simulate PET TACs using 'true' parameter values, 3) add Poisson noise to the simulated PET TACs, 4) estimate kinetic parameters for simulated PET TACs, 5) calculate relative changes in

the estimated kinetic parameters across timepoints, and 6) calculate the bias (Equation 7) and root mean square error (Equation 8) of the relative change estimates by comparing with the relative changes in the 'true' parameter values (72).

$$\text{bias}=\frac{\sum_i(R_i-R_t)}{N} \qquad \text{Eq 7}$$

$$\text{RMSE}=\sqrt{\frac{\sum_i(R_i-R_s)^2}{N}} \qquad \text{Eq 8}$$

where R_i is the relative parameter estimate from the i^{th} simulation, R_t is the 'true' relative parameter value, and N is the total number of simulations.

Statistical Analysis

Due to the skewed nature of the FLT uptake distributions, we utilized non-parametric statistics to analyze the data. The median value of each tumor's voxel-based kinetic parameter distributions was extracted, providing summary kinetic parameters for each tumor. The median kinetic parameter value across all tumors within a given patient was extracted, providing summary kinetic parameters for each patient. Significant changes in FLT metabolism during treatment were assessed using Wilcoxon signed-rank tests.

2.3 Results

The median values of FLT fraction measurements across the scans from the nine patients with venous blood sampling were 0.78 and 0.70 at 45 and 100 minutes, respectively. These values were used to derive the population-based correction for FLT metabolism (**Figure 4**a). Wilcoxon signed-rank tests indicated FLT metabolism did not change significantly during the course of anti-angiogenic therapy i.e. the FLT fraction measurements at 45 and 100 minutes

post-injection were not significantly different across imaging timepoints (**Figure 4**b). This indicates anti-angiogenic therapy has a minimal effect on the metabolism of FLT and the same population-based correction for FLT metabolism may be used throughout anti-angiogenic therapy. Further, relatively small changes in kinetic parameters were found when going from the patient-specific to the population-based correction for FLT metabolism (**Figure 4**c), indicating little benefit to using the patient-specific FLT metabolite correction.

All thirty-three patients with various metastatic cancers were included in the analysis of kinetic parameter covariance and noise simulations. At baseline, parameter covariance was similar to what has been reported previously for the FLT kinetic model, including high covariance (correlation coefficient greater than 0.90) between the k_3 and V_d parameters (**Table 4**). Moreover, covariance of FLT kinetic parameters did not change appreciably during the course of anti-angiogenic therapy. The number of tumor voxels utilizing the 5 parameter FLT kinetic model were 6,859 (33%), 3,984 (24%), and 6,555 (35%) at the baseline, peak drug, and washout timepoints, respectively. Nearly all tumors (>95%) had some voxels utilizing a 4 parameter model and some utilizing a 5 parameter model.

Figure 5 shows the results from the Monte Carlo simulations. The median value of the bias is close to zero for all kinetic parameters, indicating estimates of relative parameter changes across a patient population will be unbiased. The median value of the RMSE is approximately 15% for V_b, K_1, V_d, and K_i; however, the RMSE for k_3 is larger (median approximately 30%), indicating estimates of k_3 will be less precise relative to the other parameter estimates.

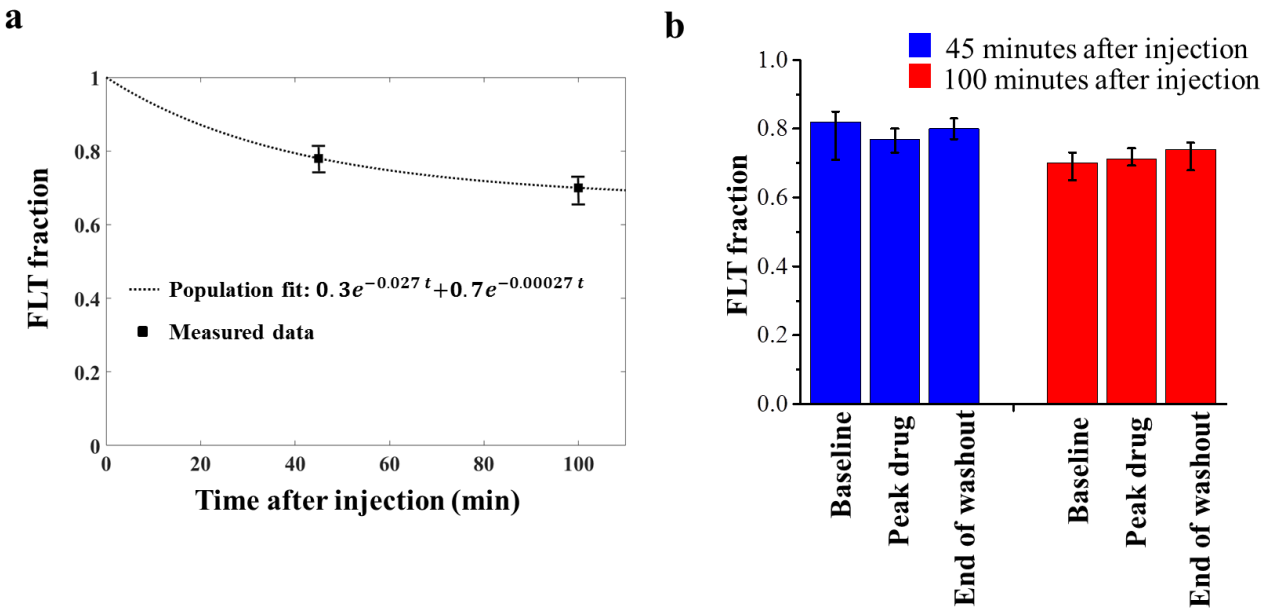

c

Kinetic parameter	Median change (%)	Interquartile range (%)	Range (%)	P-value
V_b	0	-1 to +1	-5 to +18	0.82
K_1	0	-2 to 0	-5 to +4	0.79
V_d	-1	-2 to +1	-22 to +3	0.22
k_3	+5	-6 to +8	-33 to +50	0.23
K_i	+3	-11 to +6	-36 to +28	0.50

Figure 4: (a) A population-based correction for FLT metabolism was formulated using an exponential fit to the median value of FLT fraction measurements across all patients at 45 and 100 minutes. Measurement data points show median values and error bars show interquartile range across all patients' blood sample measurements. (b) Comparison of FLT metabolism at different timepoints during VEGFR-TKI treatment. The bars show the median value across all patients ± interquartile range. (c) Going from patient-specific to the population-based metabolite correction led to relatively small changes in FLT kinetic parameters and no changes were significant using a Wilcoxon signed-rank test.

Table 4: Normalized covariance matrix for FLT kinetic parameters.

	K_1	**V_d**	**k_3**	**k_4**	**V_b**
K_1	1	-	-	-	-
V_d	-0.56* (-0.75 to -0.34)**	1	-	-	-
k_3	0.45 (0.29 to 0.53)	-0.93 (-0.94 to -0.93)	1	-	-
k_4	-0.18 (-0.40 to -0.01)	-0.37 (-0.48 to -0.13)	0.65 (0.45 to 0.76)	1	-
V_b	-0.62	0.08	-0.08	0.16	1

	(-0.72 to -0.58)	(-0.10 to 0.24)	(-0.15 to -0.02)	(0.04 to 0.30)	

* These coefficients were summarized the same way as kinetic parameter s (i.e. taking medians)
**Interquartile range

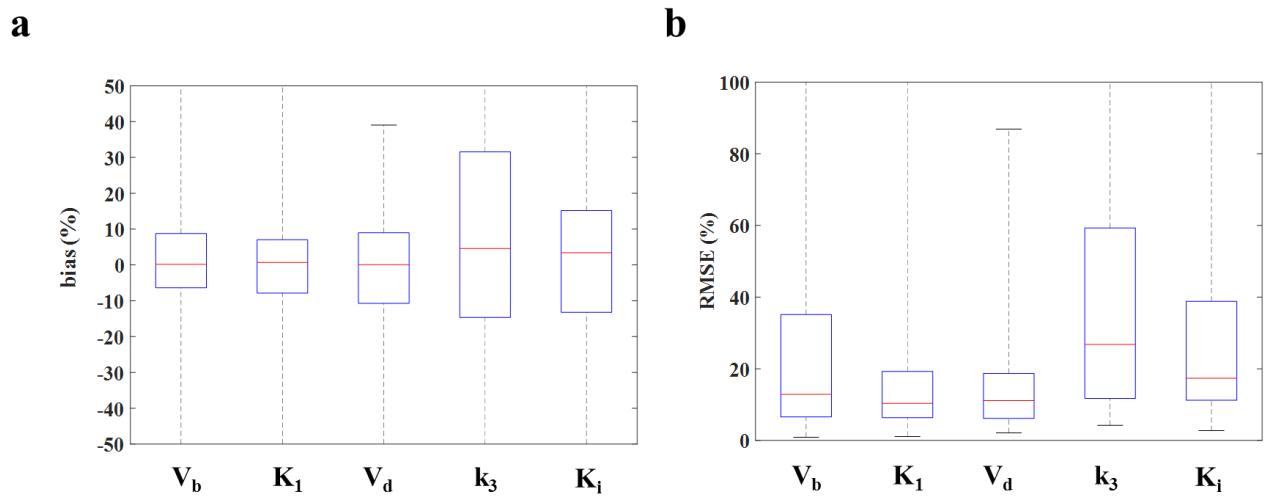

Figure 5: The box plots show the bias (a) and RMSE (b) for each kinetic parameter that were calculated from the Monte Carlo simulations.

2.4 Discussion

In this chapter a population-based correction for FLT metabolism was derived using blood samples extracted 45 and 100 minutes after tracer injection. Comparison between kinetic parameter estimates using the population-based correction and patient-specific correction using blood samples demonstrated relatively small changes in kinetic parameters for the majority of patients. This suggests the population-based correction for FLT metabolism is a viable non-invasive option for assessing changes in FLT kinetic parameters during anti-angiogenic therapy. Further comparisons of population-based corrections with patient-specific corrections using full blood sampling at various timepoints after injection, as was done in Shields et al. (66), would be valuable to further characterize uncertainties associated with population-based corrections.

Noise in the dynamic PET frames leads to uncertainty in kinetic parameter estimates. To characterize the effect of noise on the parameters estimates we performed Monte Carlo simulations. From these simulations we found the bias in relative parameter estimates was close to 0% (median) and the root mean squared error was approximately 15% (median) for V_b, K_1, and K_i. However, there are additional factors besides noise that lead to uncertainty in the kinetic parameter estimates. Test-retest studies of FLT kinetic parameters in tumors have shown relatively small mean changes in kinetic parameters from test to retest timepoints; however, the repeatability coefficients (1.96σ) were approximately 50% for K_i and 70% for V_b (58,73). These results suggest conclusions regarding changes in V_b, K_1, and K_i may be reliable when summarized across a large population but changes in any individual patient's kinetic parameters should be interpreted with the relatively large parameter uncertainties in mind. Prospective test-retest studies of FLT kinetic parameters in larger patient populations would allow improved characterization of patient-level uncertainties; this would likely be necessary before clinical decisions could be made based on changes in any individual's FLT kinetic parameters.

2.5 Conclusion

In this chapter we introduce a FLT compartmental model that can be used to measure kinetic parameters, such as the net flux of FLT (K_i) that theoretically offers a more reliable measure of cell proliferation than the FLT SUV. We have derived a population-based correction for FLT metabolism using patient blood sampling at 45 and 100 minutes. This population-based correction removes the need for blood sampling to correct for FLT metabolism, making the kinetic modelling approach more feasible for clinical studies. Finally, we characterized the effects of noise on kinetic parameter estimates, concluding that population-based estimates of

kinetic parameter changes will be unbiased. The results from this chapter will be applied in Chapter 5: Dynamic FLT PET to investigate concurrent changes in tumor vasculature and cell proliferation during anti-angiogenic therapy.

Chapter 3: Improving the quantitative accuracy of FLT PET with parametric statistical modelling

3.1 Motivation

When quantifying the pharmacodynamic effects of a given therapeutic agent, summary statistics are calculated by combining changes in a given biomarker across a population of patients. A significant change in the summary statistic indicates whether or not the therapy is having its intended effect. The quantitative accuracy of summary statistics can be improved with parametric statistical modelling. Parametric statistical modelling can provide increased statistical power by accounting for correlations in underlying data. For example, when analyzing patients with multiple tumors, investigators may summarize SUVs for each patient (19,25). Although this approach gives SUVs without intra-patient correlations, it discards information (e.g. SUVs for each tumor are reduced to single SUV for each patient by taking the average SUV across all tumors within a patient) and consequently reduces statistical power. An alternative analysis may be to incorporate the tumor SUVs into a parametric model that accounts for intra-patient correlation of tumor SUVs.

Unfortunately, the skewed nature of PET SUV distributions prevents parametric statistical modelling (74). Furthermore, skewed SUV distributions limit use of other parametric statistical tests such as t-tests, linear regression, and analysis of variance (75). If the normality assumptions of these statistical tests are violated, resulting parameter estimates and conclusions may not be reliable. This motivates PET SUV transformations that result in normal distributions and allow utilization of parametric statistical techniques (53,56,76). The increased statistical power provided by these parametric techniques can potentially reduce the number of patients and expenses required for clinical studies.

^{18}F-fluorodeoxyglucose (FDG) is a widely used PET radiotracer for quantifying glucose utilization in tumors (19,77). FDG SUVs extracted from tumors have been shown to be positively skewed and a log transformation has been shown to provide normal FDG SUV distributions in some cases (53). No study has assessed the normality of FLT PET SUV distributions. In this chapter the utility of Box-Cox transformations for providing normal SUV distributions is assessed for FLT SUV distributions (78). For comparison and to demonstrate the generalizability of our methodology we also apply Box-Cox transformations to FDG SUV distributions. To our knowledge this is the first study to utilize Box-Cox transformations on PET data. Sensitivity of the normal transformations to therapy is investigated. Lastly, the lognormal behavior of these SUV distributions is investigated and compared with the optimal Box-Cox transformation.

3.2 Methodology

Imaging cohorts

The transformation methodology is applied to two imaging cohorts. The first cohort consists of FLT PET imaging data from our institution (University of Wisconsin Carbone Cancer Center). This includes patients with metastatic cancers that underwent FLT PET scanning at baseline and after two weeks of anti-angiogenic therapy (Table 5). The second cohort is a publicly available dataset (Radiation Therapy Oncology Group 0522 from the Cancer Imaging Archive) that consists of patients with head and neck squamous cell carcinoma that underwent FDG PET scans at baseline and eight weeks after radiation therapy (77). The maximum SUV of voxels within a tumor (SUV_{max}) is extracted from each tumor and the resulting distributions of tumor SUV_{max} are analyzed using our transformation methodology.

Table 5: Summary of the patient cohorts utilized in this study.

Cohort	Tracer	Disease	Therapy	Timepoints	Number of patients	Number of tumors
1	FLT	Various metastatic solid tumors	Anti-angiogenic	Pre, Post	27	70
2	FDG	Head and neck primary and nodal tumors	Radiation	Pre , Post	52	126

Identification of optimal transformations

To identify optimal transformations, we apply one parameter Box-Cox transformations to SUV distributions (Equation 9).

$$T=\begin{cases} \frac{S^{\lambda}-1}{\lambda} & \text{if } \lambda \neq 0 \\ \ln(S) & \text{if } \lambda = 0 \end{cases} \qquad \text{Eq 9}$$

where S is the untransformed SUV measurement, λ is the Box-Cox transformation parameter, and T is the resulting transformed SUV measurement. An optimal transformation is identified by conducting a grid search of λ in order to ascertain the distribution of transformed values which most closely resembles a normal distribution. The transformation parameter is varied in increments of 0.01 within the range of -3 to +3. The optimal transformation parameter is selected as that which produces a transformed SUV distribution with the maximum Shapiro-Wilk P-value (79).

Ninety-five percent confidence intervals (95% CI) for the optimal transformation parameter are calculated with non-parametric bootstrapping using the bias corrected and accelerated bootstrap implemented using the boot function in R version 3.4 (80). The resampling for the bootstrap is performed on a patient-level with 10,000 iterations. Identification of an optimal transformation parameter is repeated separately for each imaging cohort. To

characterize the resulting distributions, we calculate the distribution mean, skewness (Equation 10) and excess kurtosis (Equation 11)

$$\gamma_1 = \frac{\frac{1}{N}\sum_i^N (S_i - \bar{S})^3}{\left(\frac{1}{N}\sum_i^N (S_i - \bar{S})^2\right)^{\frac{3}{2}}} \qquad \text{Eq 10}$$

$$\gamma_2 = \frac{\frac{1}{N}\sum_i^N (S_i - \bar{S})^4}{\left(\frac{1}{N}\sum_i^N (S_i - \bar{S})^2\right)^2} - 3 \qquad \text{Eq 11}$$

N is the number of tumors in the SUV distribution, S_i is the SUV for the ith tumor, and $\bar{S}$ is the mean of the tumor SUV distribution. Quantile-Quantile plots (Q-Q plots) were also generated to characterize resulting distributions and their deviations from normality (81,82).

3.3 Results

The effect of the Box-Cox transformation on SUVs is shown **Figure 6**. When the transformation parameter is less than one, the Box-Cox transform reduces positive skewness by shifting higher SUVs closer to lower SUVs. The amount of shift is determined by the transformation parameter, with lower values of the transformation parameter leading to greater shift in SUVs.

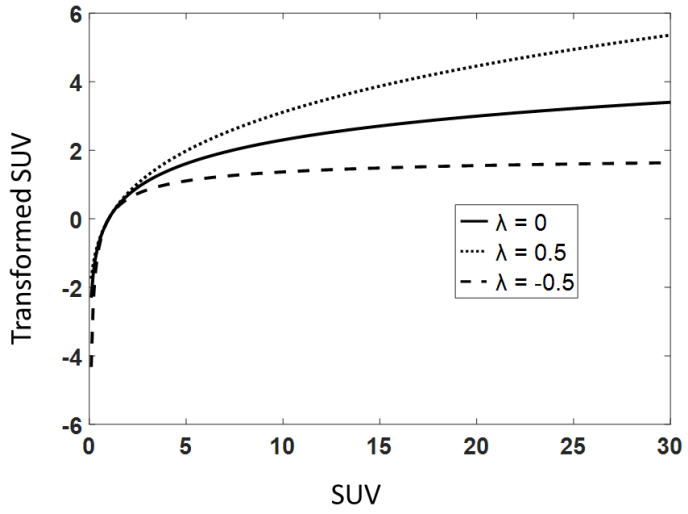

Figure 6: For a given transformation parameter λ, the Box-Cox transform reduces positive skew by shifting high SUVs closer to low SUVs. Various values of the transformation parameter are shown by different curves.

Untransformed SUV distributions for both FLT and FDG deviated significantly from normality, demonstrating relatively high coefficients of variation as well as high values of skewness and excess kurtosis (**Table 6**). The optimal Box-Cox transformation parameters for FLT and FDG are shown in **Figure 7**. The optimal transformations for FLT SUV_{max} distributions were λ = -0.02 (95%CI: -0.34 to 0.30) and λ = -0.37 (95%CI: -0.77 to -0.03) at pre and post treatment, respectively. The optimal transformations for FDG SUV_{max} were λ = 0.42 (95% CI: 0.17 to 0.67) and λ = -0.01 (95% CI: -0.58 to 0.41) at pre and post treatment, respectively.

Figure 8 shows Q-Q plots for the untransformed, log transformed, and optimally transformed FDG SUV_{max} distributions. The untransformed SUV distributions had quantiles greater than expected for normal distributions, indicating non-normal behavior (**Figure 8**a and **Figure 8**d). After a log transformation, the SUV distributions exhibited more normal behavior (**Figure 8**b and **Figure 8**e); however, some quantiles fall below what is expected for a normal

distribution (**Figure 8**b). The quantiles for the optimally transformed distributions demonstrated good agreement with expected normal quantiles (**Figure 8**c and **Figure 8**f).

For both FLT and FDG, therapy resulted in increased skewness and kurtosis in SUV_{max} distributions, leading to a decrease in the optimal transformation parameter from pre to post treatment. After applying the optimal transformations, all SUV distributions had reduced skewness and excess kurtosis and none of the distributions deviated significantly from normality. A log transformation also resulted in reduced skewness and excess kurtosis but the pre treatment FDG SUV_{max} distribution remained significantly non-normal even after log transformation (Table 6).

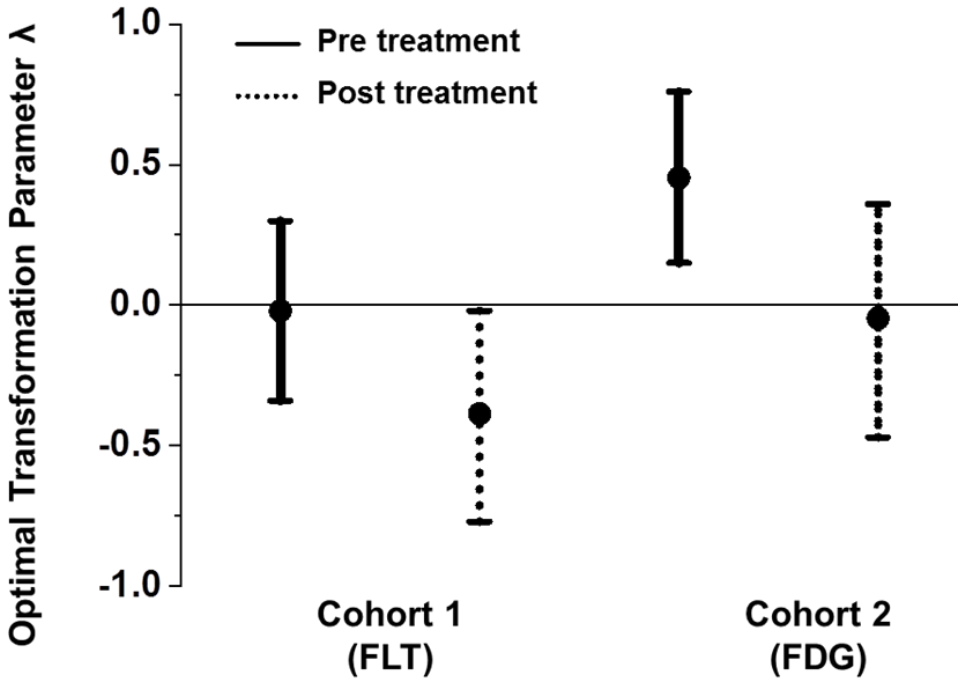

Figure 7: Optimal transformation parameters and 95% confidence intervals for the SUV_{max} distributions of both patient cohorts. There are cases where the optimal transform deviates significantly from $\lambda=0$, indicating a log transformation is not likely to be optimal for producing normal SUV distributions.

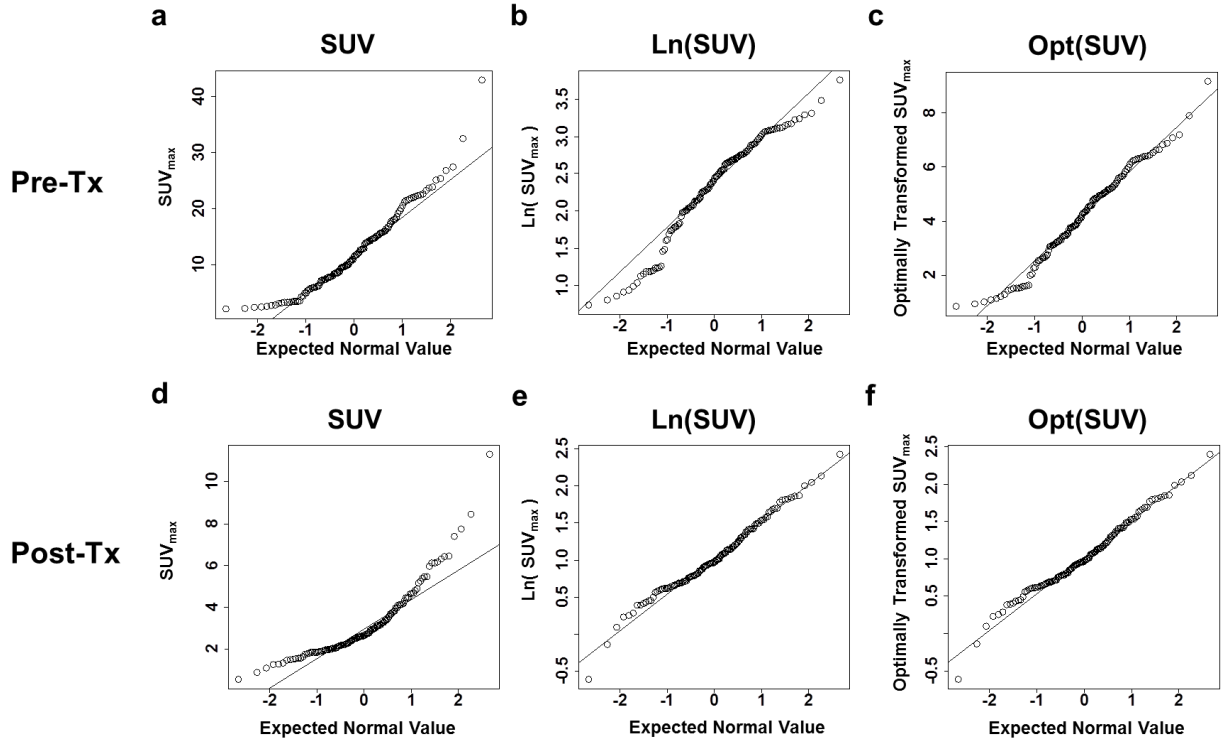

Figure 8: Q-Q plots of SUV_{max}, log transformed SUV_{max}, and optimally transformed SUV_{max} at pre treatment (a-c) and post treatment (d-f). In these plots the measured SUVs are plotted vs. the expected quantiles values of a standard normal distribution. If the measured SUVs followed a true normal distribution, we expect the measured SUVs to be linearly proportional to the standard normal quantiles (indicated by the line of normality shown on each plot). If the measured SUVs lie above this line that indicates the SUV measurements are higher than would be expected for a normal distribution. This is the case for both the pre (a) and post (d) treatment SUV distributions where a number of measured SUVs lie above the line of normality, indicating positive skewness. At pre treatment, the log transform shifts the data too far turning a positive skew (a) into a negative skew (b); however, there is minimal skew for the optimal transformation (c). At post treatment, there is visual improvement in normality when going from untransformed SUV (d) to log transformed SUV (e). In this case, since the log transform is very close to optimal, there is little difference when going from log transformed (e) to optimally transformed SUV (f).

Table 6: Summary of the untransformed, optimally transformed, and log transformed SUV_{max} distributions. Distribution statistics for FLT SUV_{mean} and SUV_{total} are also included for comparison.

		No Transform					Optimally Transformed					Log Transformed (λ=0)				
PET metric	Time	Mean	CV[a]	γ_1[b]	γ_2[c]	P[d]	Mean	CV[a]	γ_1	γ_2	P	Mean	CV[a]	γ_1	γ_2	P
FLT SUV_{max}	Pre	6.0	0.6	1.3	1.2	<0.01	1.9	0.4	0.0	-0.5	0.49	1.6	0.4	0.0	-0.5	0.49
	Post	4.6	0.7	1.6	2.0	<0.01	1.0	0.4	0.0	-0.8	0.30	1.3	0.5	0.4	-0.6	0.05
FLT SUV_{mean}	Pre	2.4	0.5	1.0	0.4	<0.01	0.7	0.6	0.0	-0.7	0.33	0.8	0.6	0.1	-0.8	0.28
	Post	2.0	0.6	2.5	7.9	<0.01	0.5	0.8	0.0	0.7	0.56	0.6	0.9	0.6	0.8	0.08
FLT SUV_{total}	Pre	91.6	1.9	4.0	17.7	<0.01	3.5	0.4	0.0	-0.6	0.71	3.5	0.4	0.0	-0.6	0.71
	Mid	53.1	1.6	3.2	11.3	<0.01	3.0	0.6	0.0	-1.0	0.07	2.8	0.6	-0.1	-1.0	0.07
FDG SUV_{max}	Pre	12.3	0.6	0.9	1.4	<0.01	4.2	0.4	0.0	-0.5	0.12	2.3	0.3	-0.5	-0.4	<0.01
	Post	3.2	0.5	1.7	4.2	<0.01	1.0	0.5	0.1	0.6	0.21	1.0	0.5	0.1	0.6	0.21

[a] Coefficient of variation
[b] Skewness
[c] Excess kurtosis
[d] Shapiro-Wilk P-value for assessing distribution normality

3.4 Discussion

It is often assumed that a log transformation is adequate for providing normally distributed PET SUVs extracted from tumors (53); however, this chapter presented cases where the log transformation was not optimal for producing normal SUV distributions. Through optimization of the Box-Cox transformation, we identified transformations leading to normally distributed SUVs, even in cases where the log transformation failed to provide normal distributions. Importantly, the results showed that therapy can alter the optimal transformation leading to normally distributed SUVs. This indicates that although a transformation may provide

sufficiently normal SUV distributions at one timepoint (prior to therapy) it may not do so at another timepoint (post therapy).

After applying optimal Box-Cox transformations to FLT SUVs, both pre and post treatment distributions were normally distributed. After applying optimal Box-Cox transformations to FDG SUVs, both pre and post treatment distributions were normally distributed, providing further validation of the Box-Cox transformation methodology. After log transforming FLT SUVs, the pre treatment distribution was normally distributed but the post treatment distribution approached non-normality ($P = 0.05$). After log transforming the FDG SUVs, the pre treatment deviated significantly from normality ($P<0.01$) but the post treatment was normally distributed. These results indicate therapy can alter the lognormal behavior of SUV distributions for both FDG and FLT. This underlies the importance of assessing whether transformed SUV distributions are sufficiently normal before performing statistical tests that require distribution normality.

The relatively high coefficients of variation for the tumor SUV distributions that have a lower bound of zero suggest non-normal behavior; this is further supported by relatively high values of skewness and excess kurtosis. Some have speculated that tumor SUV distributions deviate from normality since the morphologic features of tumor vasculature follow lognormal distributions (53). Given the deviation from normal and lognormal behavior found in this study for both PET tracers it seems likely physiologic factors in addition to vascular morphology are influencing the behavior of tumor SUV distributions. For example, the distribution of cell densities across different tumors or the distribution of tracer phosphorylation rates across different tumors could impact the behavior of tumor SUV distributions. Furthermore, SUV data that is compiled from multiple institutions will be influenced by differences in PET scanners and

imaging protocols across institutions that could alter the behavior of underlying SUV distributions (83,84).

For both FLT and FDG SUV_{max} distributions, the skewness and kurtosis increased during therapy. An increase in kurtosis implies a greater number of outliers; this accompanied by an increase in skewness indicates an increase in the number of outliers that are greater than the mean. Thus, for both patient cohorts in this study, therapy led to an increase in the number of SUV outliers that were greater than the mean (this increase is evident in **Figure 8**a and **Figure 8**d). The increase in positive outliers from pre to post therapy may represent resistant tumors that are more refractory to therapy relative to the rest of the tumor population. This effect led to a decrease in the optimal Box-Cox transformation parameter from pre to post treatment for both patient cohorts. This result indicates selection of the optimal normal transformation will likely change depending on whether analysis is performed on SUVs extracted before, during, or after therapy. However, this does not rule out the possibility that a single transform may be adequate for providing normal distributions at pre and post treatment. If one desired to analyze multiple timepoints with the same transform, the Box-Cox optimization could be modified to take into account the distributions from all timepoints simultaneously. For example one could identify the transformation parameter that maximizes the minimum Shapiro Wilk P-value resulting from the transformed distributions.

Oftentimes changes in PET SUVs are used to characterize tumor responses to therapy (19,25,56,85). This may require analysis of negative changes in tumor SUV metrics as a result of treatment. One of the limitations of the one-parameter Box-Cox transformation is that it cannot be used to transform distributions with negative values. However, one could still assess changes in SUVs by performing the Box-Cox transformation prior to calculating changes i.e.

perform a normal transformation on the SUVs and then calculate changes on the transformed scale. This would require that the same transformation be applied to both the pre and post timepoints. Since the optimal transformation parameter decreased for both FLT and FDG SUV distributions from pre to post treatment, assessing changes across timepoints may require the optimization be modified so that a single normal transformation is found for both the pre and post treatment SUV distributions simultaneously.

3.5 Conclusion

In this chapter, Box-Cox transformations were utilized to identify the optimal normal transformations for FLT and FDG SUV distributions extracted from tumors before and after treatment. Importantly, it was showed that SUV distributions can significantly change from pre to post treatment, indicating the optimal transformation leading to a normal distribution will likely change during the course of therapy. These normal SUV transformations enable powerful parametric statistical modelling for analyzing correlated measurements and enable use of other parametric statistical tests (t-tests, linear regression, analysis of variance, etc.) when analyzing PET SUVs. The results from this chapter will be utilized to enable parametric statistical modelling in Chapters 4 and 6 of this dissertation.

Section II FLT PET response assessment in anti-angiogenic therapy

Angiogenesis is the process of new blood vessel formation and maintenance that is primarily activated during periods of human growth (20,86). In adulthood, angiogenesis has a limited role in normal human physiology (87). The discovery that tumors must activate angiogenic processes to grow beyond 2-3 mm in size led to the development of anti-angiogenic therapies (86). Angiogenesis was an enticing therapeutic target as all tumors require the angiogenic process for growth and it is a process not normally activated in healthy tissues. Thus, targeting the angiogenesis pathway was thought to have a high therapeutic index i.e. little adverse effects on healthy tissues and ubiquitous inhibition of tumor growth. Excitement for anti-angiogenic agents grew in 2004 following the FDA approval of the anti-angiogenic agent bevacizumab for treating advanced colorectal cancer. This led the then FDA commissioner to herald anti-angiogenic therapy as the "fourth modality of cancer treatment" following surgery, chemo, and radiation therapy (88).

The vascular endothelial growth factor (VEGF) pathway is the most common target of anti-angiogenic agents due to its well documented role in angiogenesis (20). Anti-angiogenic drugs targeting the VEGF ligand and VEGF receptors (VEGFRs) on endothelial cells have had the most success and have been shown to slow tumor growth for a number of different cancers (20). Bevacizumab, a monoclonal antibody targeting the VEGF ligand, was one of the first anti-angiogenic agents showing clinical success but only when combined with chemotherapy (2,3,89,90). This success was followed by development of VEGFR tyrosine kinase inhibitors (VEGFR-TKIs) that showed improved single agent activity compared with bevacizumab.

VEGFR-TKI monotherapies prolonged overall and progression free survival in multiple metastatic cancers (91-95).

Despite initial responses to VEGFR-TKI treatments, brief periods of efficacy are always followed by disease resistance and progression (20,86,96). Thus, development of novel therapeutic strategies to prolong patient benefit and delay the onset of disease resistance is an active area of research. Given the success of VEGFR-TKIs as monotherapy, a logical next step to improve efficacy of these agents was combination trials with cytotoxic chemotherapy. This was based on the clinical successes that were found when concurrently administering VEGF-ligand targeting agents like bevacizumab with chemotherapies (2-4). However, phase III clinical trials administering concurrent VEGFR-TKI and chemotherapy demonstrated negative results (5,97-102). A more thorough investigation of mechanistic actions of anti-angiogenic therapies would provide crucial understanding of why some combination therapies fail, while others prove effective, leading to more efficient development of combination strategies. Section II of this dissertation will utilize FLT PET to characterize the mechanistic actions of anti-angiogenic agents. Through this work we were able to provide explanation for the negative results when concurrently administering VEGR-TKIs with chemotherapy and devise a novel treatment paradigm for combining VEGFR-TKIs with chemotherapy.

FLT PET has been utilized to assess the effects of anti-angiogenic therapy in a number of clinical trials (25,26,28,52,85,103-106). It has shown particular promise for assessing pharmacodynamic effects of VEGFR-TKIs (25,85,105,106). During continuous treatment with VEGFR-TKIs patients experienced a decrease in tumor FLT uptake. However, this decrease was followed by a rebound in FLT uptake just days after a break in VEGFR-TKI dosing, presumably due to rapid increases in tumor cell proliferation. This rebound, known as the

VEGFR-TKI withdrawal flare, was independent of tumor type. This led some to hypothesize that the withdrawal flare can be exploited by 'synchronizing' chemotherapy during VEGFR-TKI treatment breaks to maximize the therapeutic index of cell cycle-specific chemotherapy (25,85,105). This sequential treatment strategy, i.e. applying cell-cycle specific chemotherapy during VEGFR-TKI treatment breaks to specifically target the withdrawal flare, has not been studied clinically.

The work in this thesis utilizes FLT PET to further assess whether a sequential VEGFR-TKI and chemotherapy treatment paradigm might be advantageous. This includes assessment of the withdrawal flare in multiple intermittent VEGFR-TKI treatment cycles (Chapter 4: Assessing pharmacodynamic effects of intermittent anti-angiogenic therapy using static FLT PET) and utilization of dynamic FLT PET scanning to further characterize vascular and proliferative changes occurring in tumors during VEGFR-TKI therapy (Chapter 5: Dynamic FLT PET to investigate concurrent changes in tumor vasculature and cell proliferation during anti-angiogenic therapy). The anti-angiogenic therapy section of this dissertation concludes with the results from Chapters 4 and 5 being utilized to develop and assess a novel treatment paradigm (Chapter 6: Assessing the pharmacodynamic effects of sequential VEGFR-TKI therapy and chemotherapy with FLT PET).

Chapter 4: Assessing pharmacodynamic effects of intermittent anti-angiogenic therapy using static FLT PET and plasma VEGF

4.1 Motivation

Axitinib is a VEGFR-TKI that blocks VEGFRs-1, 2, and 3. It is a second generation anti-angiogenic agent that has shown improved potency over previous VEGFR-TKIs and has been approved for the treatment of metastatic renal cell carcinoma (107). Despite the promise of axitinib, patients eventually acquire resistance to treatment. This has motivated a number of studies investigating axitinib pharmacokinetics and pharmacodynamics in an effort to develop improved treatment strategies. For example, pharmacokinetic modelling showed that higher doses of axitinib in renal cell carcinoma patients tolerating therapy was associated with improved response rate (108). Alternatively, it has been hypothesized that combining VEGFR-TKI treatments such as axitinib with other types of treatments might improve efficacy (105). Based on results from previous studies (25,85), it has been hypothesized that the treatment withdrawal flare, characterized by a rebound in tumor cell proliferation during the VEGFR-TKI washout period, may offer an opportune time to apply synergistic cell-cycle specific chemotherapy (25,85). However, further characterization of VEGFR-TKI pharmacodynamic effects during intermittent regimens is necessary to determine the feasibility of sequential treatment strategies. This includes determining whether the withdrawal flare occurs in later cycles of intermittent treatment regimens.

This chapter evaluates the withdrawal flare during multiple intermittent treatment cycles with the VEGFR-TKI axitinib. FLT-PET/CT imaging and plasma measurements of VEGF ligand levels will be used to characterize the pharmacodynamic effects of treatment, including

the withdrawal flare. Correlations between PET data and VEGF ligand levels will be assessed using normal data transformations and mixed effects models. The ultimate clinical goal is to exploit the withdrawal flare to improve therapeutic index of cell–cycle specific chemotherapy for applications in the neoadjuvant or metastatic setting.

4.2 Methodology

Patient Population

Patients with histologically or cytologically confirmed solid malignancy (excluding lymphoma) that was metastatic or unresectable and for which no standard therapy existed were included in this study. Patients with prior anti-VEGF treatment were excluded. Other exclusion criteria include concomitant coumarin-derivative anticoagulation, history of brain metastases, and any concomitant use of CYP3A4 or CYP1A2 inducers. All patients signed informed consent documents approved by the Institutional Review Board at the University of Wisconsin. Additional approval by the Radioactive Drug Research Committee at the University of Wisconsin was obtained given use of an experimental tracer. This study was conducted in accordance with the Declaration of Helsinki.

Drug administration and study design

Patients underwent VEGFR-TKI treatment with the standard FDA approved 5 mg twice daily (BID) axitinib. All patients underwent three week treatment cycles with axitinib taken orally, twice daily with food on days 1-14, followed by a one week drug break (days 15-21). Patients underwent up to 6 FLT PET/CT scans at three timepoints during both cycles 1 and 3 (**Figure 9**). No imaging was obtained during cycle 2. The rationale for FLT PET/CT imaging

during cycle 3 was to determine whether the withdrawal flare was present in later cycles of intermittent treatment while still maintaining an evaluable number of patients on the study. The imaging timepoints for cycle 1 and cycle 3 included: (i) baseline (-3 to 0 days prior to treatment), (ii) peak drug exposure (12 to 14 days into the dosing period), and (iii) near end of drug washout period (5 to 7 days into the treatment break). In order to be evaluable for FLT PET/CT imaging patients needed to complete greater than 90% of scheduled axitinib doses prior to completion of the third FLT PET/CT scan. All patients were assessed for progression every three cycles of therapy using RECIST 1.1 guidelines. Patients were also assessed for progression by a treating physician, which was based on a number of factors available to the physician including adverse side-effects of treatment.

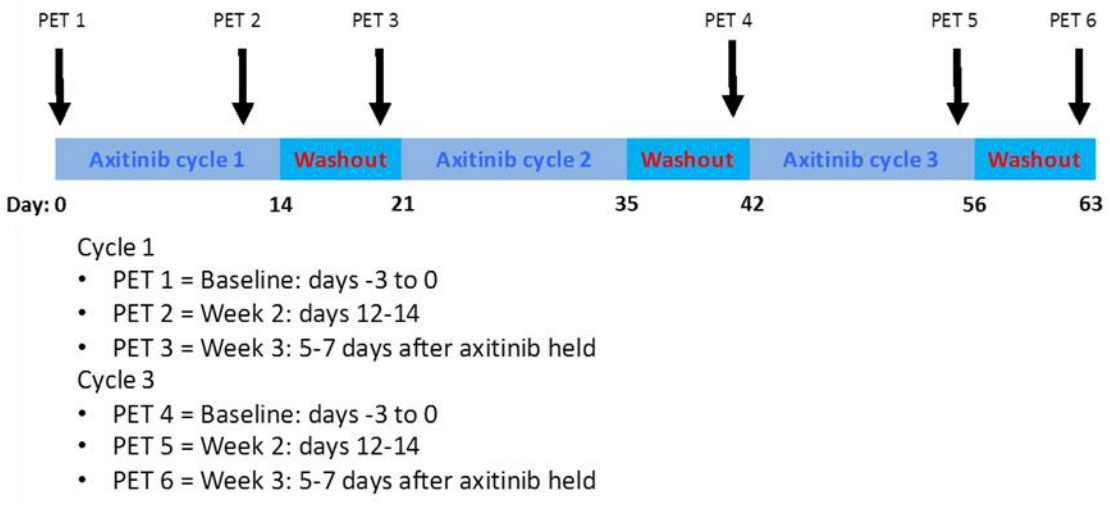

Figure 9: Treatment schedule and FLT PET/CT imaging timepoints

FLT PET/CT scans and analysis

Patients were injected with up to 300 MBq of FLT. FLT PET/CT scans were initiated 60 minutes post injection (7 bed positions, 5 minutes per bed position) on a Discovery LS PET/CT

scanner (GE, Waukesha WI). An ordered-subsets expectation maximization (OSEM) algorithm was used for three-dimensional image reconstruction with CT data used for attenuation correction. Parameters for the reconstruction included: 256x256 matrix, 35 subsets, 2 iterations, and a 3-mm Gaussian post-filter. The resulting image was a 256x256x263 matrix with voxel dimensions of 2.73, 2.73, and 3.27 mm, respectively.

Each tumor (up to five per patient) was identified by a nuclear medicine physician using both PET and CT images. Manual segmentation of tumors was performed by the same individual for all scans using Amira software (Visage Imaging Inc.). Imaging metrics analyzed included SUVs, which were corrected for injected activity and patient weight (resulting in SUVs with units of g/mL). SUVs were calculated for each voxel and summarized for all tumors in each patient giving global SUVs (including SUV_{mean}, SUV_{max}, and SUV_{total}). SUV_{mean} was defined as the average SUV of all tumors within a patient. SUV_{max} was defined as the SUV in the voxel with highest SUV of all tumors within a patient. SUV_{total} was defined as the product of the sum of SUVs from all tumors within a patient and the voxel volume. In addition to extracting SUVs for each time point, relative percent changes in SUVs were calculated for the treatment and washout periods within cycles 1 and 3. Equation 12 shows example calculation for the relative change in SUV during the treatment period in cycle 1.

$$SUV_{\%} = \frac{SUV_{PET\ 2} - SUV_{PET\ 1}}{SUV_{PET\ 1}} \times 100\% \qquad \text{Eq 12}$$

VEGF and Axitinib Plasma Concentrations

Plasma samples for analysis of axitinib and vascular endothelial growth factor ligand (VEGF) concentrations were collected on the same days as PET/CT scans:-3 to 0 days prior to dosing, after 12 to 14 days of dosing (week 2) and after 5 to 7 days of drug washout (week 3).

VEGF concentrations were measured by a commercially available 96-well plate quantitative sandwich immunoassay (Quantikine® human VEGF, R & D Systems, Minneapolis, MN) according to manufacturer's instructions. Axitinib plasma concentrations were measured by a validated LC/MS/MS (85).

Statistical Methods

Relative changes in SUVs and plasma markers were summarized in terms of medians and ranges. Since the distributions of the relative changes in SUVs and plasma markers were highly skewed, the nonparametric Wilcoxon signed-rank test was utilized to evaluate changes across time points. A linear mixed effects model with subject specific random effects was used to examine the association between SUVs and VEGF measurements. A compound symmetry correlation structure was utilized to account for correlation of measurements arising from the same patient. Both the SUV and VEGF distributions were normally transformed before inclusion in the linear mixed effects model. All reported P-values are two-sided and $P<0.05$ was used to define statistical significance. Data analysis was conducted using R software version 3.4.0.

4.3 Results

Patient Characteristics

Sixteen patients were enrolled on this study and underwent FLT PET scanning (**Table 7**). Two of the patients completed only the baseline FLT PET/CT scan and were not included in the imaging analysis. The remaining fourteen patients completed three or more of the scheduled FLT PET/CT scans. The median cycles of therapy received was 4 (range 2 to 18).

Table 7: Patient Demographics

	Patients N=16
Age (years)	
Median (range)	70 (38-82)
Number of Patients	
Male	11 (69%)
Female	5 (31%)
Primary Disease site	
Prostate	5 (31%)
Colorectal	3 (19%)
Urothelial	2 (13%)
Ovarian	1 (6%)
Lung	1 (6%)
Other	4 (25%)
Number of organs with metastases	
1	5 (31%)
2	5 (31%)
3+	6 (38%)

FLT PET/CT Imaging

Figure 10 highlights a representative tumor that had decreases in SUVs during dosing periods and increases in SUVs during washout periods in both cycle 1 and cycle 3. Although the tumor in **Figure 10** shows increased SUV in cycle 3 relative to cycle 1, as a whole, the population of patients didn't exhibit significantly different SUVs when comparing corresponding time points in cycle 1 vs. cycle 3 e.g. for SUV_{mean}: Baseline cycle 1 vs. Baseline cycle 3, P = 0.90; Peak Drug cycle 1 vs. Peak Drug cycle 3, P = 1; Washout cycle 1 vs. Washout cycle 3, P = 0.50 (**Figure 11**).

Table 8 summarizes median percent changes in SUV_{mean}, SUV_{max}, and SUV_{total} during treatment and washout periods for pharmacodynamic patients. SUV_{mean} decreased significantly during dosing period in both cycle 1 (median -15%, P = 0.02) and cycle 3 (median -21%, P =

0.008). No statistical significant differences were found when comparing the percent change in SUV_{mean} during dosing period in cycle 1 vs. cycle 3 (P = 0.8). SUV_{mean} significantly increased during washout period in both cycle 1 (median +20%, P < 0.001) and cycle 3 (median +27%, P = 0.03). No significant difference was found when comparing the percent change in SUV_{mean} during washout period in cycle 1 vs. cycle 3 (P = 0.7). Similar trends occurred for SUV_{max} and SUV_{total}.

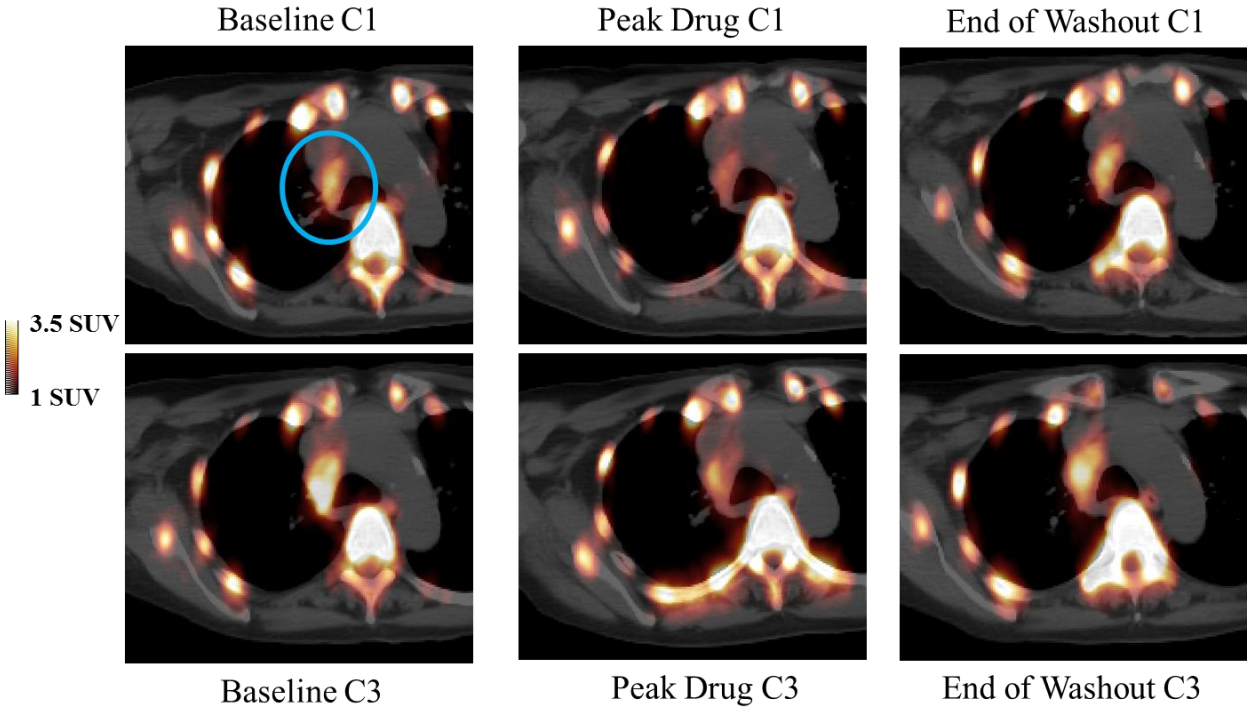

Figure 10: Axial PET/CT slice with increased SUV in a metastatic lymph node (blue ellipse). Note reduced SUV at peak drug in both cycle 1 and cycle 3, which subsides by the end of washout. C1 =cycle 1; C3 = cycle 3

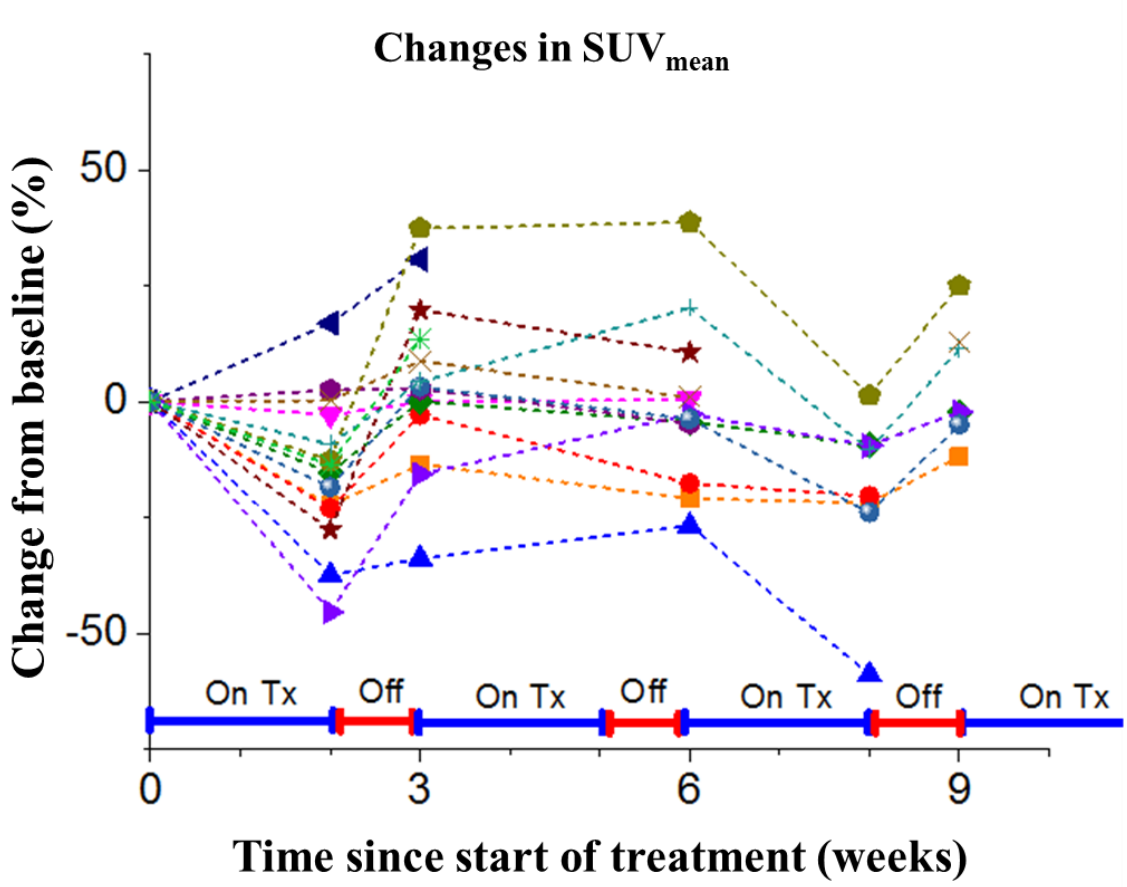

Figure 11: Changes in tumor SUV_{mean} for all patients across all six timepoints. No significant differences were evident in the changes seen in cycle 1 (0 to 3 weeks) vs. the changes in cycle 3 (6 to 9 weeks).

Table 8: Median percent changes in tumor SUV and plasma VEGF during dosing and washout periods (range shown in parenthesis).

	Median % change during drug dosing period		**Median % change during drug washout period**	
	Cycle 1 (n=14)	Cycle 3 (n=8)	Cycle 1 (n=14)	Cycle 3 (n=6)
SUV_{mean}	-15 *(-48 to +16)*	-21 *(-42 to -6)*	+20 *(+1 to +58)*	+27 *(+16 to +33)*
SUV_{max}	-23 *(-68 to +23)*	-26 *(-43 to -7)*	+28 *(-29 to +159)*	+33 *(+14 to +69)*
SUV_{total}	-49 *(-91 to +23)*	-23 *(-91 to -4)*	+50 *(-15 to +1492)*	+62 *(-14 to +1100)*
VEGF	+140 *(-40 to +3787)*	+193 *(+15 to +1363)*	-63 *(-95 to 0)*	-67 *(-82 to -39)*

Plasma VEGF concentration

The last row of **Table 8** summarizes the relative percent changes in plasma VEGF ligand levels. VEGF concentrations increased during dosing period in both cycle 1 (median +140%, P = 0.002) and cycle 3 (median +193%, P = 0.03). There was no difference between the percent changes in VEGF during dosing period for cycle 1 vs. cycle 3 (P = 0.1). VEGF concentrations decreased during washout in cycle 1 (median -63%, P < 0.001) and cycle 3 (median -67%, P = 0.25). There was no significant difference between the percent changes in VEGF during washout for cycle 1 vs. cycle 3 (P = 1.0).

A linear mixed effects model with VEGF as a predictor variable, demonstrated significant negative correlation (P<0.001) between log-transformed VEGF and SUV_{total} (slope = -0.42, 95%CI = -0.57 to -0.27). The fitted model and measured data are shown in **Figure 12**.

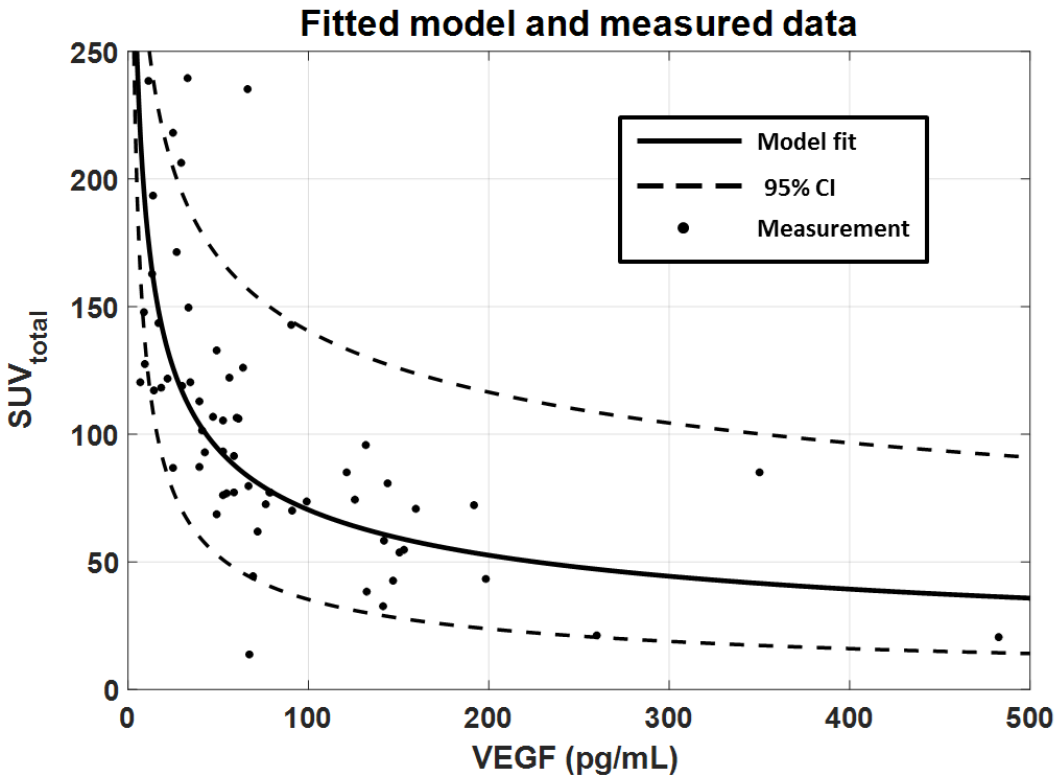

Figure 12: Tumor SUV_{total} as a function of plasma VEGF concentration is shown for both the measured data as well as the fitted linear mixed effects model. In general, higher VEGF measurements indicated a lower SUV_{total}. CI = confidence interval

Axitinib plasma concentration

The median plasma concentration of axitinib in cycle 1 week 2 (after 12-14 days of dosing) was 8 ng/mL (range 1 - 33 ng/mL). The median concentration in cycle 3 week 2 was 11 ng/mL (range 1 - 46 ng/mL). No significant difference in axitinib concentration during week 2 was found in cycle 1 vs cycle 3 (P = 0.6). Axitinib concentrations measured prior to dosing and after 5-7 days of washout were below the limit of quantification. No significant correlations were found between axitinib plasma concentrations and either plasma VEGF concentrations or SUV metrics.

4.4 Discussion

The results in this chapter suggest that diminished tumor cell proliferation during continuous anti-angiogenic dosing likely contributes to negative results of previous studies concurrently combining VEGR-TKI therapy and chemotherapy. However, an increase in tumor cell proliferation during drug washout periods offers a potential target for *sequential* combination chemotherapy.

Significant increases in tumor FLT uptake during VEGFR-TKI washout periods characteristic of an acute treatment withdrawal flare was observed in both cycle 1 and cycle 3. Furthermore, tumor FLT uptake during the third cycle of treatment was not significantly different than uptake in first cycle of treatment. These results suggest that the pharmacodynamic effect of axitinib is similar and consistent across multiple drug cycles. This effect is

characterized by decreases in tumor cell proliferation during dosing periods followed by subsequent increases during drug washout periods. These results suggest an intermittent VEGFR-TKI treatment regimen with cell-cycle specific chemotherapy applied during the VEGFR-TKI treatment breaks would be a rational treatment strategy.

Significant increases in plasma VEGF levels during dosing periods were followed by decreases in VEGF levels during the washout periods. This is in agreement with our previous study in a similar cohort of patients being treated with axitinib (108). Additionally this study shows these trends are present in both the first and third cycles of treatment with no significant differences between cycles. It has been hypothesized that acquired resistance to VEGR-TKI treatment might be attributed to increasing tumor secretion of the VEGF ligand; however, the results of this study showed no difference between VEGF plasma concentration in early and later cycles. This indicates some patients acquire resistance by means other than increased VEGF secretion, such as recruitment of additional angiogenic pathways to circumvent the VEGF pathway (96).

A significant negative correlation was found between FLT uptake metric SUV_{total} and plasma VEGF concentration. An increase in a patient's plasma VEGF concentration indicated a corresponding decrease in their SUV_{total}. This negative correlation could be explained by the fact that a greater degree of tumor VEGFR inhibition (leading to increased VEGF secretion and unbound VEGF) is accompanied by a greater drop in tumor cell proliferation. This confirms an on-target effect of axitinib and lends support to targeting the VEGF pathway to inhibit tumor cell proliferation and growth.

4.5 Conclusion

Response to axitinib included diminished FLT uptake during dosing periods followed by increased FLT uptake during drug washout periods. These changes were no different when comparing treatment cycle 1 versus cycle 3, suggesting that the pharmacodynamic effect of intermittent axitinib is similar across multiple drug cycles. This suggests that a sequential treatment regimen that applies chemotherapy during VEGFR-TKI washout periods may be synergistic capitalize on the withdrawal flare. Further correlation between FLT PET uptake and VEGF ligand levels is supportive of an on-target effect of VEGFR-TKI axitinib, leading to diminished FLT uptake and increase in circulating VEGF ligand.

Chapter 5: Dynamic FLT PET to investigate concurrent changes in tumor vasculature and cell proliferation during anti-angiogenic therapy

5.1 Motivation

In the previous chapter we utilized static (single-timepoint) FLT PET imaging to estimate SUVs in tumors. In general, FLT SUVs have been shown to be correlated with reference standards of cell proliferation. However, this has not been assessed in the context of anti-angiogenic therapy where treatment may cause significant changes in tumor vasculature, potentially influencing SUVs independent of changes in cell proliferation. FLT compartmental modelling can be used to differentiate changes in tumor vasculature and cell proliferation, providing insight into the causes of SUV fluctuations during anti-angiogenic therapy. In this chapter we utilize dynamic FLT PET imaging with compartmental modelling to evaluate spatiotemporal changes in FLT kinetics in metastatic cancer patients undergoing anti-angiogenic therapy. Specifically, we will investigate concurrent vascular and proliferative changes occurring in tumors during VEGFR-TKI therapy with axitinib. We will compare the estimated kinetic parameters with the more simplified SUV metrics evaluated in the previous chapter. The results provide additional clinical insight relating to optimal combination strategies for VEGFR-TKIs and chemotherapies.

5.2 Methodology

Study design

Thirty-three patients with histologically or cytologically confirmed solid metastatic tumors for which no standard curative therapy exists were included in this analysis. For all patients, oral axitinib was administered continuously for two weeks followed by a scheduled one week treatment break (**Figure 13**). During the continuous VEGFR-TKI treatment weeks patients took 5 mg of axitinib twice daily. Patients underwent up to three dynamic FLT PET/CT scans during the first cycle of treatment including at: 1) baseline, 2) peak drug (after two weeks of continuous axitinib dosing), and 3) the end of drug washout (after a one week treatment break). Detailed methodology of the dynamic PET scanning and FLT compartmental modelling can be found in Chapter 3.

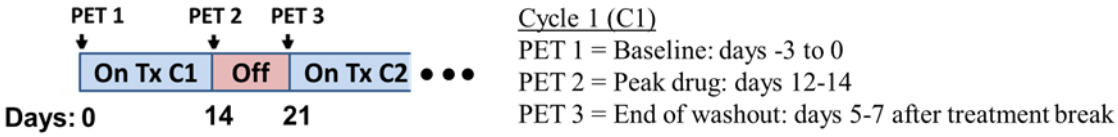

Figure 13: Dynamic PET scanning with FLT compartmental modelling was performed at three timepoints during the first cycle of VEGFR-TKI therapy.

Statistical Analysis

Significant changes in patient summarized FLT kinetic parameters were assessed using Wilcoxon signed-rank tests. Spearman correlation coefficients were used to assess relationships between changes in FLT PET kinetic parameters as well as relationship between kinetic parameters and SUVs. SUVs were extracted at early (0 to 20 minutes), mid (20 to 40 minutes), and late timepoints (60+ minutes) post-injection by averaging dynamic PET frames. P-values less than or equal to 0.05 were considered significant and all statistical analysis was performed in R software version 3.4.0.

5.3 Results

A total of thirty-three patients with soft-tissue metastatic tumors completed at least two PET scans at designated imaging timepoints. These patients had various types of metastatic cancers with the most common being carcinomas of the colon, prostate, and lung (**Table 9**).

Figure 14 shows an axial CT slice with a tumor parametric map overlay, demonstrating representative changes in FLT kinetic parameters. The parametric maps revealed spatial heterogeneity in tumor vasculature (V_b and K_1) and cell proliferation (K_i) that is altered during therapy. Tumor size as visualized on CT was relatively unchanged during the first treatment cycle; however, the results of the FLT kinetic analysis demonstrated notable changes in underlying tumor physiology. This included decreases in both vascular and proliferative FLT kinetic parameters during axitinib exposure weeks and increases in these parameters during axitinib washout.

Table 9: Patient characteristics

Characteristic	Number of patients
Total	33
Gender	
Male	23 (70%)
Female	10 (30%)
Prior anti-VEGF therapy	
Yes	12 (36%)
No	21 (64%)
Primary Cancer Histology	
Colorectal Adenocarcinoma	7 (21%)
Prostate Carcinoma	5 (15%)
Non-Small-Cell Lung Carcinoma	4 (12%)
Renal Cell Carcinoma	3 (9%)
Urothelial Carcinoma	2 (6%)
Breast Carcinoma	2 (6%)
Neuroendocrine	2 (6%)
Head and Neck Carcinoma	2 (6%)
Other*	6 (19%)

Tumors segmented for analysis	
1	11 (33%)
2	16 (49%)
3	4 (12%)
4	2 (6%)
FLT PET/CT scans completed	
Baseline	25 (76%)
Peak Drug	32 (97%)
End of Washout	31 (94%)

*** Other histologies included one of each: hepatocellular carcinoma, ovarian carcinoma, appendiceal carcinoma, squamous cell carcinoma, neurofibrosarcoma, and one of unknown primary cancer origin**

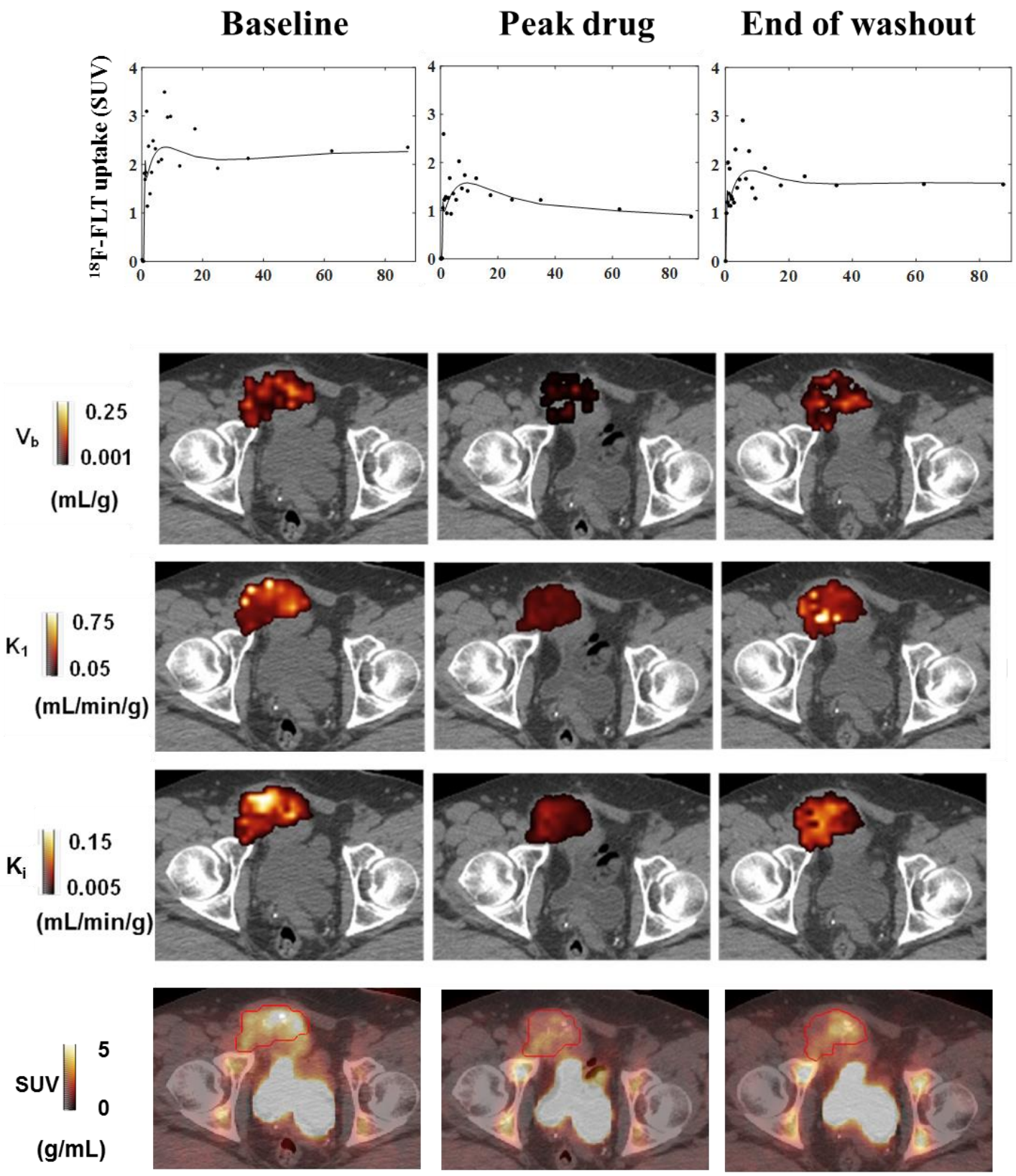
Baseline
Peak drug
End of washout
^{18}F-FLT uptake (SUV)
0
1
2
3
4
0
20
40
60
80
V_b
0.25
0.001
(mL/g)
K_1
0.75
0.05
(mL/min/g)
K_i
0.15
0.005
(mL/min/g)
SUV
5
0
(g/mL)

Figure 14: Spatiotemporal changes in tumor cell proliferation and vasculature during VEGFR-TKI treatment. The top row of images shows representative model estimated time activity curves, including measured SUVs for a pelvic tumor voxel from a patient with metastatic colorectal cancer at baseline, peak drug, and end of washout timepoints. The second, third, and fourth row of images show the corresponding FLT parametric maps overlaid on top of CT slices (data has been up-sampled to the resolution of CT scan for visualization). The second row of images shows changes in blood volume parameter V_b, the third row shows changes in the vascular perfusion/permeability parameter K_1, and the fourth row shows changes in the proliferative parameter K_i. The last row of images shows fused PET/CT images (final PET frame of dynamic scan).

Percent changes in kinetic parameters were calculated across the various imaging timepoints and are summarized in **Table 10**. Changes in kinetic parameter for each patient are shown in **Figure 15**a-d for V_b, K_1, and K_i and in **Figure 16**a-d for V_d and k_3. During axitinib exposure, the median value of all kinetic parameters decreased and the decrease was significant for K_1, k_3, and K_i. The majority of patients had simultaneous decreases in both vascular (V_b and K_1) and proliferative (K_i) kinetic parameters during axitinib exposure (**Figure 15**a); however, there was no significant correlation between the changes in the parameters. During axitinib washout, the median value of all kinetic parameters increased and the increase was significant for V_b, K_1, k_3, and K_i. The majority of patients experience simultaneous increases in both vascular and proliferative kinetic parameters during axitinib washout (**Figure 15**b).

From baseline to end of axitinib washout, there were no significant changes in any of the kinetic parameters, indicating that by the end of axitinib treatment breaks, many tumors resemble their pretreatment condition (**Figure 15**c). This is also supported by negative correlations between change in a given kinetic parameter during the axitinib exposure period and change in that same parameter during the axitinib washout period. These trends were strongest for the vascular kinetic parameters V_b (ρ=-0.70, $P<0.01$) and K_1 (ρ=-0.71, $P<0.01$) (**Figure 17**).

Table 10: Summary of changes in tumor kinetic parameters during axitinib treatment.

	Kinetic parameter	Median change (%)	Interquartile range (%)	Mean change (%)	Standard deviation (%)	P-value*
Baseline to peak drug (axitinib exposure)						
	V_b	-21	-60 to +14	-20	47	0.07
	K_1	-39	-51 to -22	-28	43	<0.01
	V_d	-11	-37 to +25	-3	48	0.45
	k_3	-33	-50 to -9	-24	42	0.01
	K_i	-37	-55 to -19	-32	36	<0.01
Peak drug to end of washout (axitinib washout)						
	V_b	+42	-12 to +177	+234	603	<0.01
	K_1	+46	+20 to +91	+61	66	<0.01
	V_d	+15	+1 to +29	+16	36	0.02
	k_3	+16	-8 to +53	+67	159	0.02
	K_i	+39	-4 to +82	+61	95	<0.01
Baseline to end of washout						
	V_b	-1	-23 to +38	+16	56	0.58
	K_1	-3	-13 to +28	+11	47	0.63
	V_d	-4	-18 to +21	+4	35	0.81
	k_3	-11	-37 to +25	+21	129	0.45
	K_i	-8	-35 to +30	+13	92	0.65

* P-value is from the Wilcoxon signed-rank test

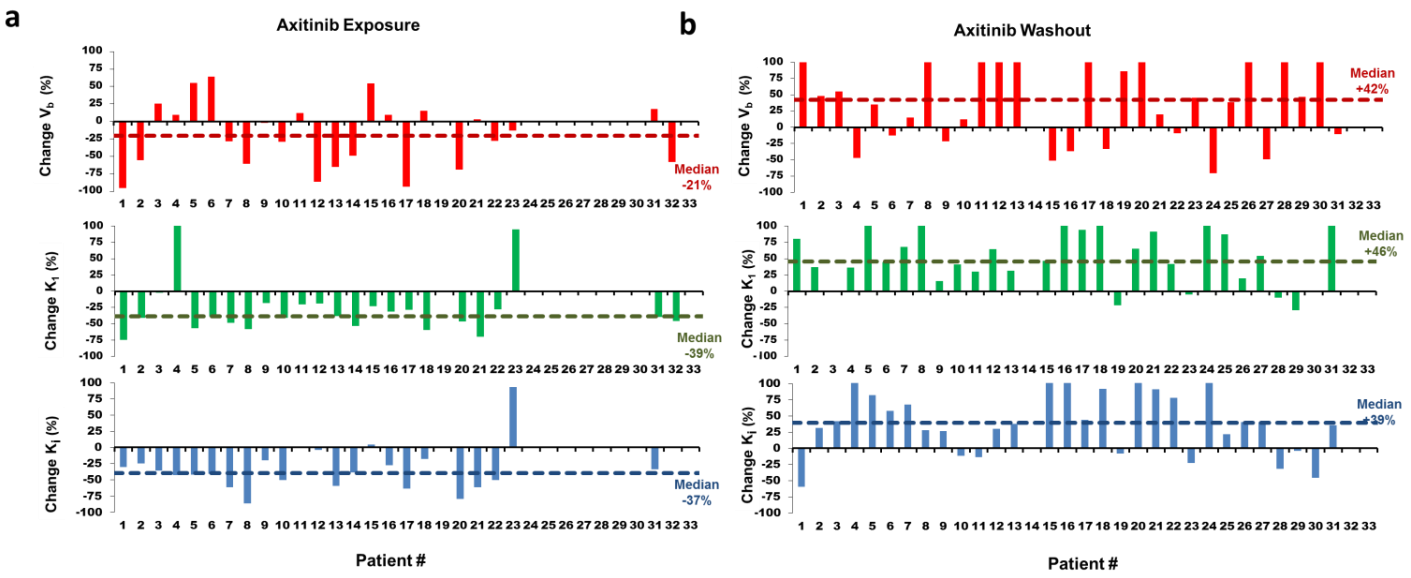

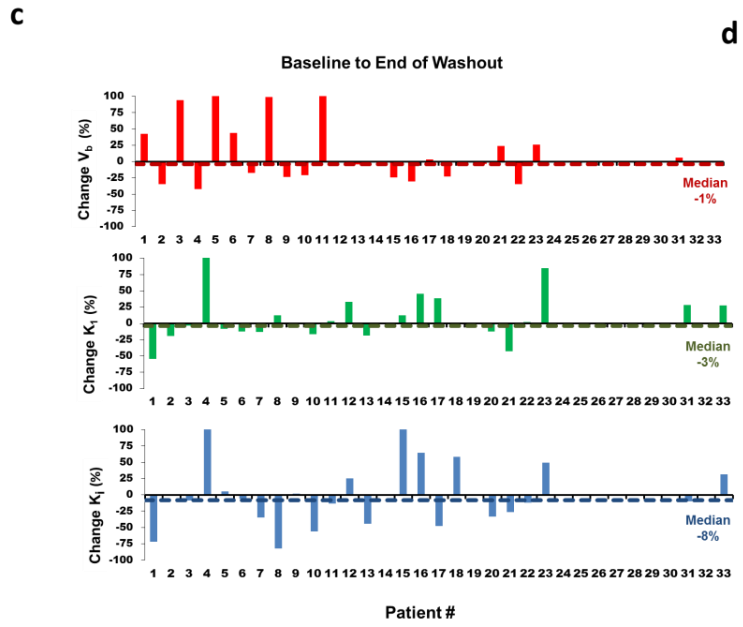

d

Patient #	PET FOV	Primary Cancer Histology
1	Pelvis	Squamous cell Carcinoma
2	Chest	Prostate carcinoma
3	Abdomen	Prostate carcinoma
4	Abdomen	Colorectal carcinoma
5	Pelvis	Appendiceal carcinoma
6	Chest	Ovarian carcinoma
7	Pelvis	Colorectal carcinoma
8	Chest	Prostate carcinoma
9	Chest	Non-small-cell lung carcinoma
10	Chest	Breast carcinoma
11	Abdomen	Colorectal carcinoma
12	Abdomen	Urothelial carcinoma
13	Chest	Colorectal carcinoma
14	Abdomen	Neuroendocrine
15	Abdomen	Prostate carcinoma
16	Chest	Colorectal carcinoma
17	Pelvis	Non-small-cell lung carcinoma
18	Chest	Neurofibrosarcoma
19	Chest	Breast carcinoma
20	Chest	Head and neck carcinoma
21	Chest	Colorectal carcinoma
22	Abdomen	Neuroendocrine
23	Abdomen	Prostate carcinoma
24	Chest	Non-small-cell lung carcinoma
25	Abdomen	Unknown primary
26	Chest	Head and neck carcinoma
27	Chest	Non-small-cell lung carcinoma
28	Abdomen	Renal cell carcinoma
29	Chest	Colorectal carcinoma
30	Abdomen	Renal cell carcinoma
31	Chest	Renal cell carcinoma
32	Abdomen	Hepatocellular carcinoma
33	Chest	Urothelial carcinoma

Figure 15: Change in individual patients' kinetic parameters (V_b, K_1, and K_i) during (a) axitinib exposure, (b) axitinib washout, and (c) from baseline to end of washout. A summary of dynamic PET FOVs and primary cancer histologies for each patient are provided for reference (d). Patients are numbered consistently for each insert and the blanks on the graphs represent patients that did not complete scans at the requisite timepoints. For inserts a-c the top graph shows changes in blood volume parameter V_b, the middle graph shows changes in the vascular perfusion/permeability parameter K_1, and the bottom graph shows changes in the proliferative parameter K_i. In general, patients experienced decreases in tumor FLT kinetic parameters during axitinib exposure (a), followed by increases during axitinib washout (b); this is indicated by median lines shown on each of the plots. Patients who experienced decrease in a given kinetic parameter during the axitinib exposure were more likely to have

increase in that kinetic parameter during the axitinib washout. Similarly, patients that experienced increase in a given kinetic parameter during the axitinib exposure were more likely to have decrease in that kinetic parameter during the axitinib washout (these negative correlations are shown in greater detail in Fig. 5). Note the vertical axis bounds are from -100% to +100% for ease of comparisons across plots; however, some patients had changes greater than +100%.

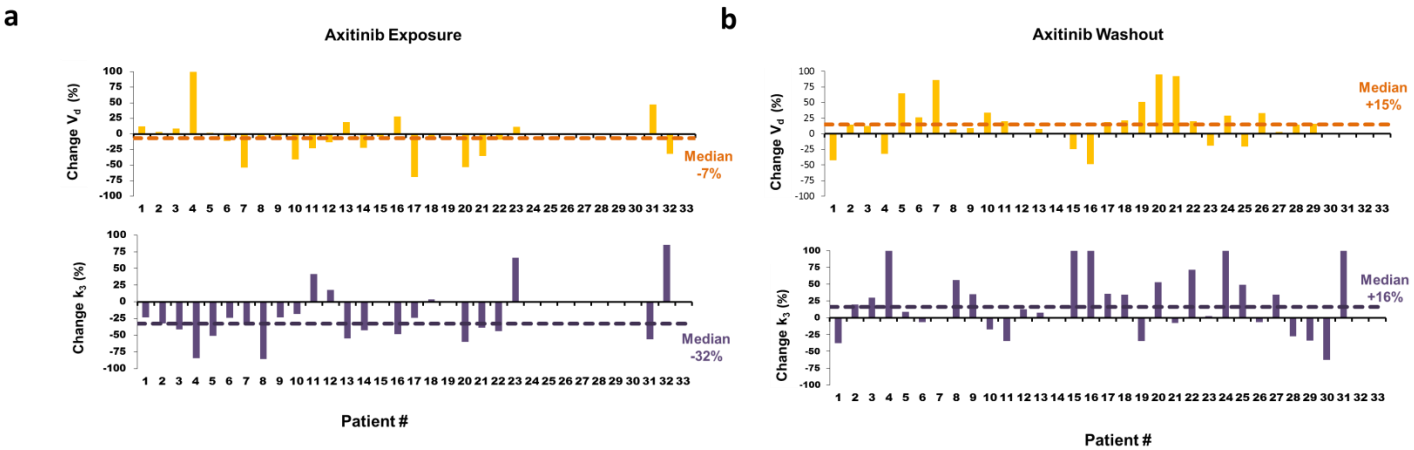

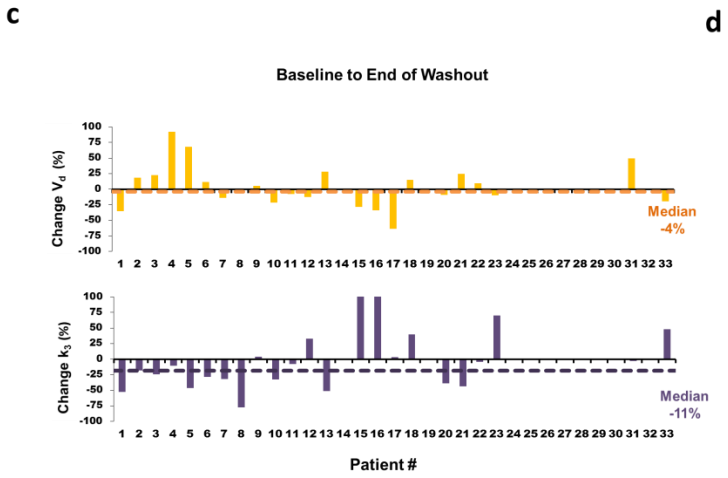

d

Patient #	PET FOV	Primary Cancer Histology
1	Pelvis	Squamous cell Carcinoma
2	Chest	Prostate carcinoma
3	Abdomen	Prostate carcinoma
4	Abdomen	Colorectal carcinoma
5	Pelvis	Appendiceal carcinoma
6	Chest	Ovarian carcinoma
7	Pelvis	Colorectal carcinoma
8	Chest	Prostate carcinoma
9	Chest	Non-small-cell lung carcinoma
10	Chest	Breast carcinoma
11	Abdomen	Colorectal carcinoma
12	Abdomen	Urothelial carcinoma
13	Chest	Colorectal carcinoma
14	Abdomen	Neuroendocrine
15	Abdomen	Prostate carcinoma
16	Chest	Colorectal carcinoma
17	Pelvis	Non-small-cell lung carcinoma
18	Chest	Neurofibrosarcoma
19	Chest	Breast carcinoma
20	Chest	Head and neck carcinoma
21	Chest	Colorectal carcinoma
22	Abdomen	Neuroendocrine
23	Abdomen	Prostate carcinoma
24	Chest	Non-small-cell lung carcinoma
25	Abdomen	Unknown primary
26	Chest	Head and neck carcinoma
27	Chest	Non-small-cell lung carcinoma
28	Abdomen	Renal cell carcinoma
29	Chest	Colorectal carcinoma
30	Abdomen	Renal cell carcinoma
31	Chest	Renal cell carcinoma
32	Abdomen	Hepatocellular carcinoma
33	Chest	Urothelial carcinoma

Figure 16: Change in patients' kinetic parameters (k_3 and V_d) during axitinib exposure (a), axitinib washout (b), and from baseline to end of washout (c). A summary of dynamic PET FOVs and primary cancer histologies for each patient are provided for reference (d). Patients are numbered consistently for each insert and the blanks on the graphs represent patients that did not complete scans at the requisite timepoints. For inserts a-c, the top graph shows changes in V_d and the bottom graph shows changes in k_3. In general, patients experienced decreases in k_3 (P=0.01) during axitinib exposure (a) and increases in k_3 (P=0.02) and V_d (P=0.02) during axitinib washout (b); this is indicated by median lines shown on

each of the plots. Note the vertical axis bounds are from -100% to +100% for ease of comparisons across plots; however, some patients had changes greater than +100%.

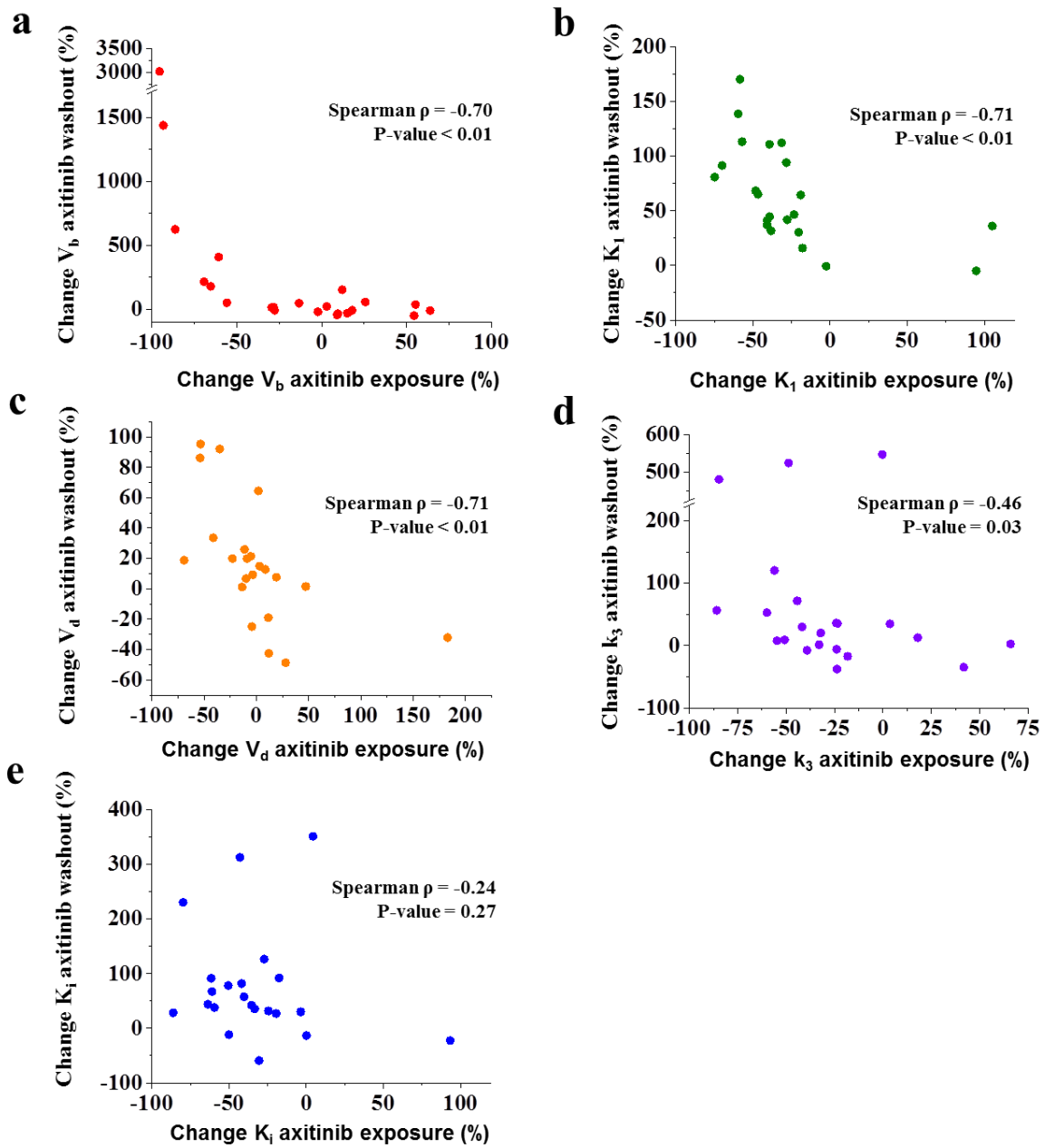

Figure 17: Correlation plots showing relationship between change in a given kinetic parameter during the axitinib exposure period and change during the axitinib washout period. Spearman correlation coefficients and corresponding P-values are also shown for V_b (a), K_1 (b), V_d (c), k_3 (d), and K_i (e). Patients that experienced large decreases in V_b, K_1, or V_d during axitinib exposure were more likely to experience large increases in these parameters during axitinib washout.

Oftentimes, simplified methods such as the SUV are used in place of more rigorous kinetic analysis. Typically SUVs are measured from a static PET scan performed at a single timepoint following injection of a radiotracer; thus, it is critical to ensure the appropriate timepoint is chosen so the physiology of interest is captured by the SUVs.

Table 11 shows correlation between relative FLT kinetic parameters and relative SUVs extracted at early, mid, and late timepoints following radiotracer injection. In general, SUVs measured at an early timepoint post-injection, were significantly correlated with vascular kinetic parameters (V_b and K_1). SUVs measured at the mid and late timepoints post-injection were significantly correlated with the proliferative parameter (K_i). In nearly all cases, SUVs were significantly correlated with kinetic parameter V_d.

Table 11: Spearman correlation coefficients describe relationship between SUVs and kinetic parameters

	SUV early (frames 0-20 min averaged)			**SUV mid (frames 20-40 min averaged)**			**SUV late (60+ min; final dynamic frame)**		
	Axitinib exposure	Axitinib washout	Baseline to end wash.	Axitinib exposure	Axitinib washout	Baseline to end wash.	Axitinib exposure	Axitinib washout	Baseline to end wash.
Vb	*0.77 (<0.001)**	*0.47 (0.01)*	0.11 (0.60)	0.39 (0.06)	-0.01 (0.95)	-0.07 (0.75)	*0.54 (0.007)*	0.03 (0.86)	0.03 (0.87)
K1	*0.57 (0.004)*	*0.45 (0.01)*	0.10 (0.66)	0.31 (0.14)	*0.42 (0.02)*	0.20 (0.36)	0.18 (0.39)	0.33 (0.07)	0.17 (0.42)
Vd	*0.42 (0.04)*	*0.38 (0.04)*	*0.48 (0.02)*	*0.74 (<0.001)*	*0.70 (<0.001)*	*0.43 (0.04)*	*0.68 (<0.001)*	0.35 (0.06)	*0.60 (0.003)*
k3	0.13 (0.56)	-0.06 (0.76)	-0.09 (0.68)	0.04 (0.85)	0.14 (0.47)	0.20 (0.36)	0.02 (0.91)	0.13 (0.50)	0.07 (0.72)
Ki	0.41 (0.05)	0.14 (0.48)	0.33 (0.11)	*0.47 (0.02)*	*0.59 (<0.001)*	*0.66 (<0.001)*	*0.51 (0.01)*	*0.46 (0.01)*	*0.53 (0.01)*

*P-value shown in parenthesis

5.4 Discussion

The purpose of this chapter was to utilize dynamic FLT PET imaging to provide greater understanding of the clinical pharmacodynamics of VEGFR-TKIs, including the interplay between vascular and proliferative changes occurring in tumors. Two prior clinical studies have utilized dynamic imaging to assess vasculature pharmacodynamics during treatment with the VEGFR-TKI axitinib (109,110). In a phase I study, Liu et al. reported reductions in vascular perfusion and permeability in 13/17 (76%) patients' tumors after two days of continuous treatment with axitinib as measured with DCE-MRI (*12*). Similarly, the current chapter showed decreases in vascular perfusion and permeability after two weeks of continuous axitinib exposure, with 20/24 (83%) patients experiencing decreases in FLT kinetic parameter K_1. In a phase II study, Lo et al. showed decreases in fractional blood volume in 10/15 (67%) hepatic tumors following two weeks of continuous axitinib treatment as measured with DCE-US (110). The results in this chapter also showed decreases in fractional blood volume after two weeks of continuous axitinib exposure with 15/24 (63%) patients experiencing decreases in FLT kinetic parameter V_b. The fact that three different imaging modalities independently obtained similar findings regarding vascular changes during axitinib therapy provides strong evidence of axitinib successfully targeting tumor vasculature *in vivo* and demonstrates the potential value of dynamic FLT PET imaging for evaluating emerging anti-angiogenic agents. It is worth noting that in this analysis it is assumed FLT is similar to thymidine in that the tracer is rapidly transported from the blood into the cell and therefore K_1 is primarily determined by blood flow (41,70,111). Although we acknowledge other factors such as changes in vascular permeability may also affect K_1 (48,71).

The advantage of utilizing dynamic FLT PET is that in addition to providing insight into vasculature pharmacodynamics, it enables concurrent assessment of proliferative changes. Decreased tumor cell proliferation has been a documented effect of axitinib and other VEGFR-TKIs in preclinical studies (112,113). This study demonstrated decreases in tumor cell proliferation after two weeks of continuous axitinib treatment as measured by the FLT kinetic parameter K_i. These results shed insight into the clinical effects of axitinib. It suggests concurrent treatment of axitinib with chemotherapies may not be synergistic due to the reduction in tumor cell proliferation caused by VEGFR inhibition. This may be the reason most studies are reporting negative results when co-administering VEGFR-TKIs and cell-cycle specific chemotherapies (5,97,98).

Increases in both vascular and proliferative FLT PET kinetic parameters were observed during the axitinib washout period, implying rebound in the malignant nature of the tumor during treatment breaks. Given the effective plasma half-life of axitinib is 2 to 6 hours, the PET scans performed at the end of the washout period occur long after the drug has been excreted from the body (109,114). This corroborates findings of previous studies describing increases in tumor vasculature and cell proliferation during VEGFR-TKI washout periods (25,115,116). Initially the rationale for including these treatment breaks was to decrease drug-related toxicities (117); however, this washout period may be an opportune time to apply synergistic therapies. The increased cell proliferation and vasculature during VEGFR-TKI washout periods offers a potential target for combination therapies applied sequentially i.e. during VEGFR-TKI treatment breaks. Interestingly, negative correlations were found between changes in the tumor vasculature during axitinib exposure and changes in the tumor vasculature during axitinib washout. This suggests that changes in FLT PET kinetic parameters during the axitinib exposure

period could be used to predict which patients will experience a vascular rebound during planned treatment breaks. In theory, patients with rebound in the malignant state of the tumors during treatment breaks would benefit the most from sequential therapy.

Relative changes in FLT SUVs measured prior to 20 minutes post-injection were moderately correlated with relative changes in the vascular parameters K_1 and V_b. Relative changes in FLT SUVs measured after 20 minutes post-injection were moderately correlated with relative changes in the proliferative parameter K_i. These findings are similar to results from other studies that have assessed the relationship between the FLT SUVs and kinetic parameters in greater detail (40,64).

5.5 Conclusion

Dynamic FLT PET was used to investigate the mechanistic actions of the VEGFR-TKI axitinib in patients with advanced solid malignancies. Axitinib exposure led to decreases in both proliferative and vascular FLT PET kinetic parameters that may antagonize treatment with concurrent chemotherapy. Increases in proliferative and vascular FLT PET kinetic parameters during axitinib washout suggests rebound in the malignant nature of tumors, indicating VEGFR-TKI treatment breaks may be an optimal time for scheduling synergistic chemotherapy. The results indicate dynamic FLT PET imaging provides a valuable tool for concurrently evaluating vascular and proliferative changes in tumors during anti-angiogenic therapy and can facilitate development of improved therapeutic strategies.

Chapter 6: Assessing the pharmacodynamic effects of sequential VEGFR-TKI therapy and chemotherapy with FLT PET

6.1 Motivation

The previous two chapters provided evidence that treatment breaks in VEGFR-TKI dosing lead to increased tumor cell proliferation (withdrawal flare) that offers an opportune time to apply synergistic cell-cycle specific chemotherapy. This chapter investigates the sequential treatment approach, using a VEGFR-TKI in combination with cell-cycle specific chemotherapy. The aims were to assess the safety, tolerability, and pharmacodynamic effects of this sequential treatment strategy. Serial FLT PET/CT scans and plasma VEGF measurements were acquired to assess differences between pharmacodynamic effects in cycle 1 (after VEGFR-TKI exposure) and pharmacodynamic effects in cycle 2 (after sequential chemotherapy and VEGFR-TKI exposure).

6.2 Methodology

Study Design

Patients with histologically or cytologically confirmed solid malignancies that were metastatic or unresectable were included in this study. Informed consent was obtained from all patients prior to their participation and the study was approved by the Institutional Review Board at the University of Wisconsin.

X-82 (VEGFR-TKI) was provided to patients in 100 mg tablets. Patients underwent 1:1 randomization to two X-82 dose levels; in the high dose cohort, patients took 400 mg X-82 once daily and on the low dose cohort, patients took 200 mg X-82 once daily. Treatment cycles for all patients consisted of continuous X-82 dosing on days 1 to 14 followed by a break in X-82 dosing

on days 15 to 21; docetaxel was administered intravenously (75 mg/m^2) on day 21 of each treatment cycle (**Figure 18**). Patients continued on treatment until radiographic disease progression, clinical progression (based on physician discretion or serious drug-related adverse event), or patient withdrawal of consent. Patients were evaluated for response and radiographic progression every 3 cycles (9 weeks) using RECIST 1.1 guidelines (13). Objective response was defined as the best response measured by RECIST 1.1 and all measured partial responses were confirmed with repeat measurement within 4 weeks after the criteria for partial response were met. Pharmacodynamic assessments, including FLT PET/CT imaging and plasma VEGF measurements, were performed at four timepoints: 1) baseline, 2) maximum X-82 exposure, 3) maximum X-82 washout and 4) maximum X-82 exposure post docetaxel.

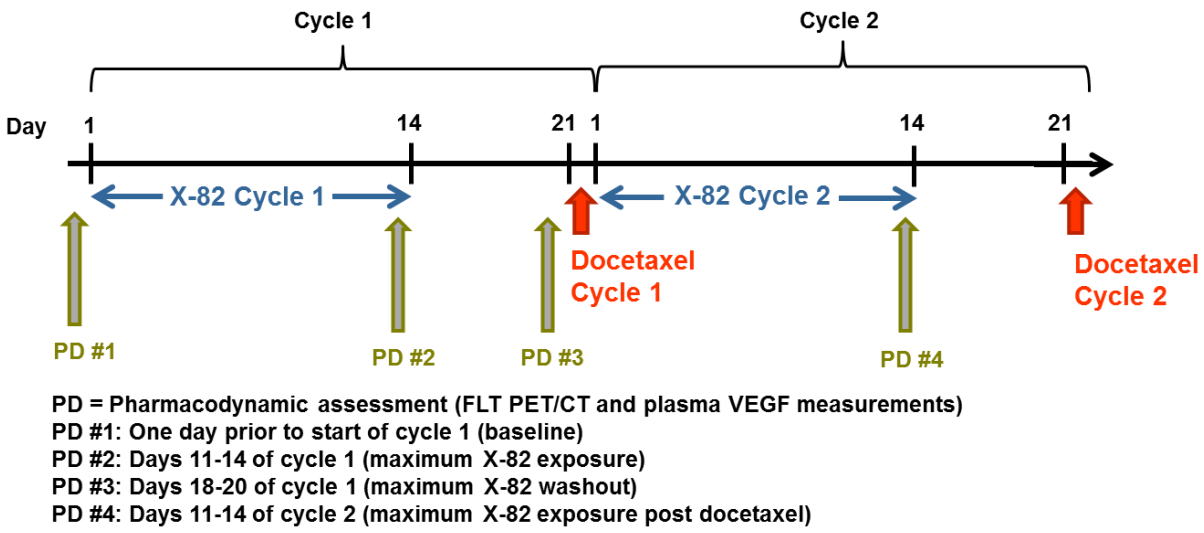

Figure 18: Study schema including drug administration and pharmacodynamic timepoints for the first two treatment cycles.

FLT PET/CT Imaging

FLT PET/CT scans were performed using a Discovery LS PET/CT scanner (GE, Waukesha WI). At the beginning of each imaging session patients were injected with FLT

(mean injected dose 362 MBq, range 314-394 MBq). Sixty minutes post-injection patients underwent a CT scan followed by a whole-body PET scan (5 minutes per scanning position). The CT scan was used for PET attenuation correction and as an anatomic reference for identifying tumors. The PET scans were reconstructed with an iterative 3D ordered subsets expectation maximization algorithm with grid size 256x256, 2 iterations, 14 subsets, and 4 mm post-filter; the PET voxel size was 2.73x2.73x3.27 mm.

Using the resulting PET/CT scans and baseline diagnostic radiology reports, an experienced nuclear medicine physician identified tumors amenable for quantitative FLT PET analysis (i.e. solid tumors outside of regions with high background FLT uptake such as liver and bone marrow). The identified tumors were manually segmented using Amira software (ThermoFisher Scientific Inc., Waltham MA). Tumor cell proliferation was quantified by calculating the max (SUV_{max}), mean (SUV_{mean}), and total (SUV_{total}) SUV of tumor voxels.

Plasma VEGF Measurements

Blood samples were drawn (4 mL) for analysis of VEGF levels by enzyme-linked immunosorbent assay (ELISA). For each sample, plasma was separated by centrifugation at approximately 1200g x 15 minutes, aliquoted into cryovials, and stored at -70^{o}C until analysis. Each sample was analyzed using a commercially available 96-well plate quantitative sandwich immunoassay (Quantikine® human VEGF, R & D Systems, Minneapolis, MN) with a standard curve ranging from 31.2 to 500 pg/mL VEGF. At the time of assay, all samples and standards were brought to room temperature and prepared on the plate as recommended by the manufacturer. The plate was read at 450 nm using a Molecular Devices SpectraMax 190 plate reader.

Statistical Analysis

Changes in tumor SUV metrics were evaluated using a linear mixed effects model with patient specific random effects and a compound symmetry correlation structure to account for multiple tumors within the same patient. A separate model was formulated for estimating the change in FLT uptake between each pair of time points. All SUV measurements were normally transformed before conducting the analyses to ensure the normality assumption was met. Model estimated percentage changes and the corresponding 95% confidence intervals were back transformed and reported on the original scale. All P-values were two-sided and $P<0.05$ was used to define statistical significance. All model fitting was performed in R (v 3.2.00).

Percent changes in plasma VEGF measurements were calculated for each patient and summarized in terms of medians and ranges. Significant changes in VEGF levels across time points were assessed using Wilcoxon signed-rank tests. Significant differences in VEGF levels between the high and low dose X-82 cohorts were assessed using Wilcoxon rank-sum tests.

6.3 Results

Patient Characteristics

Fourteen patients (8 patients in the low dose cohort; 6 patients in the high dose cohort) were enrolled in the study (**Table 12**). The median patient age was 61 years (range 47 to 72) and 64% of patients were female. Patients had a variety of primary cancer histologies with the most common being lung carcinoma (n=3). The median number of RECIST identified tumors (target plus non-target tumors) at baseline was 5 (range 3 to 8). The median number of prior systemic

therapy regimens was 2.5 (range 0-11). Eleven patients (79%) had been treated with prior chemotherapy. Two patients (14%) had been treated with a prior anti-VEGF agent.

Table 12: Patient characteristics

Patient	Age	Gender	Histology	X-82 Cohort	No. of prior systemic therapies	Prior VEGF therapy (Y/N)	Objective response	FLT PET analysis
1	57	Female	Breast carcinoma	Low	6	N	Progressive	Yes
2	47	Female	Thyroid carcinoma	High	1	Y	Stable	Yes
3	72	Female	Ovarian carcinoma	High	6	N	Stable	Yes
4	57	Female	Lung carcinoma	High	4	Y	Partial	Yes
5	64	Female	Urothelial carcinoma	High	2	N	Stable	No
6	71	Male	Squamous cell carcinoma	Low	4	N	N/A	No
7	65	Female	Lung carcinoma	Low	1	N	N/A	No
8	67	Male	Lung carcinoma	Low	2	N	Progessive	No
9	54	Female	Ovarian carcinoma	Low	2	N	Stable	No
10	67	Female	Endometrial carcinoma	High	5	N	N/A	No
11	56	Female	Breast carcinoma	Low	11	N	Stable	No
12	65	Male	Adenoid cystic carcinoma	Low	0	N	Stable	No
13	53	Male	Leiomyosarcoma	Low	3	N	Progressive	No
14	58	Male	Unknown primary carcinoma	High	0	N	Stable	No

Adverse Events

No patients experienced an adverse event greater than grade 3 that were possibly related to X-82. For the six patients in the high dose X-82 cohort, three patients (50%) experienced at least one grade 3 adverse event while on study (**Table 13**). For the eight patients in the low dose X-82 cohort, three patients (38%) experienced at least one grade 3 adverse event while on study. Of the 11 total grade 3 adverse events that were experienced, 7 (64%) occurred in cycle 5 or later. Two patients had docetaxel doses reduced to 60 mg/m^2 after starting treatment due to persistent neutropenia.

Table 13: Adverse events of grade (Gr) 3 or greater that were possibly related to X-82.

Adverse event	Number of pts high dose cohort	Number of pts low dose cohort
Gr 3 Hypertension	1	-
Gr 3 Low WBC	1	-
Gr 3 Infection	1	1
Gr 3 Anemia	1	-
Gr 3 Hyponatremia	1	1
Gr 3 Hypoalbumenia	1	-
Gr 3 Thrombosis	1	-
Gr 3 Rectal Hemorrhage	-	1

Disease Response

For the six patients in the high dose X-82 cohort, the median time on treatment was 13 weeks (range 3 to 19). The objective responses for the high dose cohort were as follows: one patient (17%) with partial response, four patients (67%) with stable disease, and one patient who withdrew consent to participate in the study prior to any follow-up RECIST assessment making them unevaluable for objective response. For the eight patients in the low dose X-82 cohort, the median time on treatment was 8 weeks (range 1 to 36). The objective responses for the low dose cohort were as follows: three patients with stable disease (38%), three patients with progressive disease (38%), and two patients that were unevaluable for objective response.

FLT PET/CT Imaging

Four patients with fourteen metastatic tumors completed all four of the scheduled PET/CT scans and were included in the imaging pharmacodynamic assessment. **Figure 19** shows a tumor with representative changes in SUV. Mixed effects modelling provided estimates of changes in tumor SUVs during therapy (**Table 14**). During the cycle 1 X-82 exposure period (X-82 alone), tumor SUV_{mean} decreased (mean change -2%; P=0.78). During the cycle 1 X-82 washout period, tumor SUV_{mean} significantly increased (mean change +19%; P<0.01). During

the cycle 2 X-82 exposure period (post docetaxel administration), tumor SUV_{mean} significantly decreased (mean change -26%; P=0.02). Percent changes between timepoints for all analyzed tumors are shown in **Figure 20**.

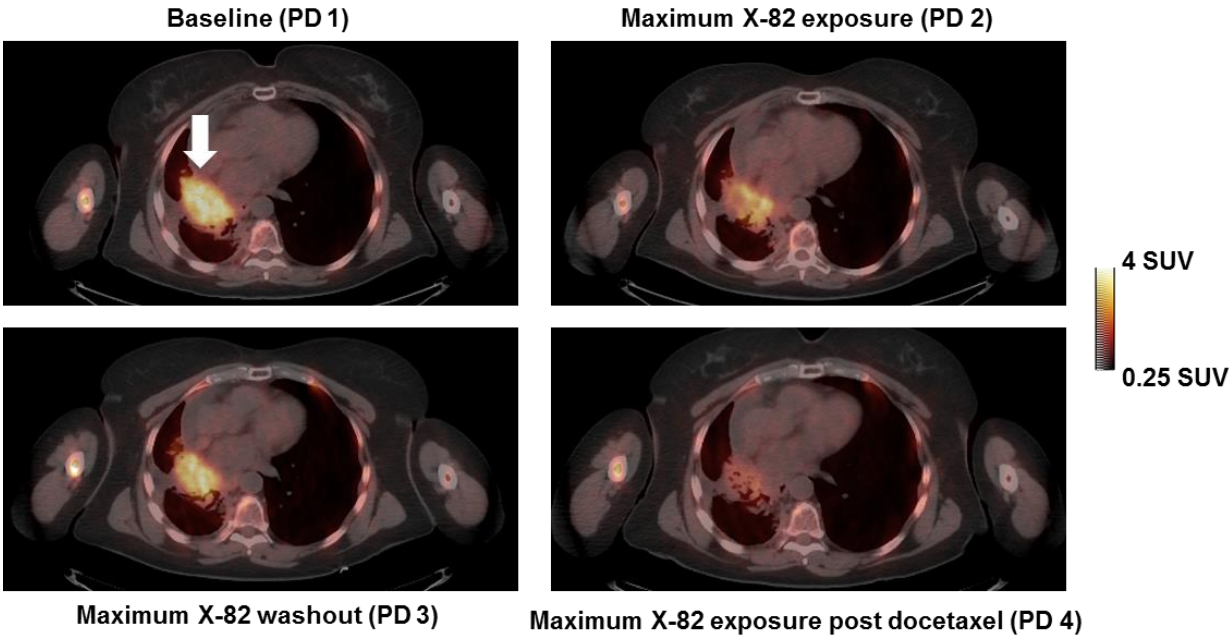

Figure 19: Axial FLT PET/CT slice of a lung tumor (Patient #4). The SUV_{mean} for this tumor (indicated by arrow) was 1.9 g/mL at baseline, decreased to 1.6 g/mL at maximum X-82 exposure in cycle 1, then rebounded to 1.7 g/mL at maximum X-82 washout, and decreased to 1.2 g/mL at maximum X-82 exposure in cycle 2. This patient achieved a partial response as measured by RECIST but eventually progressed after 4 cycles due to development of new brain metastases.

Table 14: Percent changes in tumor SUVs across timepoints calculated using mixed effects models

	SUV metric	Model Estimated Mean Change (%)	95% Confidence Interval	P-Value
Change PD1 to PD2 (n=14)				
	SUV_{mean}	-2	-17 to +15	0.78
	SUV_{max}	-11	-20 to -2	0.04
	SUV_{total}	-16	-33 to +5	0.16
Change PD2 to PD3 (n=14)				
	SUV_{mean}	+19	+10 to +28	<0.01
	SUV_{max}	+29	+20 to +40	<0.01

	SUV_{total}	+71	-9 to +220	0.13
Change PD3 to PD4 (n=14)				
	SUV_{mean}	-26	-40 to -8	0.02
	SUV_{max}	-44	-63 to -14	0.03
	SUV_{total}	-59	-73 to -37	<0.01

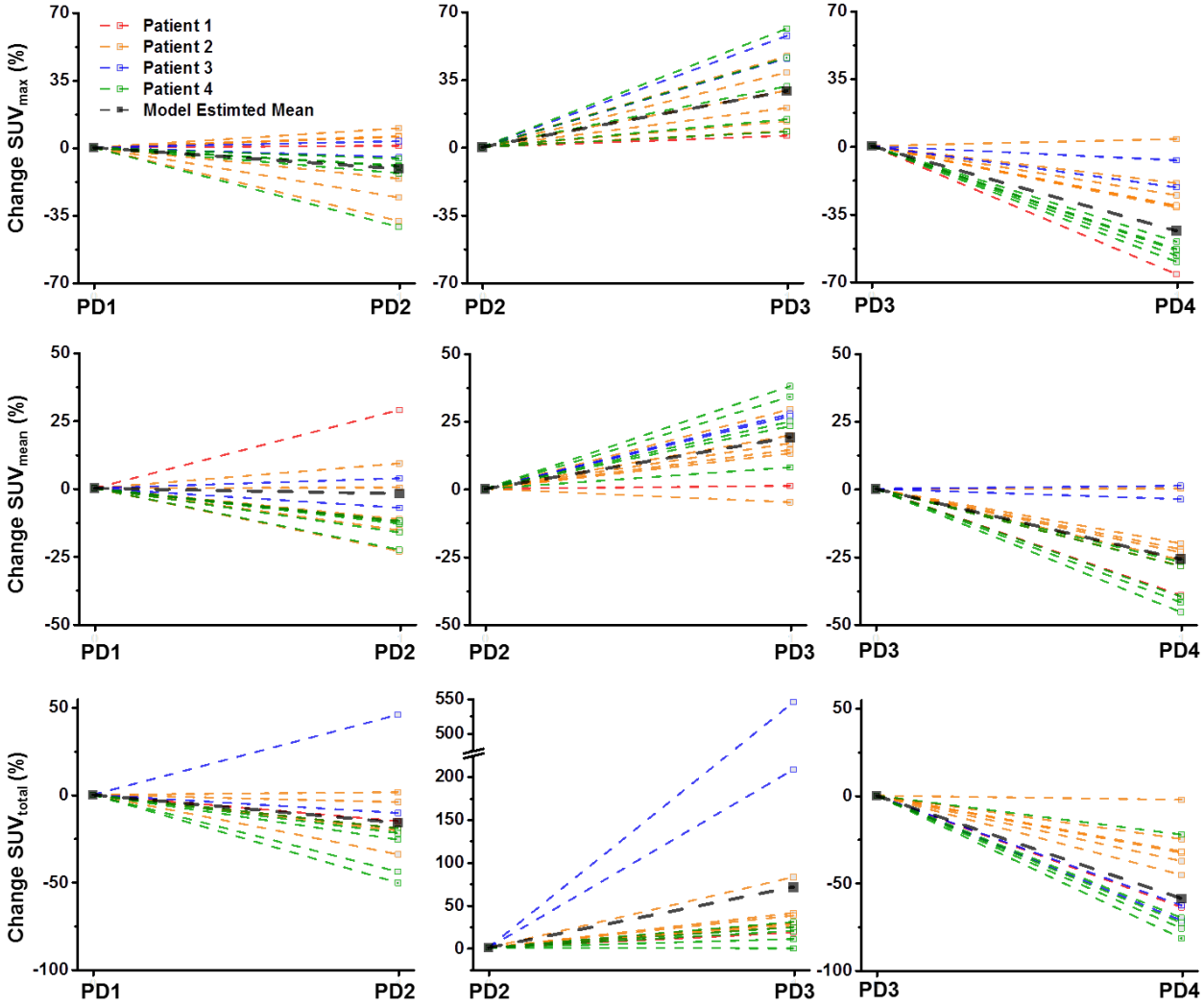

Figure 20: Percent change in tumor SUVs for SUV_{max} (top), SUV_{mean} (middle), and SUV_{total} (bottom). Tumors from the same patient are shown in the same color. Diminished SUV_{max} is evident for the majority of tumors during cycle 1 (change from PD1 to PD2). Increases in SUV_{max} are evident for the majority of tumors during the X-82 treatment break (change from PD2 to PD3). After docetaxel and X-82 exposure in cycle 2 (change from PD3 to PD4), there are decreases in uptake in nearly all tumors. Changes in SUV_{mean} and SUV_{total} had similar trends as SUV_{max}. However, SUV_{mean} was less sensitive to therapy induced changes than SUV_{max}.

SUV_{total} was more sensitive than SUV_{max} to therapy induced changes but the SUV_{total} changes demonstrated greater variability across patients than the SUV_{max} changes.

Plasma VEGF

Ten patients completed two or more plasma VEGF measurements and were included in the VEGF pharmacodynamic analysis (**Table 15** and **Figure 21**). Changes in plasma VEGF were not significantly different between the low and the high dose X-82 cohorts. A combined analysis of both cohorts demonstrated a median increase in plasma VEGF of +13% during the cycle 1 X-82 dosing period (P = 0.57) and a median increase of +52% during the cycle 2 X-82 dosing period (P = 0.03).

Table 15: Median percent changes in plasma VEGF for the low and high dose X-82 cohorts

Change PD1 to PD2	**Low (n=4)**	**High (n=6)**	**Combined (n=10)**
Median (%)	-13	+17	+13
Range (%)	-53 to +37	-55 to +195	-55 to +195
Change PD2 to PD3	**Low (n=4)**	**High (n=5)**	**Combined (n=9)**
Median (%)	-19	-32	-29
Range (%)	-45 to +174	-76 to +137	-76 to +174
Change PD3 to PD4	**Low (n=3)**	**High (n=4)**	**Combined (n=7)**
Median (%)	+62	+48	+52
Range (%)	+27 to +169	-21 to +282	-21 to +282

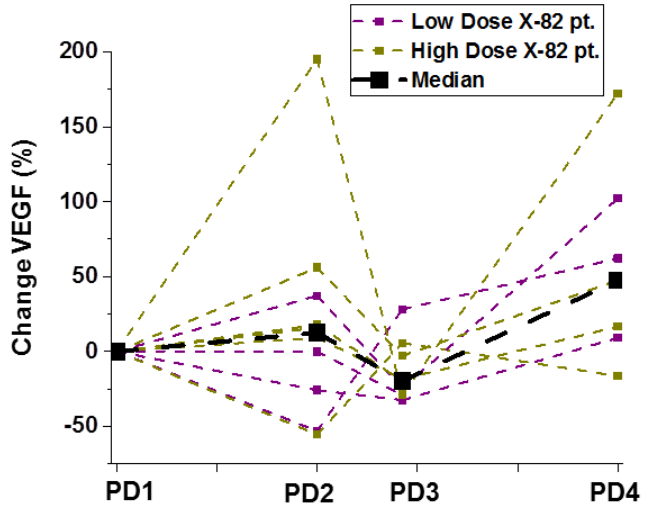

Figure 21: Percent changes in plasma VEGF relative to baseline. Median plasma VEGF levels increased during the cycle 1 (PD1 to PD2) and cycle 2 (PD3 to PD4) X-82 exposure periods; however, there was large amount of interpatient variability, particularly during the cycle 1 X-82 exposure period.

6.4 Discussion

While combination of VEGF ligand targeting agents like bevacizumab with chemotherapy have shown added benefit, combining VEGFR-TKIs with chemotherapies has failed to achieve the same benefit in many studies (5,97-102). Although there have been exceptions, we hypothesized that the mostly negative results of VEGFR-TKIs with chemotherapy studies are due to suboptimal scheduling with a concurrent rather than sequential approach (118). This rationale formed the basis for this study where we investigated the effects of a novel VEGFR-TKI X-82 used in sequential combination with docetaxel applied during VEGFR-TKI treatment breaks. The primary goals of this chapter were to assess the safety/tolerability of treatment and assess pharmacodynamic changes during the sequential treatment regimen. None of the 14 patients in this study experienced an adverse event greater than grade three and 6 (43%) patients experienced a grade 3 adverse event (with the majority of these grade 3 events occurring after 5 cycles of therapy). The sequential combination of X-82 and docetaxel led to diminished tumor FLT uptake, suggestive of a decrease in tumor cell proliferation. Further, a greater decrease in FLT uptake was evident during cycle 2 (X-82 plus docetaxel) than in cycle 1 (X-82 alone), suggesting sequential chemotherapy enhances the pharmacodynamic effect of therapy.

The effect of X-82 at two dose levels (400 mg daily vs. 200 mg daily) was assessed in this study. There were a greater number of patients with stable or partial response on 400 mg X-

82 (5/6 patients; 84%) than those on 200 mg X-82 (3/8 patients; 34%). However, there were a greater number patients that experienced grade 3 adverse events on 400 mg X-82 (3/6 patients; 50%) than on 200 mg X-82 (3/8 patients; 38%).

Increases in FLT PET parameters during the X-82 washout period, indicates a tumor withdrawal flare that is consistent with increased tumor cell proliferation (25,85). After administration of docetaxel and two additional weeks of X-82 exposure, FLT PET parameters decreased again. A greater decrease in FLT PET parameters was evident in the second cycle of treatment suggesting greater decreases in tumor cell proliferation. These results support the hypothesis that 'synchronizing' cell-cycle chemotherapy with VEGFR-TKI treatment breaks will lead to greater anti-tumor effect than VEGR-TKI monotherapy; however, further clinical studies are warranted to confirm long-term clinical benefit. Although we did not assess the effects of docetaxel monotherapy, one prior study has shown that tumor FLT SUV_{max} had median change of -18% two weeks after administration of docetaxel to patients with breast cancer (119). In this study we found even greater decrease in FLT SUV_{max} with mean change of -44% (median -31%) two weeks after administration of docetaxel and continuous VEGFR-TKI therapy, lending further support to the sequential treatment approach. It is important to note that three out of the four patients included in the FLT PET/CT analysis were in the high dose X-82 cohort.

This study was limited in that it accrued only 14 of the targeted 30 patients as the study was prematurely terminated due to a change in developmental strategy of the agent by the sponsor. However, this is one of few clinical studies assessing the effects of sequential chemotherapy applied during VEGFR-TKI treatment breaks. Further, X-82 is a novel VEGFR-TKI that has been studied little in clinical trials and in only one other clinical trial for treating

cancer (120), indicating the potential value of these results for guiding future development of X-82 as well as development of improved therapeutic strategies with VEGFR-TKIs.

6.5 Conclusion

The sequential combination of VEGFR-TKI and chemotherapy was safe and led to diminished FLT uptake. Further, decrease in FLT uptake during cycle 2 (VEGFR-TKI plus chemotherapy) was greater than in cycle 1 (VEGFR-TKI alone), suggesting sequential chemotherapy enhances the pharmacodynamic effect of therapy. These results suggest further study comparing anti-angiogenic therapy with sequential combination of anti-angiogenic therapy and chemotherapy is warranted and in particular determination of whether the sequential treatment approach leads to improved patient outcomes.

Section III FLT PET response assessment in immunotherapy

Immunotherapies have shown great potential for treating metastatic cancers. In metastatic melanoma for example, T cell checkpoint inhibitors were the first therapies to lead to significant increases in overall survival (121-123). T cell checkpoint inhibitors target proteins such as the programmed cell death protein (PD-1) or its ligand PD-L1. PD-1 is a member of a broader class of CD28 proteins that are expressed on the surface of T cells and are involved in regulation of T cell activation and survival. When PD-1 interacts with its ligand PD-L1, deactivation of the T cell occurs, serving as protection from autoimmune destruction of healthy tissue. However, this pathway also provides immunity to infectious diseases and cancer. Specifically in cancer, PD-L1 expressed on the surface of tumor cells can bind to PD-1 receptors on T cells, enabling the tumor to deactivate T cells. These insights led to the development of drugs targeting the PD-L1-PD-1 pathway wherein the goal is to inhibit activation of PD-1, thereby promoting T cell proliferation, survival, and destruction of tumor cells (124).

Despite the promise of T cell checkpoint inhibitors for treating advanced cancers a number of challenges remain. In some cancers, there have not been responses. In metastatic prostate cancer for example, PD-1 blocking antibodies showed no evidence of objective response (125,126). Furthermore, even for cancers that do demonstrate clinical responses to PD-1 blocking antibodies, typically only a small fraction of patients achieve durable, long lasting responses. One theory for the lack of universal responses is that the immune system cannot differentiate tumor cells from healthy cells i.e. the tumor cells express no unique antigens that are recognizable to the immune system as a threat. This had led investigators to explore combinations of T cell checkpoint inhibitors and vaccine-based treatments. In this case, the

vaccine trains the immune system to recognize a specific antigen expressed by tumor cells and the T cell checkpoint blockade prevents the tumor from deactivating the immune response. This multi-faceted approach may prove especially useful in cancers such as prostate that have previously not responded to T cell checkpoint blockade monotherapies (127).

However, there are additional challenges that threaten to hinder clinical translation of these novel immunotherapy combinations. Measuring tumor responses is complicated by the fact that responding tumors may initially increase in size due to infiltration of immune effector cells into the tumor (14). Without having a reliable early marker of response, it is challenging for physicians to manage patient care and decide whether a given treatment should be continued or swapped with something more appropriate. Furthermore, knowledge of why a given patient does not respond to a particular immunotherapy is often unknown. Another important challenge of combining multiple immunotherapies is the increased risk of patients experiencing an immune related adverse event. As monotherapies, T cell checkpoint inhibitors have well documented risks relating to adverse events, however, these risks become even greater when combining multiple immunotherapies (128,129). This generates a need for pharmacodynamic and predictive biomarkers in immunotherapy (130,131).

This dissertation will investigate the potential clinical value of FLT PET/CT imaging as a biomarker in immunotherapy. Specifically we will investigate whether FLT PET detects changes in immune cell and tumor cell proliferation during novel combination of a PD-1 inhibitor and prostate cancer vaccine (Chapter 7: Evaluating patient responses to immunotherapy using FLT PET). We will also perform a preliminary assessment of combined FLT and FDG PET-based biomarkers for assessing an immune response (Chapter 8: Multi-modality FLT and FDG PET for imaging immune response in canine patients).

Chapter 7: Evaluating patient responses to immunotherapy using FLT PET

7.1 Motivation

A large number of patients do not respond to immunotherapy, many respond without immediate changes detectable with conventional imaging, and many have unusual immune-related adverse events that cannot be predicted in advance. This has been the motivation for a number of clinical studies aiming to identify improved biomarkers for evaluating patient responses to immunotherapy. Two of these studies utilized FLT PET in clinical trials to evaluate its feasibility as a biomarker of response in immunotherapy. In 2010 Ribas et al., performed baseline and follow-up FLT PET scans on 10 patients with advanced melanoma who were treated with cytotoxic T lymphocyte-associated antigen 4 (CTLA4) blockade (132). No significant change in FLT uptake was observed in tumors after approximately two months of treatment, but a significant increase in FLT uptake was noted in spleen. The authors hypothesized this increase in uptake was due to proliferation of splenic T-cells in response to CTLA4 blockade. In the other clinical study, 11 patients with melanoma lymph node metastases were treated with dendritic cell vaccine therapy injected intranodally. These patients underwent multiple FLT PET scans at baseline and follow up (133). A significant increase in FLT uptake was evident in vaccinated lymph nodes, and this increase persisted for up to three weeks following vaccination. Furthermore, a significant correlation was found between FLT uptake in vaccinated lymph nodes and T and B cell responses derived from peripheral blood samples taken at the time of imaging. These studies provide evidence suggesting FLT PET may be useful for assessing pharmacodynamics effects of immunotherapies.

In this chapter, we further investigate how FLT PET measurements of tumor and immune cell proliferation might be utilized to overcome the clinical challenges facing immunotherapy. Changes in FLT PET uptake will be assessed in metastatic castrate resistant prostate cancer patients undergoing treatment with pTVG-HP DNA vaccine and PD-1 checkpoint inhibitor pembrolizumab. The results of this work demonstrate the utility of FLT PET for predicting tumor responses and immune-related adverse events during immunotherapy.

7.2 Methodology

Study Design

This chapter reports on the exploratory aim of a clinical trial whose primary endpoints were to assess the safety and clinical effects of pTVG-HP DNA Vaccine and PD-1 inhibitor Pembrolizumab in patients with metastatic prostate cancer (127). Patients underwent treatment in one of three study arms (**Figure 22**). In study Arm 1 pTVG-HP vaccine was given every 2 weeks from week 0 to week 10 and pembrolizumab was given every 3 weeks from week 0 to week 9. In study Arm 2 pTVG-HP vaccine was given every 2 weeks from week 0 to week 10 and pembrolizumab was given every 3 weeks from week 12 to week 21. In study Arm 3 both the pembrolizumab and pTVG-HP vaccine were given every 3 weeks from week 0 to week 21. The vaccine was administered intradermally (100 μg) in the left deltoid region and pembrolizumab was administered intravenously (2 mg/kg). All patients also received recombinant human granulocyte-macrophage colony-stimulating factor (GM-CSF) at time of vaccine administration (208 μg). Both a baseline and follow-up FLT PET/CT scan was acquired in all treatment arms. The baseline FLT PET/CT scan was performed prior to starting treatment (within 4 weeks) and the 12 week FLT PET/CT scan was performed at the start of week 12 (± 3 days).

Patients' serum PSA was measured every 6 weeks. All subjects were followed for at least one year, with staging CT scans of the abdomen and pelvis, and bone scintigraphy, performed every 12 weeks or as clinically indicated using Prostate Cancer Clinical Trials Working Group recommendations (134). Patients came off study at the time of radiographic progression, undue toxicity, or at the discretion of the treating physician for clinical deterioration. The study protocol was reviewed and approved by all local (University of Wisconsin Human Subjects' Review Board), and federal (FDA, NIH Recombinant DNA Advisory Committee) entities. All patients gave written informed consent for participation.

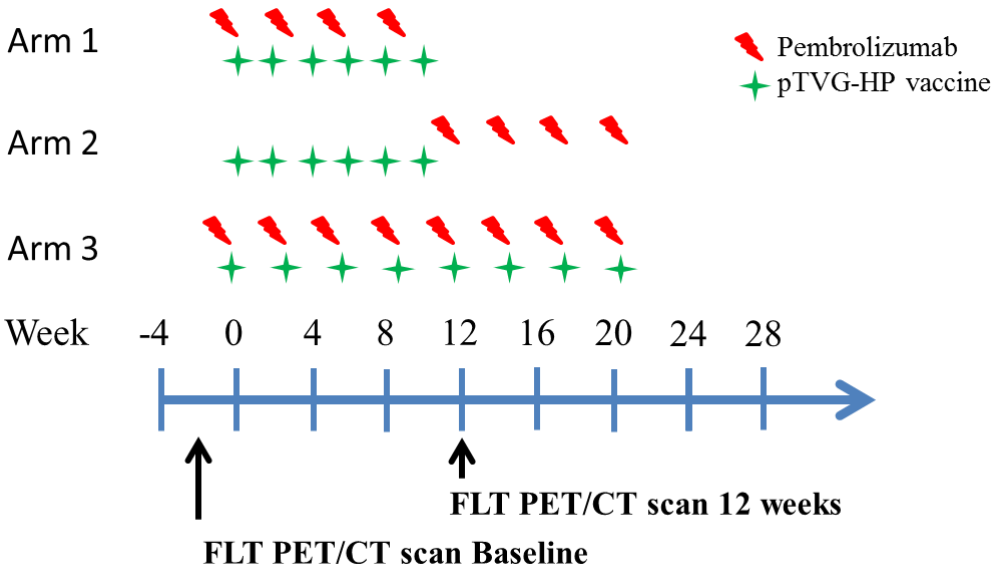

Figure 22: Study Schedule

PET/CT image acquisition and segmentation

All patients were scanned on a Discovery 710 PET/CT scanner (GE, Waukesha WI). The CT scan was used for PET attenuation correction and anatomic localization of regions of interest. A median of 345 MBq of FLT was injected (range = 210 to 363 MBq) and PET scans were

started median 59.8 minutes post-injection (range = 59.2 to 60.7 minutes post-injection). Each PET scan was a whole body scan with 5 min per bed position (patients were scanned from thighs to eyes) and 700 mm axial field of view. The PET reconstruction was a 3D ordered subsets expectation maximization algorithm with parameters that included an axial grid size of 192x192 voxels (3.64x3.64 mm axial voxel size), 3.27 mm slice thickness, 3 iterations, 24 subsets, and 5 mm Gaussian post filter.

To evaluate changes in immune cell proliferation, the left and right axillary lymph nodes were identified by a nuclear medicine physician and manually segmented using the PET and CT images. The femoral bone marrow and spleen of each patient were also segmented using semi-automatic methods that utilized both the CT and PET images. Bone marrow and spleen segmentations were visually checked to ensure no metastatic disease was present within the segmentations. Tissues that were related to immune-related adverse events (pancreas and thyroid) were also manually segmented to quantify FLT uptake in these tissues.

To evaluate tumor responses, soft tissue metastases were identified by a nuclear medicine physician and manually segmented using the FLT PET/CT images. The average and maximum PET uptake was extracted from all segmentations (SUV_{mean} and SUV_{max}, respectively). To assess tumor burden, the total tumor uptake (SUV_{total}) was also extracted from tumor segmentations.

Statistical Analysis

Due to the skewed nature of PET SUV distributions, non-parametric statistics were used to analyze the data. Wilcoxon signed-rank tests were used to assess whether there were significant changes in PET uptake from baseline to 12 weeks. Correlations were assessed using

Spearman Correlations. Wilcoxon rank-sum tests were utilized to assess differences is SUV distributions between independent groups. Cox-proportional hazards regression models were used to investigate the relationship between changes in PET uptake and progression free survival. Patients who came off study for any reason other than radiographic progression were censored. The concordance index was used to assess the ability of PET metrics to predict progression free survival and the hazard ratio was used to assess correlations between PET metrics and progression free survival (135,136). Receiver operating characteristic (ROC) curves were used to assess the ability of FLT PET to predict adverse events (137). All statistical analysis was done using R (v3.4.0). P-values less than P=0.05 were considered statistically significant.

7.3 Results

Changes in FLT PET Uptake in Immune Organs and Soft-Tissue Metastases

Seventeen patients completed both the baseline and 12 week FLT PET/CT scans (**Table 16**). The number of patients in study arms 1, 2, and 3 were 6/17 (35%), 6/17 (35%), and 5/17 (30%), respectively. The median progression free survival time was 24 weeks (range 12 to greater than 72 weeks). No significant differences in progression free survival time were found across the three study arms. For all segmented regions, the changes in SUV_{mean} and SUV_{max} were strongly correlated ($\rho > 0.70$, $P < 0.05$). Thus, the following results focus on describing changes in SUV_{mean} (the results for SUV_{max} were similar).

The change in SUV_{mean} of vaccine draining left axillary (sentinel) lymph nodes was significantly greater than the change in contralateral right axillary lymph nodes (median +16%, P = 0.02) (**Figure 23**a-b). Changes in SUV_{mean} of left axillary lymph nodes were strongly

correlated with changes in right axillary lymph nodes ($\rho = 0.84$, $P < 0.01$). No significant differences in lymph node SUVs were evident across the study arms.

Changes in spleen and bone marrow SUV_{mean} were moderately correlated ($\rho = 0.53$, $P = 0.04$). The bone marrow had a median increase of 1% in SUV_{mean} (range -20% to +49%, $P = 0.23$). The spleen demonstrated a significant median increase of 8% in SUV_{mean} (range -16% to +46%, $P = 0.02$). Furthermore, patients in arm 3 had significantly greater increases in spleen SUV_{mean} relative to arm 1 ($P = 0.04$) and arm 2 ($P < 0.01$) (**Figure 23**c-d). Neither changes in bone marrow or spleen SUV were significantly correlated with changes in lymph node SUV.

The median tumor SUV_{mean} increased 10% (range -45% to +29%, $P = 1.0$) (**Figure 23**e-f). Changes in tumor SUV_{mean} were not significantly correlated with changes in lymph node, bone marrow, or spleen SUVs. No significant differences in the changes in tumor SUV_{mean} were evident across the study arms.

The median thyroid SUV_{mean} increased 12% (range -16% to +202%, P=0.03) (**Figure 23**g-h). No significant differences in the changes in thyroid SUV_{mean} were evident across the study arms. Changes in thyroid SUVs were not significantly correlated with changes in lymph node, bone marrow, spleen, or tumor SUVs.

Table 16: Patient information

Patient #	Study arm	Soft tissue mets. at baseline	Bone mets. at baseline	IRAE greater than Gr 1[a] (week of occurrence)	Progression free survival (weeks)
1	1	Yes	Yes	None	24
2	1	Yes	Yes	None	48
3	1	No	Yes	None	24
4	1	Yes	No	None	48+
5	1	Yes	Yes	None	16
6	1	No	Yes	Hyperthyroidism (6), Hypothyroidism (12)	24
7	2	No	Yes	Hypothyroidism (36)	36+
8	2	Yes	Yes	Pancreatitis (30)	48
9	2	Yes	Yes	None	24
10	2	Yes	Yes	None	24+
11	2	No	Yes	Hyperthyroidism (18)	48
12	2	No	Yes	Adrenal Insufficiency (38)	72+
13	3	Yes	Yes	Elevated TSH (9)	36+
14	3	Yes	No	None	24
15	3	Yes	Yes	None	24
16	3	Yes	No	Hyperthyroidism (3)	12
17	3	No	Yes	None	12

[a] Immune-related adverse events that were at least possibly related to pembrolizumab or pTVG vaccine are listed

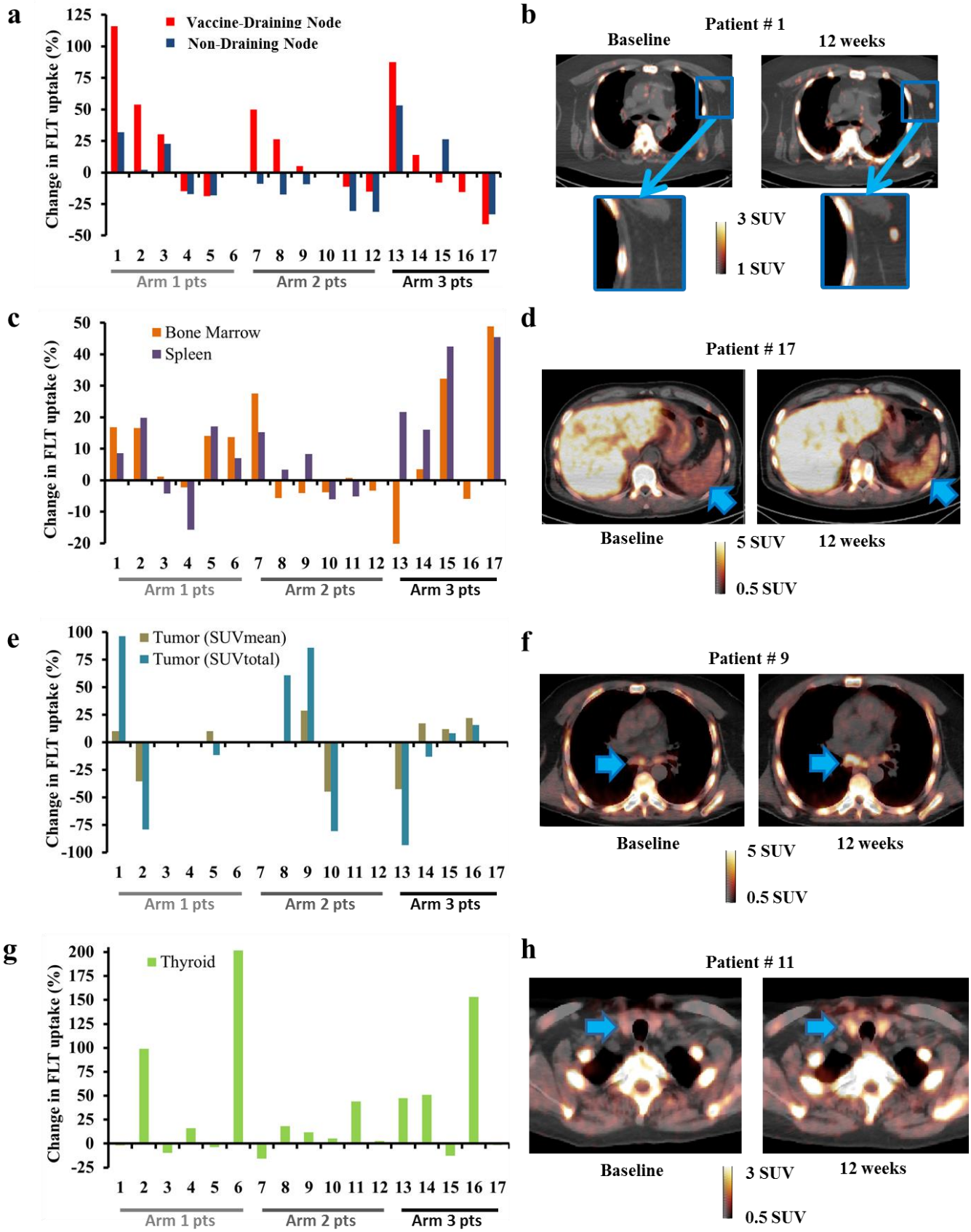
a
Vaccine-Draining Node
Non-Draining Node
Change in FLT uptake (%)
125
100
75
50
25
0
-25
-50
1 2 3 4 5 6 7 8 9 10 11 12 13 14 15 16 17
Arm 1 pts
Arm 2 pts
Arm 3 pts
b
Patient # 1
Baseline
12 weeks
3 SUV
1 SUV
c
Bone Marrow
Spleen
Change in FLT uptake (%)
50
40
30
20
10
0
-10
-20
1 2 3 4 5 6 7 8 9 10 11 12 13 14 15 16 17
Arm 1 pts
Arm 2 pts
Arm 3 pts
d
Patient # 17
Baseline
5 SUV
0.5 SUV
12 weeks
e
Tumor (SUVmean)
Tumor (SUVtotal)
Change in FLT uptake (%)
100
75
50
25
0
-25
-50
-75
-100
1 2 3 4 5 6 7 8 9 10 11 12 13 14 15 16 17
Arm 1 pts
Arm 2 pts
Arm 3 pts
f
Patient # 9
Baseline
5 SUV
0.5 SUV
12 weeks
g
Thyroid
Change in FLT uptake (%)
200
175
150
125
100
75
50
25
0
-25
1 2 3 4 5 6 7 8 9 10 11 12 13 14 15 16 17
Arm 1 pts
Arm 2 pts
Arm 3 pts
h
Patient # 11
Baseline
3 SUV
0.5 SUV
12 weeks

Figure 23: Patients are numbered the same in all inserts (also the same as in Table 1) and are ordered by study arm. (a) Changes in FLT SUV_{mean} in vaccine draining left axillary lymph nodes are shown for each patient along with changes in non-draining right axillary lymph nodes. A number of outliers with changes in left axillary lymph node SUV greater than 50% are evident. (b) Axial FLT PET/CT slice of the thorax of patient #1. The insert highlights a vaccine draining left axillary lymph with elevated uptake after 12 weeks of therapy (c) Changes in FLT SUV_{mean} in bone marrow and spleen. (d) Axial FLT PET/CT slice of the upper abdomen of patient #17. The arrow indicates the patient's spleen that has noticeably increased FLT uptake after 12 weeks. (e) Changes in FLT uptake in patients with soft tissue metastases are shown for SUV_{mean} and SUV_{total}. Changes in tumor SUVmean and tumor SUVtotal were significantly correlated ($\rho = 0.66$, $P = 0.04$). (f) Axial FLT PET/CT slice of the thorax of patient #9. The arrow indicates metastatic mediastinal lymph nodes with visually increased FLT uptake after 12 weeks of therapy. Following RECIST this patient had radiographically stable disease at week 12 but had subsequent disease progression upon the next radiographic follow-up at 24 weeks. (g) Changes in thyroid FLT uptake (h) Axial PET/CT slices are shown for a patient that experienced grade 2 hyperthyroidism (patient #11). The arrow indicates the position of the right thyroid lobe where visually increased FLT uptake is evident at 12 weeks. Notably, this patient had their first pembrolizumab injection 1 day prior to their 12 week PET scan.

FLT PET and Tumor Responses to Immunotherapy

When looking across all evaluable patients, changes in FLT uptake after 12 weeks were positively correlated with changes in RECIST measurements (**Figure 24**a-b) and PSA measurements (**Figure 24**c-d). Changes from baseline to 12 weeks in patient PSA, tumor size measurements, and PET SUVs were included in univariate Cox proportional hazards regression models to assess their association with progression free survival (**Table 17**). The strongest association was found for changes in tumor SUV_{mean} (Concordance index = 0.83, $P<0.01$; Hazard Ratio = 3.38, $P = 0.05$). A greater increase in tumor SUV_{mean} during therapy was predictive of shorter progression free survival. Furthermore, the change in SUV_{mean} from baseline to 12 weeks differentiated patients with progression free survival less than or equal to the median time from those patients with progression free survival greater than the median time (**Figure 25**a). For comparison, **Figure 25**b shows that greater increases in PSA were also associated with shorter progression free survival, albeit the association was not as significant. Notably, a greater increase in spleen SUV_{mean} was also significantly predictive of shorter

progression free survival (Concordance index = 0.73, P = 0.01; Hazard Ratio = 2.14, P = 0.02). At baseline, only tumor SUV_{mean} and tumor SUV_{total} were significantly predictive of progression free survival (**Table 18**).

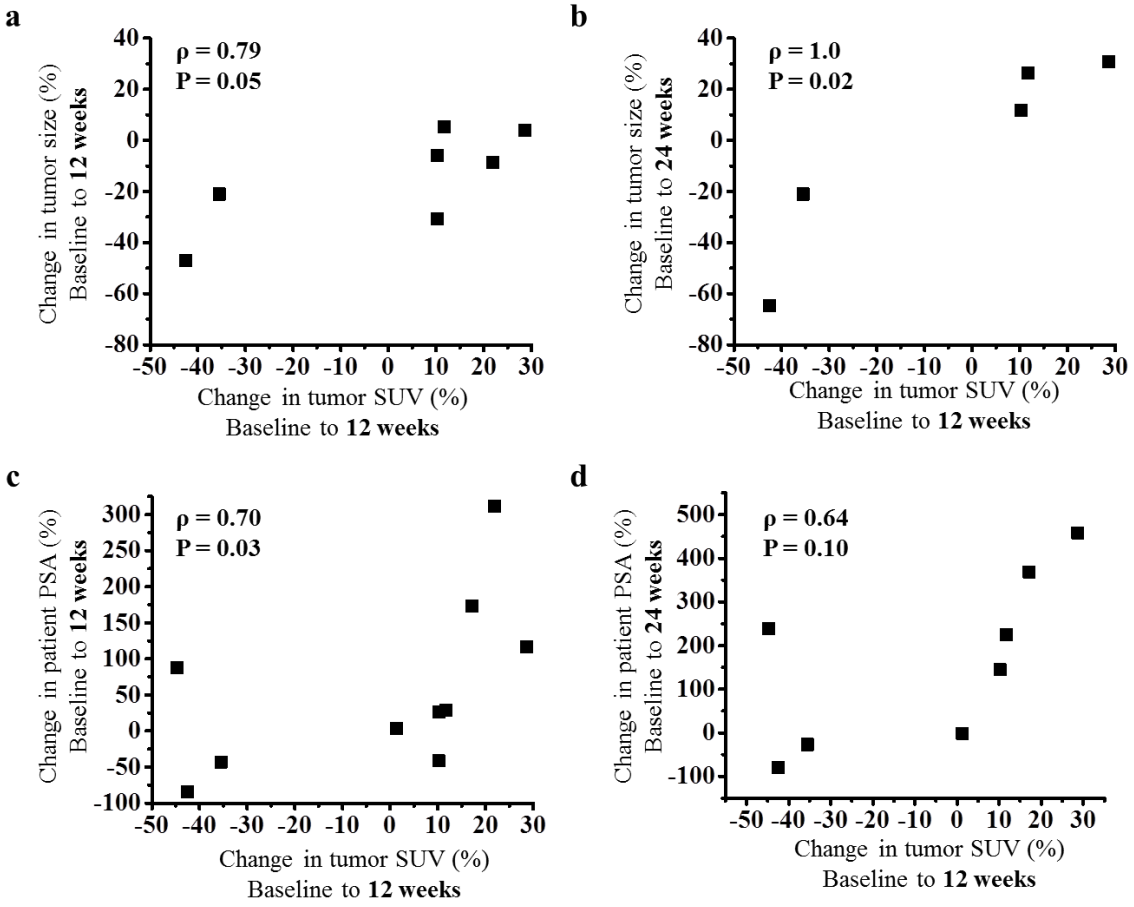

Figure 24: (a) Changes in tumor FLT SUV_{mean} after 12 weeks are plotted against changes in tumor size after *12 weeks*. Tumor size was measured following RECIST guidelines using a diagnostic CT scan. (b) Changes in tumor FLT SUV_{mean} after 12 weeks are plotted against changes in tumor size after *24 weeks*. (c) Changes in tumor FLT SUV_{mean} after 12 weeks are plotted against changes in PSA after *12 weeks*. (d) Changes in tumor FLT SUV_{mean} after *12 weeks* are plotted against changes in PSA after *24 weeks*. The strong correlation between the changes in PET uptake at 12 weeks and changes in tumor size at 24 weeks, indicate FLT PET may offer a relatively early marker of response in patients with soft tissue tumors. Note some patients are not included in these figures because they did not have RECIST measurable soft tissue tumors or were on study for less than 24 weeks.

Table 17: Changes in FLT SUVs, RECIST size measurements, and PSA levels from baseline to 12 weeks were included in Cox proportional hazards regression models to assess association with progression free survival time. Rows are organized from highest to lowest concordance index values.

Organ/Tissue	C-index[a]	C-index P value	HR[b]	HR P value	N[c]
Change tumor SUV_{mean}	0.83 (0.71 to 0.95)	<0.01	3.38 (1.01 to 11.28)	0.05	10 (8)
Change spleen SUV_{mean}	0.73 (0.56 to 0.90)	0.01	2.14 (1.11 to 4.12)	0.02	16 (11)
Change PSA	0.72 (0.50 to 0.94)	0.05	2.34 (1.18 to 4.62)	0.01	17 (12)
Change left axillary lymph node SUV_{mean}	0.70 (0.48 to 0.91)	0.07	0.89 (0.43 to 1.84)	0.75	16 (11)
Change tumor SUV_{total}	0.69 (0.59 to 0.79)	<0.01	1.53 (0.76 to 3.10)	0.24	10 (8)
Change bone marrow SUV_{mean}	0.65 (0.41 to 0.89)	0.22	1.94 (0.98 to 3.86)	0.06	17 (12)
Change soft tissue tumor size RECIST	0.59 (0.54 to 0.63)	<0.01	1.78 (0.60 to 5.29)	0.30	7 (6)

[a] C-index = concordance index (95% confidence interval shown in parenthesis)
[b] HR = hazard ratio (95% confidence interval shown in parenthesis)
[c] N = number of patients included in calculation (value in parenthesis is number of patients that were not censored)

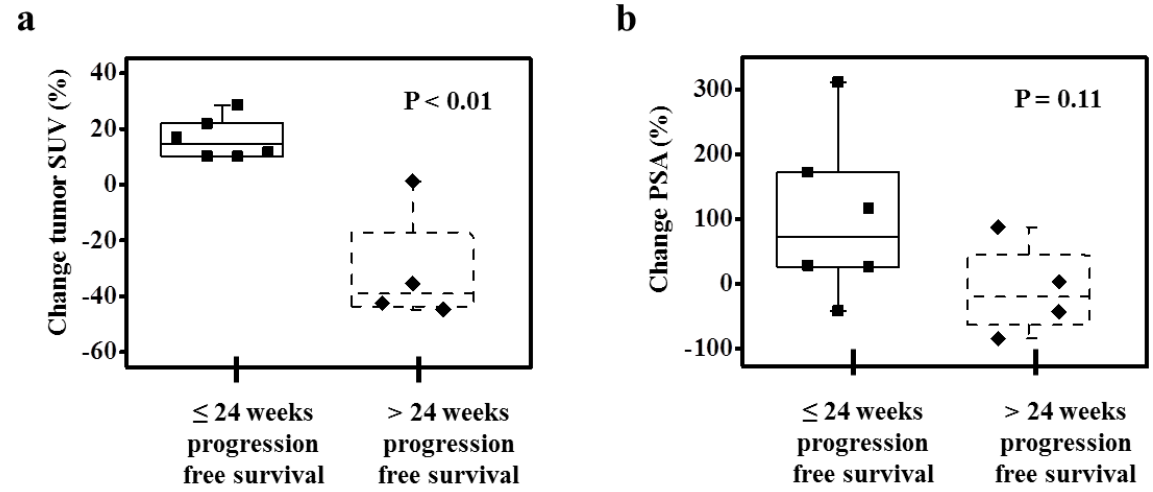

Figure 25: (a) Change in tumor SUV_{mean} at 12 weeks differentiated patients who had progression free survival less than or equal to the median progression free survival time (24 weeks) from patients who had progression free survival greater than the median. (b) Changes in PSA levels after 12 weeks for the same set of patients as shown in insert (a).

Table 18: Baseline FLT SUVs, tumor size measurements, and PSA levels were included in Cox proportional hazards regression models to assess association with progression free survival time. Rows are organized from highest to lowest concordance index values

Organ/Tissue	C-index[a]	C-index P value	HR[b]	HR P value	N[c]
Tumor SUV_{mean}	0.76 (0.64 to 0.88)	<0.01	0.34 (0.11 to 1.10)	0.07	10 (8)
Tumor SUV_{total}	0.62 (0.50 to 0.74)	0.04	1.61 (0.71 to 3.64)	0.25	10 (8)
Bone marrow SUV_{mean}	0.58 (0.45 to 0.72)	0.24	1.07 (0.68 to 1.68)	0.78	17 (12)
Spleen SUV_{mean}	0.58 (0.39 to 0.77)	0.40	0.83 (0.45 to 1.54)	0.57	16 (11)
Left axillary lymph node SUV_{mean}	0.54 (0.43 to 0.76)	0.69	0.71 (0.38 to 1.31)	0.27	16 (11)
Soft tissue tumor size (RECIST)	0.53 (0.30 to 0.76)	0.78	0.96 (0.51 to 1.78)	0.89	7 (6)

PSA	0.50 (0.29 to 0.71)	1.0	0.74 (0.36 to 1.52)	0.42	17 (12)

[a] C-index = concordance index (95% confidence interval shown in parenthesis)
[b] HR = hazard ratio (95% confidence interval shown in parenthesis)
[c] N = number of patients included in calculation (value in parenthesis is number of patients that were not censored)

Only patient #5 had successful baseline and 12 week soft-tissue tumor biopsies that could be compared with FLT PET (**Figure 26**). At 12 weeks, this patient's PSA had decreased 42%, their sum of CT defined tumor diameters had decreased 30% (RECIST measurement), and tumor FLT PET uptake had increased 10% (SUV_{mean}) (**Figure 26**a). Immunofluorescence staining of this patient's biopsy tissue revealed the majority of proliferating cells were prostate cancer cells at both baseline and follow-up (**Figure 26**b). Quantification of the immunofluorescence images revealed a non-significant increase in the number of proliferating (Ki67+) cells per unit area from baseline to 12 weeks that is in agreement with the slight increase in FLT PET uptake during this same time period (**Figure 26**c). Notably by week 16, this patient's PSA had increased 26% and RECIST measurements had increased 31%, leading to classification of progressive disease.

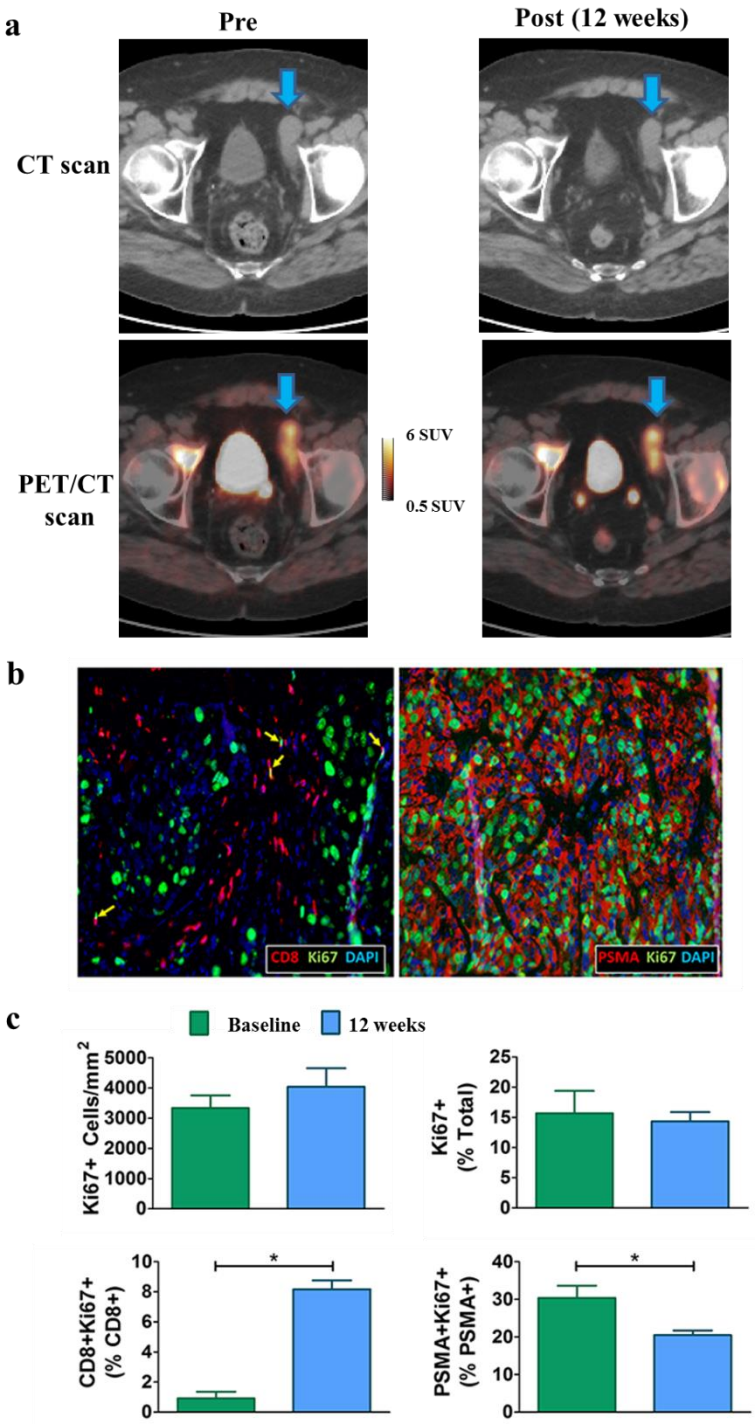

Figure 26: (a) Axial CT and PET/CT slices with a metastatic tumor indicated. At week 12 this patient had experienced diminished PSA and tumor size but slightly increased tumor FLT uptake. By week 16, this patient was found to have progressive disease with marked increases in tumor size and PSA. (b) Immunofluorescence images show representative histology sections taken from the week 12 biopsy of the tumor indicated in part (a). The left immunofluorescence image shows proliferating T cells (Ki67+CD8+; yellow arrows) and the right image shows proliferating tumor cells (Ki67+PSMA+). (c) Quantification of the immunofluorescence images from the tumor indicated in part (a). The top row shows changes in the number of proliferating cells per unit area (left) and changes in the percentage of proliferating cells (right). The bottom row shows percent changes in proliferating CD8+ T cells (left) and proliferating PSMA+ tumor cells (right). Immunofluorescence images and analysis are courtesy of Christopher Zahm. *P-value is less than 0.05

FLT PET and Immune-Related Adverse Events

Five out of seventeen patients (29%) experienced a grade 2 or greater adverse event relating to thyroid function (median time to adverse event was 9 weeks). Three out of the five patients that experienced a thyroid-related adverse event had the adverse event occur prior to the second FLT PET scan at 12 weeks, indicating the second PET scan may not be as useful for making predictions (**Figure 27**a). However, baseline FLT uptake in the thyroid was significantly predictive of whether or not a patient would go on to experience a thyroid-related adverse event (AUC = 0.97 $P<0.01$) (**Figure 27**b).

One out of seventeen patients (6%) had grade 2 or greater pancreatitis. This patient experienced a 30% increase in pancreas FLT SUV_{mean} from baseline to 12 weeks. However, other patients experienced even greater increases in pancreas FLT uptake and did not go on to experience pancreatitis. Baseline pancreatic FLT uptake was not significantly different in the patient that experienced pancreatitis than in the patients that did not experience pancreatitis. One patient experienced grade 3 adrenal insufficiency 38 weeks after starting treatment; however, there was no evidence of this on the baseline or 12 week FLT PET scans. No association was evident between immune-related adverse events and progression free survival.

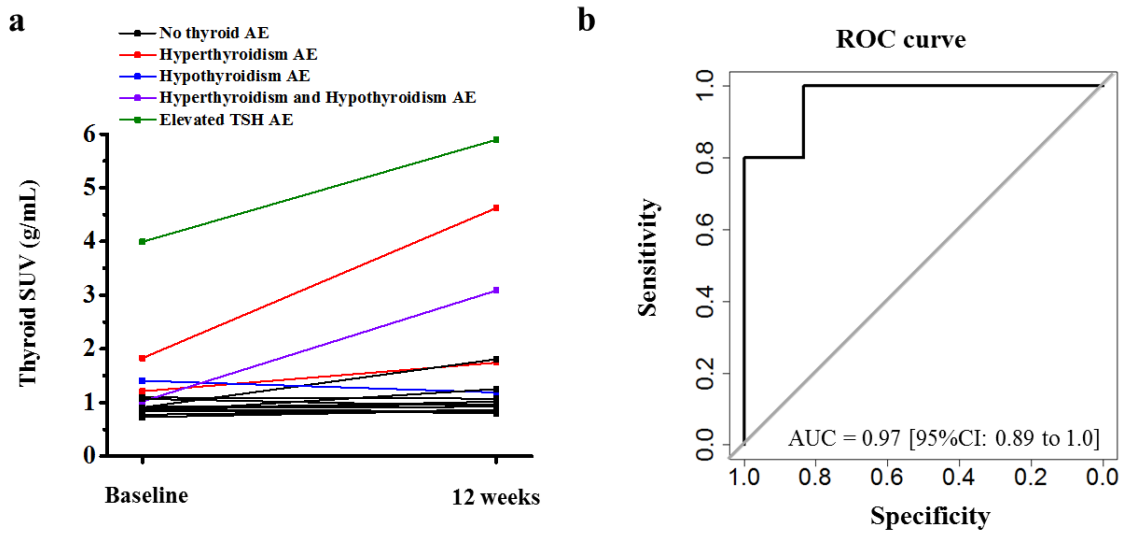

Figure 27: (a) Thyroid SUV_{mean} at baseline and after three months for all patients. Patients that experienced a thyroid related-adverse event of grade 2 or greater are shown in various colors to distinguish them from patients that did not experience a thyroid-related adverse event (black). (b) ROC curve showing the value of thyroid SUV_{mean} at baseline for predicting which patients will go on to experience a thyroid-related adverse event.

7.4 Discussion

In this chapter we evaluated changes in various lymphoid organs including non-metastatic lymph nodes, spleen, and bone marrow. This rationale was based on prior studies that showed increased FLT uptake in lymphoid organs following immunotherapy (132,133). Specifically relating to lymph nodes, previous work by Aarntzen et al. showed increased FLT uptake in lymph nodes after a dendritic cell vaccine was injected intranodally in patients with melanoma (133). Thus in the current chapter, we hypothesized that similar increases in FLT uptake would be evident in vaccine-draining lymph nodes following intradermal injection of pTVG-HP vaccine. Significantly increased FLT uptake was found in left axillary lymph nodes (sentinel node) when compared with right axillary lymph nodes. This suggests that at least a subset of patients experience a regional immune response to pTVG-HP vaccine that is

characterized by increased cell proliferation in vaccine draining lymph nodes after 12 weeks of therapy.

Previous work by Ribas et al. showed significantly increased spleen uptake of FLT following treatment with tremelimumab in patients with metastatic melanoma (132). The authors of that study hypothesized that releasing the CTLA4 checkpoint on cell cycle in lymphocytes resulted in increased cell proliferation in the spleen. Similarly in this study, significant increases in spleen uptake of FLT were evident. These increases were greatest in arm 3, where patients received a combination of pTVG-HP vaccine and pembrolizumab every three weeks. Interestingly, these increases in splenic FLT uptake were inversely correlated with progression free survival time i.e. patients with greater increases in splenic FLT uptake were more likely to have shorter progression free survival. Further investigation of this phenomenon may be critical to understanding why some patients do not respond to therapy.

Measurements of tumor size derived from anatomic imaging modalities (e.g. computed tomography, magnetic resonance imaging, etc.) have proven essential in oncology, particularly for assessing tumor responses to cytotoxic therapy (13). However, these modalities are less useful in the context of immunotherapy where inflammation in responding patients can confound measurements of tumor progression (14). We hypothesized that changes in cell proliferation as measured via FLT PET will be more specific for identifying non-responding patients than other imaging modalities. This is supported by the results of this study, where changes in FLT PET after 12 weeks were more predictive of time to progression (based on concordance index values) than changes in tumor size measured via CT after 12 weeks or changes in PSA after 12 weeks. This suggests FLT PET measurements may offer earlier markers of response than traditional methods of clinical assessment.

In this study 5/17 (29%) patients experienced an adverse event of grade 2 or greater related to thyroid function. One case led to discontinuation of treatment that was followed by subsequent disease progression. We discovered significantly higher FLT uptake at baseline in thyroids of patients that went on to experience a thyroid-related adverse event during treatment. These results indicate that prior to therapy, there is elevated cell proliferation in thyroids of patients who are likely to experience thyroid related adverse events. A previous study suggested PD-1 blockade may cause latent thyroid auto-immunity to become clinically detectable and lead to subsequent thyroid-related adverse events (138). Further study might elucidate whether elevated FLT uptake in thyroid tissue at baseline is providing a measure of proliferating T cells that is linked with latent thyroid auto-immunity. In this study, monitoring of thyroid-related adverse events was done by measuring serum changes in thyroid function. The results of this work suggest FLT PET imaging might also have a role in monitoring/predicting adverse events related to thyroid function.

Thyroid-related adverse events have been documented during pembrolizumab treatment but not during pTVG-HP vaccinations, making it likely that the thyroid-related adverse events in this study were caused by the pembrolizumab (128,129). This is supported by the fact that no patients in this study experienced a thyroid adverse event before having a pembrolizumab injection. Interestingly, one patient had increased thyroid FLT uptake less than 24 hours after receiving their first pembrolizumab injection (**Figure 23**h). This suggests that the auto-immune effects mediated by pembrolizumab may be detectable using FLT PET as early as 1 day following pembrolizumab injection.

In this study 1/17 (6%) patients experienced a grade 2 or greater pancreatitis. This patient had increased pancreatic FLT uptake from baseline to 12 weeks; however, greater

increases in pancreatic FLT uptake were evident in patients that did not go on to experience pancreatitis. This indicates FLT PET has limited specificity for predicting the occurrence of pancreatitis.

It would be of great value for future studies to explore the optimal timing of follow-up FLT PET scans since this is currently an area of uncertainty. Likely the optimal timing of PET scanning will not only depend on the particular immunotherapy but also the specific process being measured. For example, in this study the rationale for choosing the 12 week follow-up PET was based on the expected time frame for immune activation to occur following pTVG-HP vaccination (139). Nonetheless, some patients may have immune responses and meaningful changes in cell proliferation at earlier timepoints. As indicated, increases in thyroid FLT uptake were evident less than 1 day after injection of pembrolizumab. Perhaps a similar change in FLT uptake occurs in tumors with preexisting immune cell infiltrates that may offer an early marker of tumor response.

This work was limited in that bone marrow metastasis could not be evaluated using FLT PET/CT imaging. This is because of the high FLT uptake in non-diseased bone marrow that makes identification and segmentation of bone marrow metastases challenging. However, our group is currently working on developing image analysis tools to enable analysis of bone marrow metastases on FLT PET/CT images. Interestingly, for patients with bone marrow metastases and soft-tissue metastases, changes in FLT PET uptake in soft-tissue metastases alone, were predictive of clinical outcome.

7.5 Conclusion

In this chapter patients with metastatic prostate cancer were treated with pTVG-HP DNA vaccine and pembrolizumab. Increases in FLT uptake in the spleen and vaccine draining lymph

nodes suggest increased immune cell proliferation in these tissues is a pharmacodynamic effect of treatment. Changes in FLT uptake in soft-tissue tumors were predictive of progression free survival, indicating that changes in tumor cell proliferation may offer an early measure of tumor response. It was also found that baseline FLT uptake in the thyroid was predictive of the occurrence of thyroid-related adverse events. Together these results suggest PET imaging has potential as a biomarker in immunotherapy, providing a relative early marker of tumor and immune responses.

Chapter 8: Multi-modality FLT and FDG PET for imaging immune response in canine patients

8.1 Motivation

FLT PET has been shown to be more specific for assessing active tumor cell proliferation than FDG PET (140). This is particularly relevant in the context of immunotherapy where interpretation of FDG PET avid tumors is confounded by increases in glycolysis from immune cells infiltrating the tumor (18). However, FLT PET has been shown in some cases to have inferior sensitivity compared with FDG PET especially for assessing tumors with low proliferative rates (141,142). Incorporating concurrent FDG PET imaging for response assessment may help to overcome this limitation. One might expect a tumor response during immunotherapy to consist of decreases in tumor cell proliferation (FLT) and increases in glucose utilization due to immune cell infiltration into the tumor (FDG). To quantify this phenomenon, this chapter investigates multi-modality response assessment with FLT and FDG PET imaging. The tumor FDG/FLT SUV ratio is investigated as a biomarker of immune response in canines treated with mifamurtide immunotherapy. The ultimate clinical goal is to identify new techniques for measuring immune responses in patients undergoing immunotherapy.

8.2 Methodology

Mifamurtide is an analogue of a molecule found in bacterial cell walls; upon entering the blood stream mifamurtide binds to toll-like receptors on monocytes, stimulating the innate immune system. This discovery led to its development as an immunotherapy for treating cancer. Treatment with mifamurtide has been shown to improve outcomes for both canines and humans with osteosarcoma (143,144). In this chapter a canine with osteosarcoma was injected with

mifamurtide on days 0 and +4. FDG PET/MR scans were performed on days -1 and +6; FLT PET/CT scans were performed on days 0 and +7 (**Figure 28**).

Tumor and lymphoid organs were identified by a veterinary radiologist and manually segmented, allowing extraction of summary SUV metrics. All images were rigidly registered to the baseline FLT PET scan, enabling assessment of changes in tumor SUVs on a voxel-level. Since infiltration of immune cells into the tumor is believed to cause decreased tumor cell proliferation and increased glucose utilization, change in tumor FDG/FLT SUV ratio was used to quantify an immunotherapeutic response (increases in this ratio would indicate an immune response).

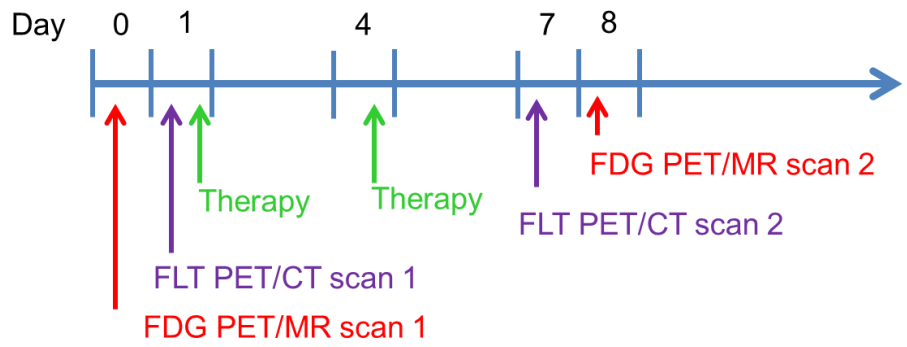

Figure 28: Schedule for canine treated with mifamurtide.

8.3 Results

The voxel-level analysis revealed heterogeneous changes in tumor cell proliferation, with sixty percent of tumor voxels (146 cm^3) exhibiting increases in FLT SUV (median +55%) and forty percent of voxels (97 cm^3) exhibiting decreases in FLT SUV (median -34%) (**Figure 29**).

Overall the tumor-level FLT SUV_{mean} was unchanged with a value of 2.9 g/mL at both baseline and follow-up (**Figure 30**). The tumor FDG SUV_{mean} increased 37% from 3.0 g/mL at baseline to 4.1 g/mL at follow-up. The tumor FDG/FLT SUV_{mean} ratio increased 40% from 1.0 at baseline to 1.4 at follow-up (**Figure 31**).

Assessment of lymphoid organs revealed SUV_{mean} changes in a non-metastatic lymph node to be -9% for FLT and +14% for FDG. Both tracers exhibited decreases in the spleen with FLT -1% and FDG -11%. Changes in the liver were +7 for FLT and -10% for FDG. Bone marrow (vertebrae L2–L7) changed +31% for FLT and -28% for FDG.

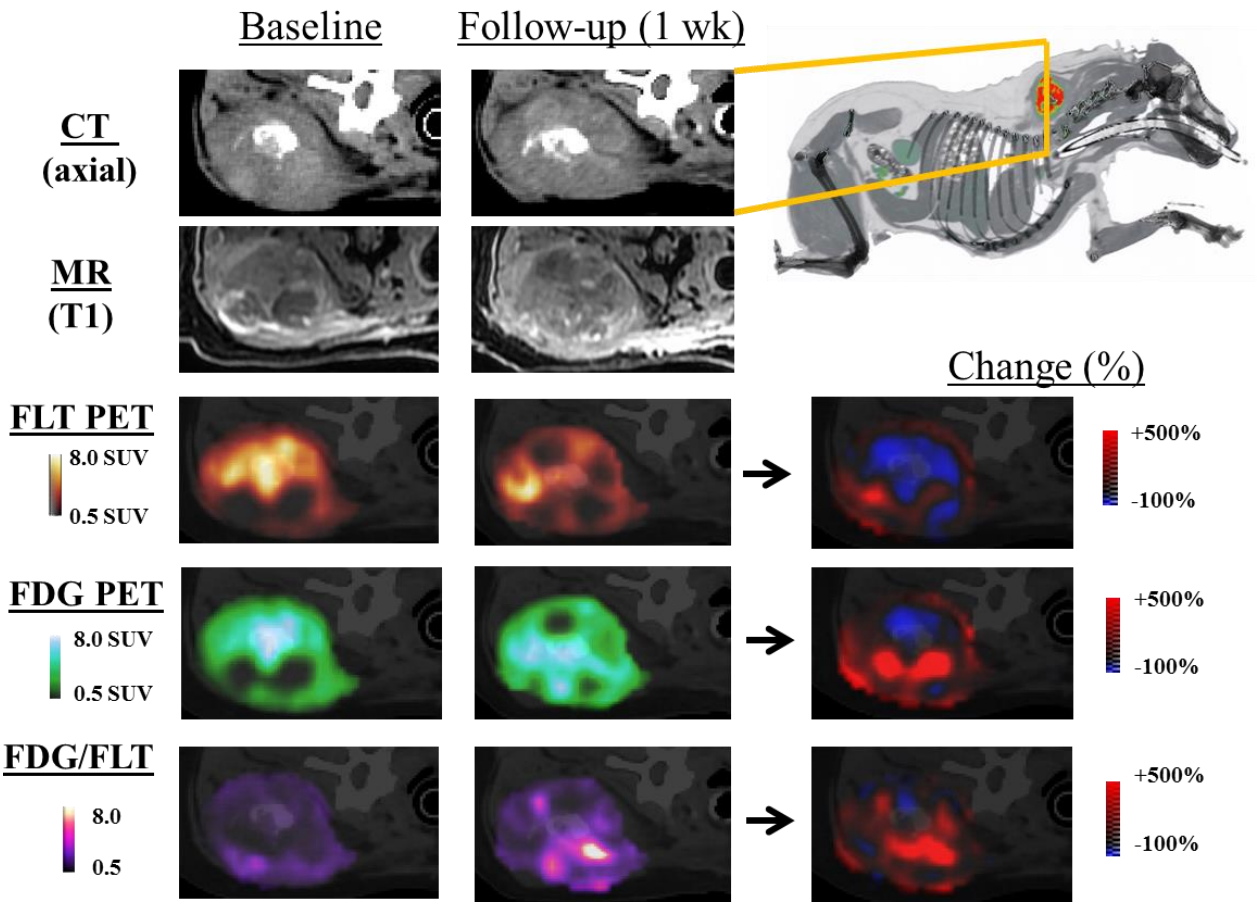

Figure 29: Axial slice of the tumor for various imaging modalities. The response maps reveal a spatially heterogeneous tumor response. Note PET images are overlaid on corresponding CT slices for reference and are upsampled to CT resolution for visualization.

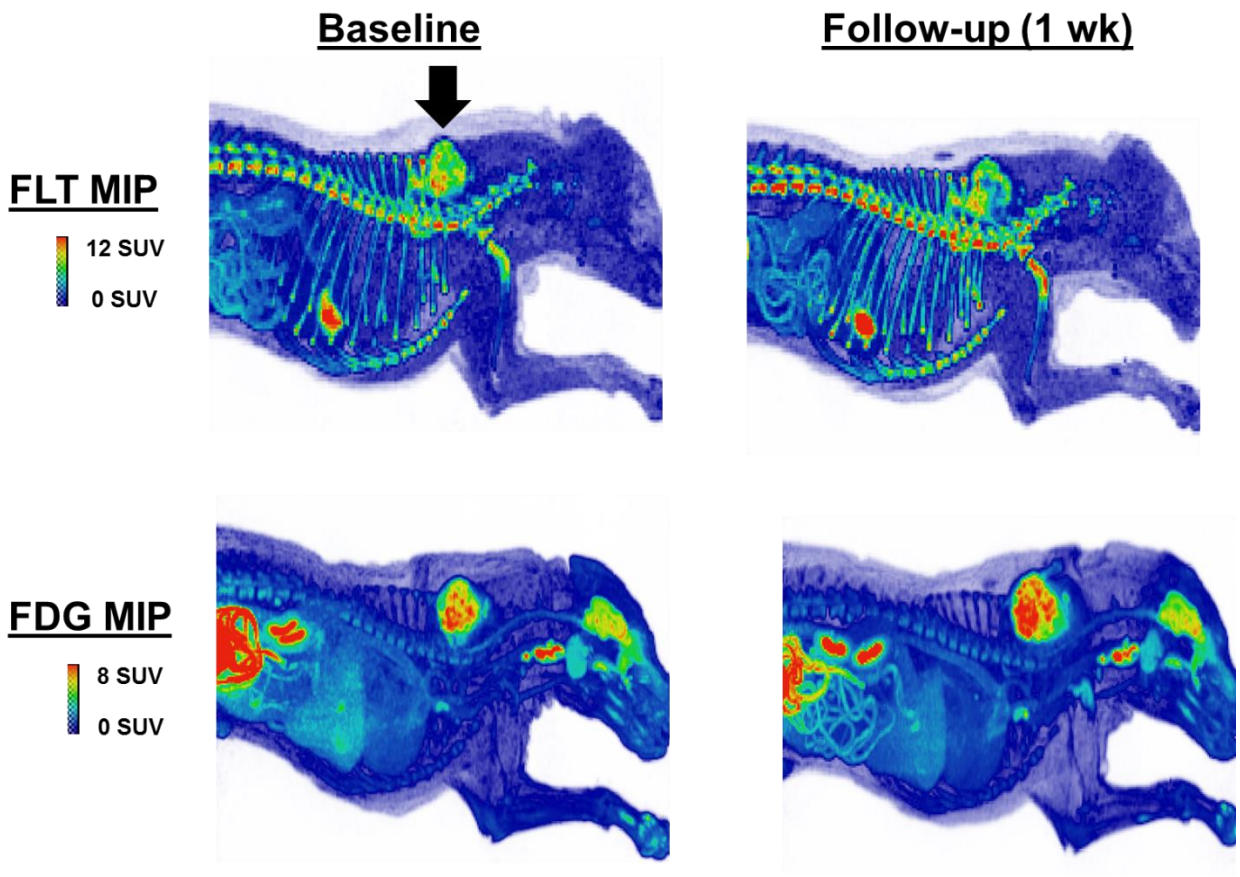

Figure 30: Maximum intensity projections (MIPs) of the baseline and follow-up FLT and FDG PET scans. Slightly diminished FLT uptake is evident in the tumor (black arrow) from baseline to follow-up. Increased FDG uptake is evident in the tumor from baseline to follow-up. Increased in FLT uptake is also visually evident in the bone marrow.

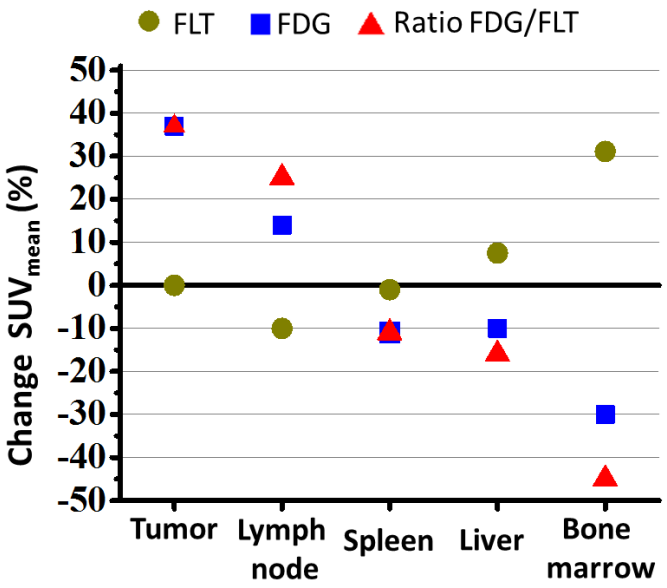

Figure 31: Change in SUV_{mean} in tumor and lymphoid organs from baseline to follow-up scans. Notably, the bone marrow (vertebrae L2 – L7) exhibited substantial increase in FLT SUV and decrease in FDG SUV during therapy.

8.4 Discussion

A voxel-based analysis revealed that different tumor regions experienced vastly different responses to mifamurtide immunotherapy. It suggests some regions within the tumor demonstrated increases and other regions demonstrated decreases in cell proliferation even though as a whole tumor cell proliferation was unchanged (0% change in SUV_{mean} from baseline to follow-up). If the tumor in this chapter were to have been biopsied at follow-up, one of the residually proliferating regions might have been removed and it may have been incorrectly concluded that the treatment had no effect. This underscores the importance of having imaging biomarkers to assess changes in the spatial heterogeneity of tumors during therapy.

The results of this chapter showed an increase in the tumor FDG/FLT uptake ratio after therapy. We believe this was caused by an increase in immune cells within the tumor region (increased FDG) and a relatively stable rate of tumor cell proliferation (unchanged FLT).

Previously it has been shown that immune cell infiltration into the tumor can lead to increased FDG uptake (18,145). This is supported by the results of this chapter where our canine patient experienced a 37% increase in tumor FDG SUV_{mean} after one week of immunotherapy. Typically, it would be impossible to differentiate whether this increased glycolytic activity was due to tumor progression or immune cell infiltration but the results of this chapter also showed no change in tumor FLT SUV_{mean}. This suggests tumor cell proliferation remained relatively stable during treatment and that the tumor was not progressing despite the increased glycolytic activity. This highlights the value of multi-modality response assessment. Having only the FDG PET or only the FLT PET may have led to the erroneous conclusion that the treatment was having little to no effect.

In this chapter it was shown that bone marrow FLT uptake increased and FDG uptake decreased during therapy with mifamurtide. The underlying causes of these changes are unknown; however, a plausible explanation is offered by the expected pharmacodynamic effects of mifamurtide. Previous studies have showed that low concentrations of toll-like receptor ligands in the blood stream drive emigration of monocytes from the bone marrow (146,147). After emigration from the bone marrow, monocytes enter the blood stream and stimulate the innate immune system (144). This suggests that treatment with the toll-like receptor agonist mifamurtide also leads to monocyte emigration from the bone marrow. Thus, the decrease in FDG uptake in the bone marrow may be explained by a drop in glycolytic activity that accompanies the emigration of monocytes out of the bone marrow. Similarly, the increase in FLT uptake may be caused by a compensatory increase in cell proliferation as the bone marrow replenishes the monocyte population. Regardless of the mechanism leading to the changes in PET uptake, the results suggest the bone marrow is an important mediator of mifamurtide

pharmacodynamic effects and biomarkers assessing this organ should be evaluated further in this context. Interestingly, this also suggests that FLT PET may be useful for evaluating bacterial infections wherein an innate immune response is triggered by bacterial molecules binding to toll-like receptors in a manner similar to mifamurtide.

8.5 Conclusion

Treatment with the innate immune stimulant mifamurtide led to an increase in the tumor FDG/FLT uptake ratio. We hypothesize that this phenomenon is due to an increase in the number of immune effecter cells within the tumor (increased FDG) and a relatively stable rate of tumor cell proliferation (unchanged FLT). These result warrant further study, including comparison with tissue histopathologic changes. Change in bone marrow FLT and FDG uptake suggest the bone marrow is an important mediator of mifamurtide pharmacodynamic effects and should be studied further in this context.

Section IV Concluding Remarks

Chapter 9: Summary and Future Work

The goal of this dissertation was to assess the clinical value of FLT PET as a biomarker of patient response to cancer therapy. In Section I, we developed methodologies to improve the quantitative accuracy FLT PET to enable more accurate response assessment. In Section II, we characterized the pharmacodynamic effects of various anti-angiogenic therapies using FLT PET, gaining insight into improved treatment strategies. In Section III, FLT PET was used to predict tumor responses to immunotherapy and to predict immune-related adverse events. This concluding chapter summarizes the major discoveries of this dissertation and describes how they could impact clinical utilization of PET imaging in the future.

9.1 Summary

Improving FLT PET quantification

The focus of Section 1 of this dissertation (Chapters 2-3) was improving the quantitative accuracy of FLT PET. The section consisted of two chapters each describing modelling approaches that might be utilized to improve quantitative accuracy in clinical studies. The following paragraphs reiterate the major results of these chapters.

In Chapter 2 of this dissertation we describe a compartmental modelling approach that can be used for FLT kinetic analysis. FLT kinetic analysis has been shown to lead to improved quantitative accuracy over FLT SUVs (40,49,50). However, the kinetic analysis methodology is more complicated than the SUV approach, including requirement of blood input function that must be corrected for FLT metabolism. In Chapter 2 we presented a non-invasive approach to correct for FLT metabolism. This approach is less invasive than other approaches that rely on

blood sampling during the dynamic imaging session and therefore offers a potentially more feasible approach for clinical implementation of FLT PET kinetic analysis. Additionally, in Chapter 2 we evaluated the ability of the FLT compartmental model to estimate kinetic parameters using Monte Carlo simulations. This provided some indication of the uncertainty in our kinetic parameter estimates, which is important for reliably applying this methodology to quantify patient responses to therapy. Ultimately this work helps facilitate use of dynamic PET scanning and FLT compartmental modelling in clinical studies to assess patient responses to therapy. The results led to the first published study reporting concurrent changes in tumor cell proliferation and vasculature during intermittent VEGFR-TKI therapy that is described in Chapter 5 of this dissertation (148).

In Chapter 3 we described a methodology to enable statistically powerful parametric modelling. Increasing statistical power can reduce uncertainties in parameter estimates and consequently improve the quantitative accuracy of FLT PET. The most straightforward way to increase statistical power is to acquire more data; in the case of PET imaging this can be expensive for researchers and burdensome for patients. An alternative way to increase statistical power is to utilize more powerful statistical methods for analyses. Parametric statistical modelling can provide superior statistical power over non-parametric approaches but requires the data follow a known distribution (74). This motivated Chapter 3 of this dissertation where we provided a methodology to identify transformations for providing normally distributed FLT PET SUVs. These normal transformations enable parametric statistical modelling that can lead to increased statistical power. This work led to the first published study to identify optimal normal transformations for FLT PET SUVs, including an investigation of how therapy affects these optimal transformations (149). It facilitates incorporation of parametric statistical modelling into

clinical trials that utilize FLT PET imaging. It enables researchers to include parametric modelling into study designs to increase statistical power, potentially reducing the number of patients and expenses required to meet clinical endpoints. As demonstrated in Chapter 6 of this dissertation, parametric modelling enable analysis of changes in tumor FLT SUVs by accounting for correlations in tumor SUVs arising from the same patient. The methodology outlined in Chapter 3 for identifying normal data transformations need not be limited to analysis of medical images and could be applied more broadly to any medical biomarker to improve understanding of distribution behavior. Going forward this methodology will help to minimize errors in statistical testing and facilitate selection of appropriate tests to maximize statistical power.

FLT PET as a biomarker of response in anti-angiogenic therapy

In Section II of this dissertation, FLT PET was applied as a biomarker of response during anti-angiogenic therapy. The work was motivated by the fact that the majority of metastatic cancer patients treated with anti-angiogenic therapy will experience only modest improvements in survival. Novel therapeutic combinations have been shown to improve outcomes in anti-angiogenic therapy; however, there are cases where combination therapy has failed, particularly in the context of VEGFR-TKIs and chemotherapies (5,97,98). These failures highlight the importance of having identified physiologic targets for synergistic combination therapy. The purpose of Section II (Chapter 4-6) of this dissertation was to utilize FLT PET to provide greater understanding of the clinical pharmacodynamics of VEGFR-TKIs and gain insight into improved anti-angiogenic treatment strategies.

It has been hypothesized that normalization of tumor vasculature brought about by anti-angiogenic therapy would lead to improved vascular function and drug delivery; this formed the rationale for numerous studies aiming to concurrently combine anti-angiogenic therapy and

chemotherapy (1,150). This hypothesis proved successful when combining VEGF-ligand targeting agents such as bevacizumab with chemotherapy. However, it proved less successful when combining VEGFR-TKIs with chemotherapy (5,97-102). The results in Chapters 4 and 5 of this dissertation showed that treatment with VEGFR-TKI led to reductions in FLT PET parameters representing tumor vascular function that could abrogate concurrent treatment with chemotherapy. This offers a plausible explanation for why studies concurrently combining VEGFR-TKI and chemotherapies have not led to improved outcomes.

Chapter 4 revealed that recurrent VEGFR-TKI treatment breaks leads to a withdrawal flare characterized by a rebound in tumor FLT uptake that, after 7 days of treatment break, is not significantly different from baseline levels of FLT uptake. This rebound flare was present in multiple intermittent treatment cycles suggesting it may be an opportune time to schedule synergistic therapy. These results led to the first published study documenting this recurring withdrawal flare (151). Chapter 5 built on the work of Chapter 4 to further explore the physiologic causes of the withdrawal flare using dynamic FLT PET with compartmental modelling. Increases in vascular and proliferative FLT PET kinetic parameters during axitinib washout suggested a disease rebound. This provided further evidence that VEGFR-TKI treatment breaks would be an optimal time for scheduling synergistic cell-cycle specific chemotherapy (148). These results indicate that FLT PET can provide therapeutic insights for more evidence-based development of combination therapies. This is an under-appreciated use of molecular imaging in clinical trials that often focus on utilizing molecular imaging solely for diagnoses or outcome prediction.

The results of Chapters 4 and 5 led in part to a novel treatment paradigm where cell-cycle specific chemotherapy was applied in sequential combination with VEGR-TKI therapy to

capitalize on the withdrawal flare. This treatment paradigm was evaluated in Chapter 6 using FLT PET imaging. It was found that application of cell-cycle-specific chemotherapy during VEGFR-TKI treatment breaks led to a greater reduction in FLT uptake than VEGFR-TKI treatment alone or chemotherapy alone. This suggests the sequential combination of VEGFR-TKI and chemotherapy is synergistic and offers a potentially improved treatment strategy for metastatic cancer patients. These finding have been subsequently published in a peer-reviewed journal (152).

It has been assumed that selective VEGFR-TKIs, primarily target VEGFRs on endothelial cells, leading to disruption of tumor vasculature and diminished tumor growth (153). The results of Section II support this hypothesis with the majority of patients experiencing simultaneous decreases in proliferative and vascular FLT kinetic parameters during axitinib (VEGFR-TKI) treatment. However, lack of correlation between changes in these parameters, suggests the anti-proliferative activity of axitinib cannot be inferred solely from assessing changes in tumor vasculature. This indicates vascular changes occurring in tumors as a result of axitinib therapy may not be the only cause of delayed tumor growth. Furthermore, in vitro studies have showed that neuroblastoma cell lines had significantly diminished proliferation after treatment with axitinib, suggesting axitinib may have direct anti-proliferative activity against tumor cells that is decoupled from its anti-vascular effects (112). Taken together, these results indicate biomarkers limited to assessing vascular pharmacodynamics may not fully capture the mechanistic actions of VEGFFR-TKIs such as axitinib. Emerging interest in novel VEGFR-TKI treatment schedules that directly target tumor cells rather than tumor vasculature indicates an additional need for modalities that provide concurrent assessment of tumor cell proliferation and vasculature (154). This underlies the potential advantage of molecular imaging with FLT PET

over conventional modalities (DCE-MRI, DCE-US, DCE-CT) that are limited to assessing only the vascular pharmacodynamics of anti-angiogenic therapies. Taken as a whole, Section II of this dissertation definitively establishes FLT PET as a clinically relevant biomarker for characterizing the pharmacodynamic effects of anti-angiogenic agents and demonstrates how it can lead to development of new combination treatment strategies.

FLT PET as a biomarker of response in immunotherapy

Section III of this dissertation (Chapters 7-8) investigates use of FLT PET as a biomarker in immunotherapy. Anti-PD1 therapies are actively being researched as treatment for patients with metastatic cancer; however, identifying a reliable biomarker to predict responding patients has remained elusive (155). No prior study has assessed the predictive value of FLT PET during anti-PD1 therapy. The two prior studies that have utilized FLT PET for response assessment in immunotherapy identified immune responses in lymphoid organs (132,133). Thus, in Section III of this dissertation we aimed to determine whether FLT PET detects changes in lymphoid organs and evaluate the predictive value of FLT PET during immunotherapy.

Chapter 7 of this dissertation is the first reported use of FLT PET to evaluate patient responses to anti-PD1 therapy in a clinical study. The results showed that FLT PET uptake was predictive of progression free survival as well as immune-related adverse events. The results indicate that FLT PET biomarkers, in the context of anti-PD1 immunotherapy of prostate cancer, may provide earlier markers of patient response than traditional clinical measures such as patient PSA or tumor anatomic size. The ramifications of this, if validated in larger patient cohorts, suggest that physicians may be able to utilize FLT PET scans to make timely, data-driven, clinical decisions to improve patient care. For example lack or tumor response on FLT PET

would indicate it is time to move on to a new therapy. This could save patients months of wasted time on ineffective treatment regimens, which is crucial for patients with metastatic cancer who may only have a few months to live without effective treatment. It may also be that physicians could use the FLT PET to identify patients at risk to experiencing an immune-related adverse event. This could lead to treatment with drugs to prevent or mitigate the adverse event.

Chapter 8 of this dissertation investigates utilization of multi-modality FLT PET and FDG PET imaging to evaluate mifamurtide immunotherapy. The results demonstrated how FDG may be combined with FLT PET to improve identification of immune responses. An increase in the tumor FDG/FLT uptake ratio was found during immunotherapy. This was the result of unchanged tumor FLT uptake and increased FDG uptake, suggesting an immune response characterized by immune cell infiltration into the tumor. In addition notable increases in FLT uptake were found in the bone marrow that suggested increased cell proliferation in the bone marrow as a pharmacodynamic effect of mifamurtide immunotherapy.

Taken as a whole, the results of Section III of this dissertation indicate clinical potential for FLT PET as a non-invasive, whole-body, biomarker in immunotherapy. Given the relatively few published studies utilizing FLT PET for evaluating immunotherapy, there is an opportunity to further expand FLT PET into other immunotherapeutic settings and even more generally as a biomarker of the immune system.

9.2 Future Directions

Chapter 2 describes a methodology for dynamic PET scanning and FLT compartmental modelling. This methodology is aimed at making dynamic PET scanning clinically feasible by deriving a population based correction for FLT metabolism that does not require blood sampling.

Chapter 5 highlights the clinical value of this methodology by applying it to characterize vascular and proliferative changes occurring in tumors during anti-angiogenic therapy. There are still a number of challenges that need to be addressed before widespread utilization of dynamic FLT PET imaging can take place clinically. This includes kinetic modelling software that is standardized across scanners and institutions. The work in this thesis has in-part contributed to an effort to commercialize kinetic analysis software by incorporating it directly into GE Healthcare's Advantage Workstation. This would help to standardize the software analysis, making comparisons across scanners more feasible.

The large uncertainties in FLT PET kinetic parameters that were described in detail in Chapters 2 indicates reduction of parameter uncertainties is necessary before changes in kinetic parameters of individual patients can be used to guide clinical decision making. This might include for example, image-processing to increase the signal-to-noise ratio of early dynamic PET frames (156). It may also include optimization of the reconstruction parameters for each dynamic frame or even estimation of kinetic parameters directly from the raw projection (157). Nonetheless, this dissertation provides insight into how dynamic FLT PET may be used in the future to investigate the mechanistic actions of therapeutic agents.

Chapter 3 demonstrated how normal transformations enable parametric statistical modelling and increased statistical power when analyzing PET data. In the future, this methodology could be applied to identify normal transformations to distributions of imaging-based parameters derived from other imaging modalities such as magnetic resonance and computed tomography. For example, an endpoint for clinical trials often includes the objective response rate measured following RECIST i.e. the percentage of patients who experience measurable decreases in tumor size during the study. These measurements of tumor size are

made by summing the diameters of tumors within a patient on CT or MRI scan. The changes in the sum of the tumor diameters are tracked throughout the course of therapy and a patient is classified as having a partial response if the sum of tumor diameters decreases by 30% or more (13). An analysis with greater statistical power would take into account the responses of each individual lesion rather than overall sum of diameters. The inherent correlation resulting from changes in lesion diameters within the same patient could be accounted for with parametric statistical modelling (after normal transformations have been applied). This is one area where the normal transformation methodology of this dissertation could be applied to improve statistical power in clinical trials.

Although the analysis in Chapter 3 focused on normal transformations for tumor summarized SUV metrics (SUV_{max}, SUV_{mean}, etc.), the methodology could be extended to voxel-level SUV distributions from tumors or organs. For example, one may wish to normalize the voxel-level SUV distributions within healthy organs so that identification of outlier voxels indicative of pathology would become probabilistic and intuitive (158). In this case, normal transformations could be of great value for disease diagnosis, where knowing underlying biomarker distributions in healthy and diseased patients might aid in discriminating between the two (159,160). This is already being investigated within our research group, where we are generating reference normal distributions of FLT SUVs in the bone marrow of healthy patients (**Figure 32**). These reference distributions will be utilized to identify regions of abnormal bone marrow uptake in a prospectively scanned patient based on their deviations from the reference normal distribution.

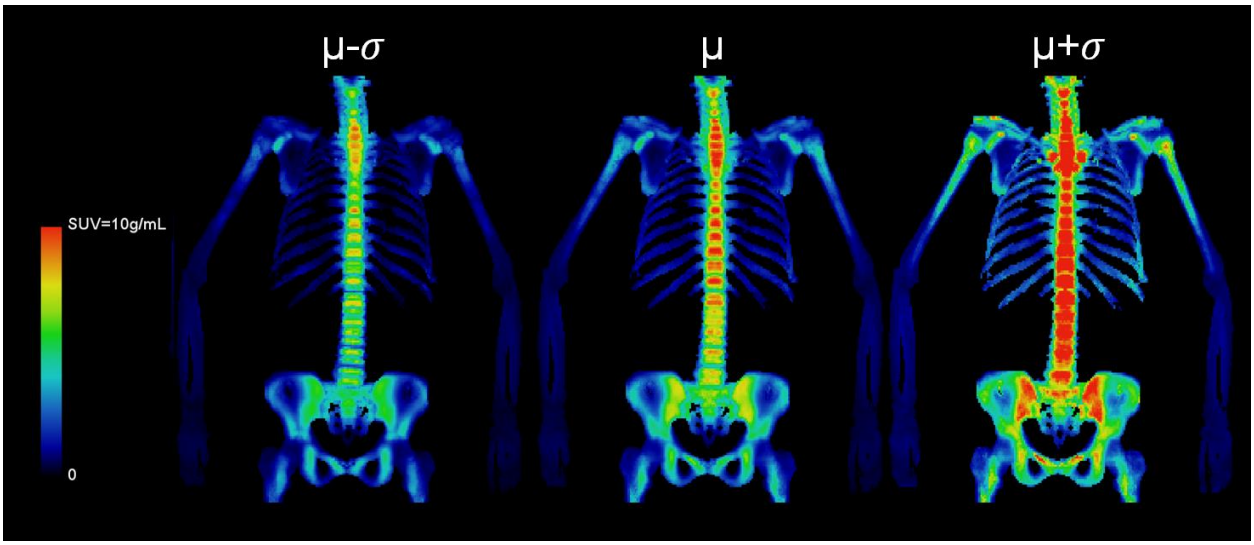

Figure 32: Reference distribution of healthy bone marrow FLT uptake. This statistical appearance model was generated by analyzing the distribution of FLT SUVs in each region of bone marrow for a cohort of patients. (Courtesy of Timothy Perk)

Chapter 7 of this thesis provided evidence that FLT PET may be a valuable biomarker for assessing response in immunotherapy. Changes in FLT uptake in lymphoid organs shed insight into the pharmacodynamic effects of immunotherapy. However, to reach its full potential the underlying mechanisms driving FLT PET uptake must be identified. This includes for example, understanding the biology that leads to increased FLT uptake in thyroids of patient most likely to experience thyroid-related adverse events. Utilizing other immune specific PET agents is one way to further investigate the underlying biologic mechanisms influencing FLT PET uptake during immunotherapy. FLT PET cannot distinguish between proliferation of immune cells and proliferation of tumor cells, limiting its specificity. However, more specific PET tracers are under development for imaging specific components of the immune system (**Table 19**). For example, a phase I dose escalation study incorporated PET imaging with a ^{89}Zr-labelled anti-CD44 antibody to assess organ specific and non-specific uptake of the anti-CD44 immunotherapeutic agent RG7356 (161). The authors concluded that specific target mediated uptake of anti-CD44 antibody was evident in the spleen, liver, bone marrow, kidney, and lung.

This PET agent might be utilized in conjunction with FLT PET to indicate whether changes in FLT uptake in lymphoid organs during immunotherapy are indeed due to changes in immune cells or potentially driven by other mechanisms.

Chapter 8 provided some preliminary evidence that the uptake ratio of FDG/FLT may be a valuable biomarker of immune response in tumors. An area of future work within our group aims to utilize this phenomenon to assess whether multi-modality imaging with FDG and FLT PET provides a prognostic marker of immune response in metastatic melanoma patients treated with an immune checkpoint inhibitor. A crucial next step will be performing studies that relate the FDG/FLT uptake ratio to clinical endpoints or histopathology results, providing validation of its use as an imaging biomarker of immune response.

Interestingly, the results in Chapter 8 suggest that stimulates of the innate immune system (not just immunotherapies) may be detectable with FLT PET imaging. The drug utilized in Chapter 8 was a molecular analogue of a molecule found in bacterial cell walls, which after injection stimulates the innate immune system (143). This drug led to an increase in FLT uptake in canine bone marrow after six days of treatment. This is assumed to be due to activation of the innate immune system, causing a corresponding increase in proliferation of immature immune cells within the bone marrow. A similar innate immune system response would be expected following a bacterial infection (18). Thus, elevated FLT PET uptake in the bone marrow may indicate a potential bacterial infection. PET imaging of bacterial infections is an active area of research although limited specificity, among other challenges, has hindered widespread adoption of any one tracer (162). FLT PET has not been explored for evaluating bacterial infections. The results of this dissertation at the very least suggest FLT PET should be considered as a potential tracer for assessing infections and shedding new insights into the pathogenesis of infections. For

example, FDG PET has been shown to poorly differentiate true infection from sterile inflammation (162); in these cases FLT PET bone marrow assessments may provide a more specific indication of an infection.

The work in this dissertation is supportive of continued development of FLT PET, as it offers a readily-available clinical tool to measure tumor responses to therapy. The results of Chapters 4-6 suggest that static and dynamic FLT PET/CT imaging of changes in tumor vasculature and cell proliferation may be sufficient for characterizing the pharmacodynamic effects of anti-angiogenic therapies. However, the results of this dissertation are also supportive of multi-modality imaging that combines FLT PET and other imaging biomarkers in cases where a more comprehensive evaluation is required. As shown in Chapter 8 of this dissertation, multi-modality PET imaging was useful for characterizing the canine patient's response to mifamurtide immunotherapy. Multi-modality imaging with FLT PET and immune-specific PET tracers (**Table 19**) would be especially beneficial in immunotherapy. For example, it may enable determination of the contributions of immune cells and tumor cells to the overall proliferative rate and changes in this rate during immunotherapy. Without the biopsy results in Chapter 7, it would have been difficult to determine whether changes in tumor FLT uptake were due to changes in immune cell proliferation or tumor cell proliferation. Combining FLT PET imaging with more specific PET tracers that bind specifically to immune cells would shed further insights into the spatial and temporal effects of immunotherapy and mitigate the need for invasive biopsies to differentiate tumor and immune cell proliferation. Given the breadth of immunotherapeutic agents, it is likely that the optimal imaging biomarkers will depend on the mechanisms of the particular immunotherapy and the clinical problem being addressed.

Regardless, this dissertation provides strong evidence supporting further development of FLT PET for assessing immunotherapy and tumor responses more generally.

Table 19: Studies utilizing PET tracers that specifically target immune system pathways and may benefit from multi-modality imaging with FLT PET

PET Tracer	# Patients	Tumor Type	Treatment	Imagine time points	Notable Results	Ref.
^{89}Zr-RG7356	13	CD44-expressing solid tumours	RG7356 (anti-CD-44)	1, 24, and 96 hours post-injection	Dose escalation study with patient receiving different doses of RG7356 followed by a 1mg injection of ^{89}Zr-RG7356 Dose-dependent uptake of ^{89}Zr-RG7356 was evident in the spleen, liver, bone marrow, lung, and kidney indicating target-specific uptake in these organs Study demonstrates a method to differentiate target specific and non-specific uptake of monoclonal antibodies as a means to aide drug development	(161)
^{18}F-FHBG	7	Glioma	CAR T cell therapy	Baseline and after two to five weeks	A significant increase in [^{18}F]FHBG Uptake was evident in tumors after CAR T cell injection suggesting T cell trafficking to tumors; however, authors could not rule out the fact that increased uptake may also have been the result of diminished blood brain barrier This study demonstrates the potential of reporter gene imaging to characterize the in vivo viability and trafficking of cytotoxic T lymphocites	(163)
^{64}Cu-DOTA-anti-CTLA-4	Variable	Colon cancer	Anti-mouse CTLA-4 mAb		Tumors demonstrated visually increased uptake of ^{64}Cu-DOTA-anti-CTLA-4 and this was verified with ex-vivo biodistribution analysis This type of assessment may enable selection of patients for anti-CTLA immunotherapies	(164)
^{64}Cu-DOTA-ipilimumab	12	Non-small cell lung cancer	Ipilimumab (anti-CTLA-4)	6, 24, and 48 hours after injection	This studied aimed to characterize binding of radiolableled ipilimumab to non small cell lung cancer cells in vivo in mice In vivo PET finding showed increased uptake in three tumor cell lines in vivo and were in concordance with in vitro and ex	(165)

					vivo measurements of CTLA-4 expression Tracer uptake in tumors decreased following injection of excess unlabaled ipilimumab indicating specific tracer uptake in the tumor	
^{64}Cu-NOTA-PD-1 and ^{64}Cu-NOTA-PD-L1	Variable	Melanoma	Checkpoint blocking monoclonal antibodies combined with radiotherapy	24 hours after injection	Following immunoradiotherapy, tumor, lymph node, and spleen uptake was higher in wild type mice than in antigen-blocked mice, suggesting specificity of ^{64}Cu-NOTA-PD-1 to PD-1 expressing cells. Similar results were found for ^{64}Cu-NOTA-PD-L1. After treating mice with IFN-γ, pronounced ^{64}Cu-NOTA-PD-L1 induction was evident in the lungs. The authors concluded the lung is strongly protected against immune attacks by PD-L1 upregulation	(166)
^{89}Zr-DFO-CD3 (anti-CD3 PET)	Variable	Colon carcinoma	Anti-CTLA-4	Mid-treatment	^{89}Zr-DFO-CD3 PET stratified mice into low and high tumor uptake groups with no significant difference in tumor size between the low and high uptake groups. However, by the end of treatment, the low uptake group had significantly larger tumor volume than the high uptake group, suggesting ^{89}Zr-DFO-CD3 PET may be useful as a response-based biomarker.	(167)
^{89}Zr-malDFO-169 cDb (anti-CD8 PET)	Variable		Adoptive cell transfer therapy, anti-CD137 antibody therapy, and anti-PD-L1 therapy	Baseline and midtreatment	Following infusion of tumor antigen-specific T cells, anti-CD8 PET detected increased uptake in tumors compared with antigen negative control tumors. Further relatively large increase in uptake was observed in axillary draining lymph node. Following anti-Cd137 therapy, anti-CD8 PET showed higher uptake in tumors compared with tumors of CD8 blocked mice. Further immunohistochemistry confirmed presence of CD8+ tumor-infiltrating T cells in tumors. Uptake in lymph nodes increased during therapy, which the authors believed due to the systemic agonistic activity of therapy on immune cells throughout the body. Following anti-PD-L1 therapy, anti-CD8 PET showed higher tumor uptake in responders than in non-responders and the result was confirmed ex vivo. Interestingly, a	(168)

	rim of uptake was seen on the periphery of non-responding tumors suggesting presence of T cells but no infiltration within the tumor.

9.3 Conclusion

This dissertation developed FLT PET imaging as a response biomarker to guide treatment decisions and develop improved therapeutic strategies. FLT PET was utilized as a pharmacodynamic biomarker to understand the mechanistic actions of anti-angiogenic therapy. The insight into drug pharmacodynamics facilitated development of a new treatment strategy wherein anti-angiogenic therapy and chemotherapy are sequentially combined. We showed that changes in FLT uptake in tumors allowed prediction of patient responses to immunotherapy. Additionally, we showed that changes in FLT uptake in non-diseased tissues (spleen, draining lymph nodes, thyroid) may provide useful information regarding the mechanistic action of immunotherapeutic agents and immune related-adverse events. As a whole, the work is highly supportive of continued use of quantitative FLT PET as a clinical tool to facilitate precision medicine, guiding evaluation of new therapeutic strategies and providing an early marker of patient response.

References

1. Jain RK. Normalization of tumor vasculature: an emerging concept in antiangiogenic therapy. Science **2005**;307(5706):58-62 doi 10.1126/science.1104819.
2. Hurwitz H, Fehrenbacher L, Novotny W, Cartwright T, Hainsworth J, Heim W, *et al.* Bevacizumab plus irinotecan, fluorouracil, and leucovorin for metastatic colorectal cancer. N Engl J Med **2004**;350(23):2335-42 doi 10.1056/NEJMoa032691.
3. Sandler A, Gray R, Perry MC, Brahmer J, Schiller JH, Dowlati A, *et al.* Paclitaxel-carboplatin alone or with bevacizumab for non-small-cell lung cancer. N Engl J Med **2006**;355(24):2542-50 doi 10.1056/NEJMoa061884.
4. Perren TJ, Swart AM, Pfisterer J, Ledermann JA, Pujade-Lauraine E, Kristensen G, *et al.* A phase 3 trial of bevacizumab in ovarian cancer. N Engl J Med **2011**;365(26):2484-96 doi 10.1056/NEJMoa1103799.
5. Carrato A, Swieboda-Sadlej A, Staszewska-Skurczynska M, Lim R, Roman L, Shparyk Y, *et al.* Fluorouracil, leucovorin, and irinotecan plus either sunitinib or placebo in metastatic colorectal cancer: a randomized, phase III trial. J Clin Oncol **2013**;31(10):1341-7 doi 10.1200/JCO.2012.45.1930.
6. Kindler HL, Niedzwiecki D, Hollis D, Sutherland S, Schrag D, Hurwitz H, *et al.* Gemcitabine plus bevacizumab compared with gemcitabine plus placebo in patients with advanced pancreatic cancer: phase III trial of the Cancer and Leukemia Group B (CALGB 80303). J Clin Oncol **2010**;28(22):3617-22 doi 10.1200/JCO.2010.28.1386.
7. Miller KD, Chap LI, Holmes FA, Cobleigh MA, Marcom PK, Fehrenbacher L, *et al.* Randomized phase III trial of capecitabine compared with bevacizumab plus capecitabine in patients with previously treated metastatic breast cancer. J Clin Oncol **2005**;23(4):792-9 doi 10.1200/JCO.2005.05.098.
8. Gnjatic S, Bronte V, Brunet LR, Butler MO, Disis ML, Galon J, *et al.* Identifying baseline immune-related biomarkers to predict clinical outcome of immunotherapy. J Immunother Cancer **2017**;5:44 doi 10.1186/s40425-017-0243-4.
9. Rizvi NA, Hellmann MD, Snyder A, Kvistborg P, Makarov V, Havel JJ, *et al.* Cancer immunology. Mutational landscape determines sensitivity to PD-1 blockade in non-small cell lung cancer. Science **2015**;348(6230):124-8 doi 10.1126/science.aaa1348.
10. Snyder A, Makarov V, Merghoub T, Yuan J, Zaretsky JM, Desrichard A, *et al.* Genetic basis for clinical response to CTLA-4 blockade in melanoma. N Engl J Med **2014**;371(23):2189-99 doi 10.1056/NEJMoa1406498.
11. Masucci GV, Cesano A, Hawtin R, Janetzki S, Zhang J, Kirsch I, *et al.* Validation of biomarkers to predict response to immunotherapy in cancer: Volume I - pre-analytical and analytical validation. J Immunother Cancer **2016**;4:76 doi 10.1186/s40425-016-0178-1.

12. Cohen JD, Li L, Wang Y, Thoburn C, Afsari B, Danilova L, *et al.* Detection and localization of surgically resectable cancers with a multi-analyte blood test. Science **2018**;359(6378):926-30 doi 10.1126/science.aar3247.

13. Eisenhauer EA, Therasse P, Bogaerts J, Schwartz LH, Sargent D, Ford R, *et al.* New response evaluation criteria in solid tumours: revised RECIST guideline (version 1.1). Eur J Cancer **2009**;45(2):228-47 doi 10.1016/j.ejca.2008.10.026.

14. Wolchok JD, Hoos A, O'Day S, Weber JS, Hamid O, Lebbé C, *et al.* Guidelines for the evaluation of immune therapy activity in solid tumors: immune-related response criteria. Clin Cancer Res **2009**;15(23):7412-20 doi 10.1158/1078-0432.CCR-09-1624.

15. Yankeelov TE, Abramson RG, Quarles CC. Quantitative multimodality imaging in cancer research and therapy. Nat Rev Clin Oncol **2014**;11(11):670-80 doi 10.1038/nrclinonc.2014.134.

16. Yankeelov TE, Mankoff DA, Schwartz LH, Lieberman FS, Buatti JM, Mountz JM, *et al.* Quantitative Imaging in Cancer Clinical Trials. Clin Cancer Res **2016**;22(2):284-90 doi 10.1158/1078-0432.CCR-14-3336.

17. 2018 American Cancer Soceity. <https://www.cancer.org/>.

18. Tumeh PC, Radu CG, Ribas A. PET imaging of cancer immunotherapy. J Nucl Med **2008**;49(6):865-8 doi 10.2967/jnumed.108.051342.

19. Wahl RL, Jacene H, Kasamon Y, Lodge MA. From RECIST to PERCIST: Evolving Considerations for PET Response Criteria in Solid Tumors. Journal of Nuclear Medicine **2009**;50(Suppl 1):122S-50S doi 10.2967/jnumed.108.057307.

20. Vasudev NS, Reynolds AR. Anti-angiogenic therapy for cancer: current progress, unresolved questions and future directions. Angiogenesis **2014**;17(3):471-94 doi 10.1007/s10456-014-9420-y.

21. Shields AF, Grierson JR, Dohmen BM, Machulla HJ, Stayanoff JC, Lawhorn-Crews JM, *et al.* Imaging proliferation in vivo with [F-18]FLT and positron emission tomography. Nat Med **1998**;4(11):1334-6 doi 10.1038/3337.

22. Hoeben BA, Troost EG, Span PN, van Herpen CM, Bussink J, Oyen WJ, *et al.* 18F-FLT PET during radiotherapy or chemoradiotherapy in head and neck squamous cell carcinoma is an early predictor of outcome. J Nucl Med **2013**;54(4):532-40 doi 10.2967/jnumed.112.105999.

23. Ott K, Herrmann K, Schuster T, Langer R, Becker K, Wieder HA, *et al.* Molecular imaging of proliferation and glucose utilization: utility for monitoring response and prognosis after neoadjuvant therapy in locally advanced gastric cancer. Ann Surg Oncol **2011**;18(12):3316-23 doi 10.1245/s10434-011-1743-y.

24. Sohn HJ, Yang YJ, Ryu JS, Oh SJ, Im KC, Moon DH, *et al.* [18F]Fluorothymidine positron emission tomography before and 7 days after gefitinib treatment predicts response in patients with advanced adenocarcinoma of the lung. Clin Cancer Res **2008**;14(22):7423-9 doi 10.1158/1078-0432.CCR-08-0312.

25. Liu G, Jeraj R, Vanderhoek M, Perlman S, Kolesar J, Harrison M, *et al.* Pharmacodynamic study using FLT PET/CT in patients with renal cell cancer and other

solid malignancies treated with sunitinib malate. Clin Cancer Res **2011**;17(24):7634-44 doi 10.1158/1078-0432.CCR-11-1677.

26. Chen W, Delaloye S, Silverman DH, Geist C, Czernin J, Sayre J, *et al.* Predicting treatment response of malignant gliomas to bevacizumab and irinotecan by imaging proliferation with [18F] fluorothymidine positron emission tomography: a pilot study. J Clin Oncol **2007**;25(30):4714-21 doi 10.1200/JCO.2006.10.5825.

27. McKinley ET, Smith RA, Tanksley JP, Washington MK, Walker R, Coffey RJ, *et al.* [18F]FLT-PET to predict pharmacodynamic and clinical response to cetuximab therapy in Ménétrier's disease. Ann Nucl Med **2012**;26(9):757-63 doi 10.1007/s12149-012-0636-x.

28. Schwarzenberg J, Czernin J, Cloughesy TF, Ellingson BM, Pope WB, Geist C, *et al.* 3'-deoxy-3'-18F-fluorothymidine PET and MRI for early survival predictions in patients with recurrent malignant glioma treated with bevacizumab. J Nucl Med **2012**;53(1):29-36 doi 10.2967/jnumed.111.092387.

29. Kishino T, Hoshikawa H, Nishiyama Y, Yamamoto Y, Mori N. Usefulness of 3'-deoxy-3'-18F-fluorothymidine PET for predicting early response to chemoradiotherapy in head and neck cancer. J Nucl Med **2012**;53(10):1521-7 doi 10.2967/jnumed.111.099200.

30. Zander T, Scheffler M, Nogova L, Kobe C, Engel-Riedel W, Hellmich M, *et al.* Early prediction of nonprogression in advanced non-small-cell lung cancer treated with erlotinib by using [(18)F]fluorodeoxyglucose and [(18)F]fluorothymidine positron emission tomography. J Clin Oncol **2011**;29(13):1701-8 doi 10.1200/JCO.2010.32.4939.

31. Kobe C, Scheffler M, Holstein A, Zander T, Nogova L, Lammertsma AA, *et al.* Predictive value of early and late residual 18F-fluorodeoxyglucose and 18F-fluorothymidine uptake using different SUV measurements in patients with non-small-cell lung cancer treated with erlotinib. Eur J Nucl Med Mol Imaging **2012**;39(7):1117-27 doi 10.1007/s00259-012-2118-8.

32. Wieder HA, Geinitz H, Rosenberg R, Lordick F, Becker K, Stahl A, *et al.* PET imaging with [18F]3'-deoxy-3'-fluorothymidine for prediction of response to neoadjuvant treatment in patients with rectal cancer. Eur J Nucl Med Mol Imaging **2007**;34(6):878-83 doi 10.1007/s00259-006-0292-2.

33. Wieder H, Beer AJ, Siveke J, Schuster T, Buck AK, Herrmann K, *et al.* F-fluorothymidine PET for predicting survival in patients with resectable pancreatic cancer. Oncotarget **2018**;9(11):10128-34 doi 10.18632/oncotarget.24176.

34. McKinley ET, Watchmaker JM, Chakravarthy AB, Meyerhardt JA, Engelman JA, Walker RC, *et al.* [(18)F]-FLT PET to predict early response to neoadjuvant therapy in KRAS wild-type rectal cancer: a pilot study. Ann Nucl Med **2015**;29(6):535-42 doi 10.1007/s12149-015-0974-6.

35. Hoshikawa H, Yamamoto Y, Mori T, Kishino T, Fukumura T, Samukawa Y, *et al.* Predictive value of SUV-based parameters derived from pre-treatment (18)F-FLT PET/CT for short-term outcome with head and neck cancers. Ann Nucl Med **2014**;28(10):1020-6 doi 10.1007/s12149-014-0902-1.

36. Herrmann K, Buck AK, Schuster T, Abbrederis K, Blümel C, Santi I, *et al.* Week one FLT-PET response predicts complete remission to R-CHOP and survival in DLBCL. Oncotarget **2014**;5(12):4050-9 doi 10.18632/oncotarget.1990.

37. Belohlavek O, Fencl P, Majovsky M, Jaruskova M, Benes V. FLT-PET in previously untreated patients with low-grade glioma can predict their overall survival. Nucl Med Rev Cent East Eur **2014**;17(1):7-12 doi 10.5603/NMR.2014.0003.

38. Challapalli A, Barwick T, Pearson RA, Merchant S, Mauri F, Howell EC, *et al.* 3'-Deoxy-3'-^{18}F-fluorothymidine positron emission tomography as an early predictor of disease progression in patients with advanced and metastatic pancreatic cancer. Eur J Nucl Med Mol Imaging **2015**;42(6):831-40 doi 10.1007/s00259-015-3000-2.

39. Inubushi M, Saga T, Koizumi M, Takagi R, Hasegawa A, Koto M, *et al.* Predictive value of 3'-deoxy-3'-[18F]fluorothymidine positron emission tomography/computed tomography for outcome of carbon ion radiotherapy in patients with head and neck mucosal malignant melanoma. Ann Nucl Med **2013**;27(1):1-10 doi 10.1007/s12149-012-0652-x.

40. Muzi M, Vesselle H, Grierson JR, Mankoff DA, Schmidt RA, Peterson L, *et al.* Kinetic analysis of 3'-deoxy-3'-fluorothymidine PET studies: validation studies in patients with lung cancer. J Nucl Med **2005**;46(2):274-82.

41. Muzi M, Mankoff DA, Grierson JR, Wells JM, Vesselle H, Krohn KA. Kinetic modeling of 3'-deoxy-3'-fluorothymidine in somatic tumors: mathematical studies. J Nucl Med **2005**;46(2):371-80.

42. Hanahan D, Weinberg RA. Hallmarks of cancer: the next generation. Cell **2011**;144(5):646-74 doi 10.1016/j.cell.2011.02.013.

43. Hughes WL, Bond VP, Brecher G, Cronkite EP, Painter RB, Quastler H, *et al.* CELLULAR PROLIFERATION IN THE MOUSE AS REVEALED BY AUTORADIOGRAPHY WITH TRITIATED THYMIDINE. Proc Natl Acad Sci U S A **1958**;44(5):476-83.

44. Gerdes J, Schwab U, Lemke H, Stein H. Production of a mouse monoclonal antibody reactive with a human nuclear antigen associated with cell proliferation. Int J Cancer **1983**;31(1):13-20.

45. Li LT, Jiang G, Chen Q, Zheng JN. Ki67 is a promising molecular target in the diagnosis of cancer (review). Mol Med Rep **2015**;11(3):1566-72 doi 10.3892/mmr.2014.2914.

46. Martiat P, Ferrant A, Labar D, Cogneau M, Bol A, Michel C, *et al.* In vivo measurement of carbon-11 thymidine uptake in non-Hodgkin's lymphoma using positron emission tomography. J Nucl Med **1988**;29(10):1633-7.

47. Kong XB, Zhu QY, Vidal PM, Watanabe KA, Polsky B, Armstrong D, *et al.* Comparisons of anti-human immunodeficiency virus activities, cellular transport, and plasma and intracellular pharmacokinetics of 3'-fluoro-3'-deoxythymidine and 3'-azido-3'-deoxythymidine. Antimicrob Agents Chemother **1992**;36(4):808-18.

48. Brockenbrough JS, Souquet T, Morihara JK, Stern JE, Hawes SE, Rasey JS, *et al.* Tumor 3'-deoxy-3'-(18)F-fluorothymidine ((18)F-FLT) uptake by PET correlates with thymidine

kinase 1 expression: static and kinetic analysis of (18)F-FLT PET studies in lung tumors. J Nucl Med **2011**;52(8):1181-8 doi 10.2967/jnumed.111.089482.

49. Backes H, Ullrich R, Neumaier B, Kracht L, Wienhard K, Jacobs AH. Noninvasive quantification of 18F-FLT human brain PET for the assessment of tumour proliferation in patients with high-grade glioma. Eur J Nucl Med Mol Imaging **2009**;36(12):1960-7 doi 10.1007/s00259-009-1244-4.

50. Kenny LM, Vigushin DM, Al-Nahhas A, Osman S, Luthra SK, Shousha S, *et al.* Quantification of cellular proliferation in tumor and normal tissues of patients with breast cancer by [18F]fluorothymidine-positron emission tomography imaging: evaluation of analytical methods. Cancer Res **2005**;65(21):10104-12 doi 10.1158/0008-5472.CAN-04-4297.

51. Chalkidou A, Landau DB, Odell EW, Cornelius VR, O'Doherty MJ, Marsden PK. Correlation between Ki-67 immunohistochemistry and 18F-fluorothymidine uptake in patients with cancer: A systematic review and meta-analysis. Eur J Cancer **2012**;48(18):3499-513 doi 10.1016/j.ejca.2012.05.001.

52. Yang W, Zhang Y, Fu Z, Sun X, Mu D, Yu J. Imaging proliferation of ^{18}F-FLT PET/CT correlated with the expression of microvessel density of tumour tissue in non-small-cell lung cancer. Eur J Nucl Med Mol Imaging **2012**;39(8):1289-96 doi 10.1007/s00259-012-2126-8.

53. Thie JA, Hubner KF, Smith GT. The diagnostic utility of the lognormal behavior of PET standardized uptake values in tumors. J Nucl Med **2000**;41(10):1664-72.

54. Willaime JM, Turkheimer FE, Kenny LM, Aboagye EO. Quantification of intra-tumour cell proliferation heterogeneity using imaging descriptors of 18F fluorothymidine-positron emission tomography. Phys Med Biol **2013**;58(2):187-203 doi 10.1088/0031-9155/58/2/187.

55. Hatt M, Cheze-Le Rest C, Aboagye EO, Kenny LM, Rosso L, Turkheimer FE, *et al.* Reproducibility of 18F-FDG and 3'-deoxy-3'-18F-fluorothymidine PET tumor volume measurements. J Nucl Med **2010**;51(9):1368-76 doi 10.2967/jnumed.110.078501.

56. Trigonis I, Koh PK, Taylor B, Tamal M, Ryder D, Earl M, *et al.* Early reduction in tumour [18F]fluorothymidine (FLT) uptake in patients with non-small cell lung cancer (NSCLC) treated with radiotherapy alone. Eur J Nucl Med Mol Imaging **2014**;41(4):682-93 doi 10.1007/s00259-013-2632-3.

57. Frings V, de Langen AJ, Smit EF, van Velden FH, Hoekstra OS, van Tinteren H, *et al.* Repeatability of metabolically active volume measurements with 18F-FDG and 18F-FLT PET in non-small cell lung cancer. J Nucl Med **2010**;51(12):1870-7 doi 10.2967/jnumed.110.077255.

58. de Langen AJ, Klabbers B, Lubberink M, Boellaard R, Spreeuwenberg MD, Slotman BJ, *et al.* Reproducibility of quantitative 18F-3'-deoxy-3'-fluorothymidine measurements using positron emission tomography. Eur J Nucl Med Mol Imaging **2009**;36(3):389-95 doi 10.1007/s00259-008-0960-5.

59. Lodge MA, Holdhoff M, Leal JP, Bag AK, Nabors LB, Mintz A, *et al.* Repeatability of. J Nucl Med **2017**;58(3):393-8 doi 10.2967/jnumed.116.178434.

60. Cysouw MCF, Kramer GM, Frings V, De Langen AJ, Wondergem MJ, Kenny LM, *et al.* Baseline and longitudinal variability of normal tissue uptake values of [Nucl Med Biol **2017**;51:18-24 doi 10.1016/j.nucmedbio.2017.05.002.

61. Kramer GM, Liu Y, de Langen AJ, Jansma EP, Trigonis I, Asselin MC, *et al.* Repeatability of quantitative. Eur J Nucl Med Mol Imaging **2018**;45(6):951-61 doi 10.1007/s00259-017-3923-x.

62. Berg E, Cherry SR. Innovations in Instrumentation for Positron Emission Tomography. Semin Nucl Med **2018**;48(4):311-31 doi 10.1053/j.semnuclmed.2018.02.006.

63. Simoncic U, Jeraj R. Cumulative input function method for linear compartmental models and spectral analysis in PET. J Cereb Blood Flow Metab **2011**;31(2):750-6 doi 10.1038/jcbfm.2010.159.

64. Simoncic U, Jeraj R. Heterogeneity in stabilization phenomena in FLT PET images of canines. Phys Med Biol **2014**;59(24):7937-55 doi 10.1088/0031-9155/59/24/7937.

65. Wagner M, Seitz U, Buck A, Neumaier B, Schultheiss S, Bangerter M, *et al.* 3'-[18F]fluoro-3'-deoxythymidine ([18F]-FLT) as positron emission tomography tracer for imaging proliferation in a murine B-Cell lymphoma model and in the human disease. Cancer Res **2003**;63(10):2681-7.

66. Shields AF, Briston DA, Chandupatla S, Douglas KA, Lawhorn-Crews J, Collins JM, *et al.* A simplified analysis of [18F]3'-deoxy-3'-fluorothymidine metabolism and retention. Eur J Nucl Med Mol Imaging **2005**;32(11):1269-75 doi 10.1007/s00259-005-1813-0.

67. Visvikis D, Francis D, Mulligan R, Costa DC, Croasdale I, Luthra SK, *et al.* Comparison of methodologies for the in vivo assessment of 18FLT utilisation in colorectal cancer. Eur J Nucl Med Mol Imaging **2004**;31(2):169-78 doi 10.1007/s00259-003-1339-2.

68. Simončič U, Zanotti-Fregonara P. Image-derived input function with factor analysis and a-priori information. Nucl Med Commun **2015**;36(2):187-93 doi 10.1097/MNM.0000000000000231.

69. de Geus-Oei LF, Visser EP, Krabbe PF, van Hoorn BA, Koenders EB, Willemsen AT, *et al.* Comparison of image-derived and arterial input functions for estimating the rate of glucose metabolism in therapy-monitoring 18F-FDG PET studies. J Nucl Med **2006**;47(6):945-9.

70. Mankoff DA, Shields AF, Graham MM, Link JM, Eary JF, Krohn KA. Kinetic analysis of 2-[carbon-11]thymidine PET imaging studies: compartmental model and mathematical analysis. J Nucl Med **1998**;39(6):1043-55.

71. Mankoff D, Muzi M, Zaidi H. Quantitative Analysis in Nuclear Oncologic Imaging In: Zaide H, editor. Quantitative Analysis in Nuclear Medicine Imaging. New York, NY: Springer; 2006. p 494-536.

72. Simoncic U. Modelling of radiopharmaceuticals uptake into the tumor - optimization of the method and its application in the clinical studies. Ljubljana Slovenia: University of Ljubljana; 2011. 113 p.

73. Kenny L, Coombes RC, Vigushin DM, Al-Nahhas A, Shousha S, Aboagye EO. Imaging early changes in proliferation at 1 week post chemotherapy: a pilot study in breast cancer

patients with 3'-deoxy-3'-[18F]fluorothymidine positron emission tomography. Eur J Nucl Med Mol Imaging **2007**;34(9):1339-47 doi 10.1007/s00259-007-0379-4.

74. Burton P, Gurrin L, Sly P. Extending the Simple Linear Regression Model to Account for Correlated Responses: An Introduction to Generalized Estimating Equations and Multi-Level Mixed Modelling. Statistics in Medicine **1998**;17:1261-91.

75. Altman DG, Bland JM. Parametric v non-parametric methods for data analysis. BMJ **2009**;338:a3167.

76. Bland JM, Altman DG. Transforming data. BMJ **1996**;312(7033):770.

77. Schwartz DL, Harris J, Yao M, Rosenthal DI, Opanowski A, Levering A, *et al.* Metabolic tumor volume as a prognostic imaging-based biomarker for head-and-neck cancer: pilot results from Radiation Therapy Oncology Group protocol 0522. Int J Radiat Oncol Biol Phys **2015**;91(4):721-9 doi 10.1016/j.ijrobp.2014.12.023.

78. Box G, Cox D. An Analysis of Transformations. Journal of the Royal Statistical Society Series B **1964**;26:211-52.

79. Shapiro S, Wilk M. An Analysis of Variance Test for Normality (Complete Samples). Biometrika **1965**;52:591-611.

80. Efron B. Better Bootstrap Confidence Intervals Journal of the American Statistical Association **1987**;82:171-85.

81. Wilk MB, Gnanadesikan R. Probability plotting methods for the analysis of data. Biometrika **1968**;55(1):1-17.

82. Filliben J. The Probability Plot Correlation Coefficient Test for Normality. Technometrics **1975**;17(1):111-7.

83. Fahey FH, Kinahan PE, Doot RK, Kocak M, Thurston H, Poussaint TY. Variability in PET quantitation within a multicenter consortium. Med Phys **2010**;37(7):3660-6 doi 10.1118/1.3455705.

84. Binns DS, Pirzkall A, Yu W, Callahan J, Mileshkin L, Conti P, *et al.* Compliance with PET acquisition protocols for therapeutic monitoring of erlotinib therapy in an international trial for patients with non-small cell lung cancer. Eur J Nucl Med Mol Imaging **2011**;38(4):642-50 doi 10.1007/s00259-010-1665-0.

85. Bruce JY, Scully PC, Carmichael LL, Eickhoff JC, Perlman SB, Kolesar JM, *et al.* Pharmacodynamic study of axitinib in patients with advanced malignancies assessed with (18)F-3'deoxy-3'fluoro-L-thymidine positron emission tomography/computed tomography. Cancer Chemother Pharmacol **2015**;76(1):187-95 doi 10.1007/s00280-015-2779-7.

86. Folkman J. Tumor angiogenesis: therapeutic implications. N Engl J Med **1971**;285(21):1182-6 doi 10.1056/NEJM197111182852108.

87. Emmett MS, Dewing D, Pritchard-Jones RO. Angiogenesis and melanoma - from basic science to clinical trials. Am J Cancer Res **2011**;1(7):852-68.

88. Folkman J. Endogenous angiogenesis inhibitors. APMIS **2004**;112(7-8):496-507 doi 10.1111/j.1600-0463.2004.apm11207-0809.x.

89. Cunningham D, Lang I, Marcuello E, Lorusso V, Ocvirk J, Shin DB, *et al.* Bevacizumab plus capecitabine versus capecitabine alone in elderly patients with previously untreated metastatic colorectal cancer (AVEX): an open-label, randomised phase 3 trial. Lancet Oncol **2013**;14(11):1077-85 doi 10.1016/S1470-2045(13)70154-2.

90. Reck M, von Pawel J, Zatloukal P, Ramlau R, Gorbounova V, Hirsh V, *et al.* Phase III trial of cisplatin plus gemcitabine with either placebo or bevacizumab as first-line therapy for nonsquamous non-small-cell lung cancer: AVAil. J Clin Oncol **2009**;27(8):1227-34 doi 10.1200/JCO.2007.14.5466.

91. Escudier B, Eisen T, Stadler WM, Szczylik C, Oudard S, Staehler M, *et al.* Sorafenib for treatment of renal cell carcinoma: Final efficacy and safety results of the phase III treatment approaches in renal cancer global evaluation trial. J Clin Oncol **2009**;27(20):3312-8 doi 10.1200/JCO.2008.19.5511.

92. Motzer RJ, Hutson TE, Tomczak P, Michaelson MD, Bukowski RM, Oudard S, *et al.* Overall survival and updated results for sunitinib compared with interferon alfa in patients with metastatic renal cell carcinoma. J Clin Oncol **2009**;27(22):3584-90 doi 10.1200/JCO.2008.20.1293.

93. Rini BI, Escudier B, Tomczak P, Kaprin A, Szczylik C, Hutson TE, *et al.* Comparative effectiveness of axitinib versus sorafenib in advanced renal cell carcinoma (AXIS): a randomised phase 3 trial. Lancet **2011**;378(9807):1931-9 doi 10.1016/S0140-6736(11)61613-9.

94. Raymond E, Dahan L, Raoul JL, Bang YJ, Borbath I, Lombard-Bohas C, *et al.* Sunitinib malate for the treatment of pancreatic neuroendocrine tumors. N Engl J Med **2011**;364(6):501-13 doi 10.1056/NEJMoa1003825.

95. Llovet JM, Ricci S, Mazzaferro V, Hilgard P, Gane E, Blanc JF, *et al.* Sorafenib in advanced hepatocellular carcinoma. N Engl J Med **2008**;359(4):378-90 doi 10.1056/NEJMoa0708857.

96. Bergers G, Hanahan D. Modes of resistance to anti-angiogenic therapy. Nat Rev Cancer **2008**;8(8):592-603 doi 10.1038/nrc2442.

97. Scagliotti G, Novello S, von Pawel J, Reck M, Pereira JR, Thomas M, *et al.* Phase III study of carboplatin and paclitaxel alone or with sorafenib in advanced non-small-cell lung cancer. J Clin Oncol **2010**;28(11):1835-42 doi 10.1200/JCO.2009.26.1321.

98. Kindler HL, Ioka T, Richel DJ, Bennouna J, Létourneau R, Okusaka T, *et al.* Axitinib plus gemcitabine versus placebo plus gemcitabine in patients with advanced pancreatic adenocarcinoma: a double-blind randomised phase 3 study. Lancet Oncol **2011**;12(3):256-62 doi 10.1016/S1470-2045(11)70004-3.

99. Hauschild A, Agarwala SS, Trefzer U, Hogg D, Robert C, Hersey P, *et al.* Results of a phase III, randomized, placebo-controlled study of sorafenib in combination with carboplatin and paclitaxel as second-line treatment in patients with unresectable stage III or stage IV melanoma. J Clin Oncol **2009**;27(17):2823-30 doi 10.1200/JCO.2007.15.7636.

100. Hecht JR, Trarbach T, Hainsworth JD, Major P, Jäger E, Wolff RA, *et al.* Randomized, placebo-controlled, phase III study of first-line oxaliplatin-based chemotherapy plus

PTK787/ZK 222584, an oral vascular endothelial growth factor receptor inhibitor, in patients with metastatic colorectal adenocarcinoma. J Clin Oncol **2011**;29(15):1997-2003 doi 10.1200/JCO.2010.29.4496.

101. Crown JP, Diéras V, Staroslawska E, Yardley DA, Bachelot T, Davidson N, *et al.* Phase III trial of sunitinib in combination with capecitabine versus capecitabine monotherapy for the treatment of patients with pretreated metastatic breast cancer. J Clin Oncol **2013**;31(23):2870-8 doi 10.1200/JCO.2012.43.3391.

102. Rugo HS, Stopeck AT, Joy AA, Chan S, Verma S, Lluch A, *et al.* Randomized, placebo-controlled, double-blind, phase II study of axitinib plus docetaxel versus docetaxel plus placebo in patients with metastatic breast cancer. J Clin Oncol **2011**;29(18):2459-65 doi 10.1200/JCO.2010.31.2975.

103. Wardak M, Schiepers C, Dahlbom M, Cloughesy T, Chen W, Satyamurthy N, *et al.* Discriminant analysis of ^{18}F-fluorothymidine kinetic parameters to predict survival in patients with recurrent high-grade glioma. Clin Cancer Res **2011**;17(20):6553-62 doi 10.1158/1078-0432.CCR-10-3290.

104. Schiepers C, Dahlbom M, Chen W, Cloughesy T, Czernin J, Phelps ME, *et al.* Kinetics of 3'-deoxy-3'-18F-fluorothymidine during treatment monitoring of recurrent high-grade glioma. J Nucl Med **2010**;51(5):720-7 doi 10.2967/jnumed.109.068361.

105. Hoh CK, Burris HA, Bendell JC, Tarazi J, Rosbrook B, Kim S, *et al.* Intermittent dosing of axitinib combined with chemotherapy is supported by (18)FLT-PET in gastrointestinal tumours. Br J Cancer **2014**;110(4):875-81 doi 10.1038/bjc.2013.806.

106. Horn KP, Yap JT, Agarwal N, Morton KA, Kadrmas DJ, Beardmore B, *et al.* FDG and FLT-PET for Early measurement of response to 37.5 mg daily sunitinib therapy in metastatic renal cell carcinoma. Cancer Imaging **2015**;15:15 doi 10.1186/s40644-015-0049-x.

107. Sonpavde G, Hutson TE, Rini BI. Axitinib for renal cell carcinoma. Expert Opin Investig Drugs **2008**;17(5):741-8 doi 10.1517/13543784.17.5.741.

108. Rini BI, Garrett M, Poland B, Dutcher JP, Rixe O, Wilding G, *et al.* Axitinib in metastatic renal cell carcinoma: results of a pharmacokinetic and pharmacodynamic analysis. J Clin Pharmacol **2013**;53(5):491-504 doi 10.1002/jcph.73.

109. Liu G, Rugo HS, Wilding G, McShane TM, Evelhoch JL, Ng C, *et al.* Dynamic contrast-enhanced magnetic resonance imaging as a pharmacodynamic measure of response after acute dosing of AG-013736, an oral angiogenesis inhibitor, in patients with advanced solid tumors: results from a phase I study. J Clin Oncol **2005**;23(24):5464-73 doi 10.1200/JCO.2005.04.143.

110. Lo GM, Al Zahrani H, Jang HJ, Menezes R, Hudson J, Burns P, *et al.* Detection of Early Tumor Response to Axitinib in Advanced Hepatocellular Carcinoma by Dynamic Contrast Enhanced Ultrasound. Ultrasound Med Biol **2016**;42(6):1303-11 doi 10.1016/j.ultrasmedbio.2016.01.025.

111. Goldman D, Bowen D, Gewirtz DA. Some considerations in the experimental approach to distinguishing between membrane transport and intracellular disposition of

antineoplastic agents, with specific reference to fluorodeoxyuridine, actinomycin D, and methotrexate. Cancer Treat Rep **1981**;65 Suppl 3:43-56.

112. Rössler J, Monnet Y, Farace F, Opolon P, Daudigeos-Dubus E, Bourredjem A, *et al.* The selective VEGFR1-3 inhibitor axitinib (AG-013736) shows antitumor activity in human neuroblastoma xenografts. Int J Cancer **2011**;128(11):2748-58 doi 10.1002/ijc.25611.

113. Zhang L, Smith KM, Chong AL, Stempak D, Yeger H, Marrano P, *et al.* In vivo antitumor and antimetastatic activity of sunitinib in preclinical neuroblastoma mouse model. Neoplasia **2009**;11(5):426-35.

114. Chen Y, Tortorici MA, Garrett M, Hee B, Klamerus KJ, Pithavala YK. Clinical pharmacology of axitinib. Clin Pharmacokinet **2013**;52(9):713-25 doi 10.1007/s40262-013-0068-3.

115. Mancuso MR, Davis R, Norberg SM, O'Brien S, Sennino B, Nakahara T, *et al.* Rapid vascular regrowth in tumors after reversal of VEGF inhibition. J Clin Invest **2006**;116(10):2610-21 doi 10.1172/JCI24612.

116. Griffioen AW, Mans LA, de Graaf AM, Nowak-Sliwinska P, de Hoog CL, de Jong TA, *et al.* Rapid angiogenesis onset after discontinuation of sunitinib treatment of renal cell carcinoma patients. Clin Cancer Res **2012**;18(14):3961-71 doi 10.1158/1078-0432.CCR-12-0002.

117. Britten CD, Kabbinavar F, Hecht JR, Bello CL, Li J, Baum C, *et al.* A phase I and pharmacokinetic study of sunitinib administered daily for 2 weeks, followed by a 1-week off period. Cancer Chemother Pharmacol **2008**;61(3):515-24 doi 10.1007/s00280-007-0498-4.

118. Reck M, Kaiser R, Mellemgaard A, Douillard JY, Orlov S, Krzakowski M, *et al.* Docetaxel plus nintedanib versus docetaxel plus placebo in patients with previously treated non-small-cell lung cancer (LUME-Lung 1): a phase 3, double-blind, randomised controlled trial. Lancet Oncol **2014**;15(2):143-55 doi 10.1016/S1470-2045(13)70586-2.

119. Contractor KB, Kenny LM, Stebbing J, Rosso L, Ahmad R, Jacob J, *et al.* [18F]-3'Deoxy-3'-fluorothymidine positron emission tomography and breast cancer response to docetaxel. Clin Cancer Res **2011**;17(24):7664-72 doi 10.1158/1078-0432.CCR-11-0783.

120. Tan B, Picus J, Chan E, Lockhart A, Roth B, Morton A, *et al.* Phase I study of X-82, an oral dual anti-VEGFR/PDGFR tyrosine kinase inhibitor, with everolimus in solid tumors. 2016; Chicago, Illinois.

121. Hodi FS, O'Day SJ, McDermott DF, Weber RW, Sosman JA, Haanen JB, *et al.* Improved survival with ipilimumab in patients with metastatic melanoma. N Engl J Med **2010**;363(8):711-23 doi 10.1056/NEJMoa1003466.

122. Hamid O, Robert C, Daud A, Hodi FS, Hwu WJ, Kefford R, *et al.* Safety and tumor responses with lambrolizumab (anti-PD-1) in melanoma. N Engl J Med **2013**;369(2):134-44 doi 10.1056/NEJMoa1305133.

123. Wolchok JD, Kluger H, Callahan MK, Postow MA, Rizvi NA, Lesokhin AM, *et al.* Nivolumab plus ipilimumab in advanced melanoma. N Engl J Med **2013**;369(2):122-33 doi 10.1056/NEJMoa1302369.

124. Sun C, Mezzadra R, Schumacher TN. Regulation and Function of the PD-L1 Checkpoint. Immunity **2018**;48(3):434-52 doi 10.1016/j.immuni.2018.03.014.

125. Brahmer JR, Drake CG, Wollner I, Powderly JD, Picus J, Sharfman WH, *et al.* Phase I study of single-agent anti-programmed death-1 (MDX-1106) in refractory solid tumors: safety, clinical activity, pharmacodynamics, and immunologic correlates. J Clin Oncol **2010**;28(19):3167-75 doi 10.1200/JCO.2009.26.7609.

126. Topalian SL, Hodi FS, Brahmer JR, Gettinger SN, Smith DC, McDermott DF, *et al.* Safety, activity, and immune correlates of anti-PD-1 antibody in cancer. N Engl J Med **2012**;366(26):2443-54 doi 10.1056/NEJMoa1200690.

127. McNeel DG, Eickhoff JC, Wargowski E, Zahm C, Staab MJ, Straus J, *et al.* Concurrent, but not sequential, PD-1 blockade with a DNA vaccine elicits anti-tumor responses in patients with metastatic, castration-resistant prostate cancer. Oncotarget **2018**;9(39):25586-96 doi 10.18632/oncotarget.25387.

128. Postow MA, Sidlow R, Hellmann MD. Immune-Related Adverse Events Associated with Immune Checkpoint Blockade. N Engl J Med **2018**;378(2):158-68 doi 10.1056/NEJMra1703481.

129. Michot JM, Bigenwald C, Champiat S, Collins M, Carbonnel F, Postel-Vinay S, *et al.* Immune-related adverse events with immune checkpoint blockade: a comprehensive review. Eur J Cancer **2016**;54:139-48 doi 10.1016/j.ejca.2015.11.016.

130. Yuan J, Hegde PS, Clynes R, Foukas PG, Harari A, Kleen TO, *et al.* Novel technologies and emerging biomarkers for personalized cancer immunotherapy. J Immunother Cancer **2016**;4:3 doi 10.1186/s40425-016-0107-3.

131. Gainor JF, Longo DL, Chabner BA. Pharmacodynamic biomarkers: falling short of the mark? Clin Cancer Res **2014**;20(10):2587-94 doi 10.1158/1078-0432.CCR-13-3132.

132. Ribas A, Benz MR, Allen-Auerbach MS, Radu C, Chmielowski B, Seja E, *et al.* Imaging of CTLA4 blockade-induced cell replication with (18)F-FLT PET in patients with advanced melanoma treated with tremelimumab. J Nucl Med **2010**;51(3):340-6 doi 10.2967/jnumed.109.070946.

133. Aarntzen EH, Srinivas M, De Wilt JH, Jacobs JF, Lesterhuis WJ, Windhorst AD, *et al.* Early identification of antigen-specific immune responses in vivo by [18F]-labeled 3'-fluoro-3'-deoxy-thymidine ([18F]FLT) PET imaging. Proc Natl Acad Sci U S A **2011**;108(45):18396-9 doi 10.1073/pnas.1113045108.

134. Scher HI, Halabi S, Tannock I, Morris M, Sternberg CN, Carducci MA, *et al.* Design and end points of clinical trials for patients with progressive prostate cancer and castrate levels of testosterone: recommendations of the Prostate Cancer Clinical Trials Working Group. J Clin Oncol **2008**;26(7):1148-59 doi 10.1200/JCO.2007.12.4487.

135. Schröder MS, Culhane AC, Quackenbush J, Haibe-Kains B. survcomp: an R/Bioconductor package for performance assessment and comparison of survival models. Bioinformatics **2011**;27(22):3206-8 doi 10.1093/bioinformatics/btr511.

136. Pencina MJ, D'Agostino RB. Overall C as a measure of discrimination in survival analysis: model specific population value and confidence interval estimation. Stat Med **2004**;23(13):2109-23 doi 10.1002/sim.1802.

137. Robin X, Turck N, Hainard A, Tiberti N, Lisacek F, Sanchez JC, *et al.* pROC: an open-source package for R and S+ to analyze and compare ROC curves. BMC Bioinformatics **2011**;12:77 doi 10.1186/1471-2105-12-77.

138. Osorio JC, Ni A, Chaft JE, Pollina R, Kasler MK, Stephens D, *et al.* Antibody-mediated thyroid dysfunction during T-cell checkpoint blockade in patients with non-small-cell lung cancer. Ann Oncol **2017**;28(3):583-9 doi 10.1093/annonc/mdw640.

139. Becker JT, Olson BM, Johnson LE, Davies JG, Dunphy EJ, McNeel DG. DNA vaccine encoding prostatic acid phosphatase (PAP) elicits long-term T-cell responses in patients with recurrent prostate cancer. J Immunother **2010**;33(6):639-47 doi 10.1097/CJI.0b013e3181dda23e.

140. Wu C, Li F, Niu G, Chen X. PET imaging of inflammation biomarkers. Theranostics **2013**;3(7):448-66 doi 10.7150/thno.6592.

141. Been LB, Suurmeijer AJ, Cobben DC, Jager PL, Hoekstra HJ, Elsinga PH. [18F]FLT-PET in oncology: current status and opportunities. Eur J Nucl Med Mol Imaging **2004**;31(12):1659-72 doi 10.1007/s00259-004-1687-6.

142. Buck AK, Halter G, Schirrmeister H, Kotzerke J, Wurziger I, Glatting G, *et al.* Imaging proliferation in lung tumors with PET: 18F-FLT versus 18F-FDG. J Nucl Med **2003**;44(9):1426-31.

143. Frampton JE. Mifamurtide: a review of its use in the treatment of osteosarcoma. Paediatr Drugs **2010**;12(3):141-53 doi 10.2165/11204910-000000000-00000.

144. Ando K, Mori K, Corradini N, Redini F, Heymann D. Mifamurtide for the treatment of nonmetastatic osteosarcoma. Expert Opin Pharmacother **2011**;12(2):285-92 doi 10.1517/14656566.2011.543129.

145. Kong BY, Menzies AM, Saunders CA, Liniker E, Ramanujam S, Guminski A, *et al.* Residual FDG-PET metabolic activity in metastatic melanoma patients with prolonged response to anti-PD-1 therapy. Pigment Cell Melanoma Res **2016**;29(5):572-7 doi 10.1111/pcmr.12503.

146. Shi C, Jia T, Mendez-Ferrer S, Hohl TM, Serbina NV, Lipuma L, *et al.* Bone marrow mesenchymal stem and progenitor cells induce monocyte emigration in response to circulating toll-like receptor ligands. Immunity **2011**;34(4):590-601 doi 10.1016/j.immuni.2011.02.016.

147. Shi C, Pamer EG. Monocyte recruitment during infection and inflammation. Nat Rev Immunol **2011**;11(11):762-74 doi 10.1038/nri3070.

148. Scarpelli M, Simoncic U, Perlman S, Liu G, Jeraj R. Dynamic ^{18}F-FLT PET imaging of spatiotemporal changes in tumor cell proliferation and vasculature reveals the mechanistic actions of anti-angiogenic therapy. Phys Med Biol **2018**;63(15):155008 doi 10.1088/1361-6560/aad1be.

149. Scarpelli M, Eickhoff J, Cuna E, Perlman S, Jeraj R. Optimal transformations leading to normal distributions of positron emission tomography standardized uptake values. Phys Med Biol **2018**;63(3):035021 doi 10.1088/1361-6560/aaa175.

150. Heist RS, Duda DG, Sahani DV, Ancukiewicz M, Fidias P, Sequist LV, *et al.* Improved tumor vascularization after anti-VEGF therapy with carboplatin and nab-paclitaxel associates with survival in lung cancer. Proc Natl Acad Sci U S A **2015**;112(5):1547-52 doi 10.1073/pnas.1424024112.

151. Scarpelli M, Bruce JY, Carmichael L, Eickhoff J, Kolesar J, Perlman S, *et al.* (18)F-FLT PET/CT imaging in patients with advanced solid malignancies treated with axitinib on an intermittent dosing regimen. Cancer Chemother Pharmacol **2016**;78(6):1245-52 doi 10.1007/s00280-016-3183-7.

152. Scarpelli M, Rampurwala M, Eickhoff J, Carmichael L, Heideman J, Binger K, *et al.* Pharmacodynamic study using FLT PET/CT in advanced solid malignancies treated with a sequential combination of X-82 and docetaxel. Cancer Chemotherapy and Pharmacology **2018** doi 10.1007/s00280-018-3599-3.

153. Smith NR, Baker D, James NH, Ratcliffe K, Jenkins M, Ashton SE, *et al.* Vascular endothelial growth factor receptors VEGFR-2 and VEGFR-3 are localized primarily to the vasculature in human primary solid cancers. Clin Cancer Res **2010**;16(14):3548-61 doi 10.1158/1078-0432.CCR-09-2797.

154. Rovithi M, Verheul HMW. Pulsatile high-dose treatment with antiangiogenic tyrosine kinase inhibitors improves clinical antitumor activity. Angiogenesis **2017**;20(3):287-9 doi 10.1007/s10456-017-9555-8.

155. Barbee MS, Ogunniyi A, Horvat TZ, Dang TO. Current status and future directions of the immune checkpoint inhibitors ipilimumab, pembrolizumab, and nivolumab in oncology. Ann Pharmacother **2015**;49(8):907-37 doi 10.1177/1060028015586218.

156. Christian BT, Vandehey NT, Floberg JM, Mistretta CA. Dynamic PET denoising with HYPR processing. J Nucl Med **2010**;51(7):1147-54 doi 10.2967/jnumed.109.073999.

157. Wang G, Qi J. Direct estimation of kinetic parametric images for dynamic PET. Theranostics **2013**;3(10):802-15 doi 10.7150/thno.5130.

158. Hara T, Kobayashi T, Ito S, Zhou X, Katafuchi T, Fujita H. Quantitative Analysis of Torso FDG-PET Scans by Using Anatomical Standardization of Normal Cases from Thorough Physical Examinations. PLOS ONE **2015**;10(5):e0125713 doi 10.1371/journal.pone.0125713.

159. Fluss R, Faraggi D, Reiser B. Estimation of the Youden Index and its associated cutoff point. Biom J **2005**;47(4):458-72.

160. Schisterman E, Perkins N. Confidence Intervals for the Youden Index and Corresponding Optimal Cut-Point. Communications in Statistics - Simulation and Computation **2007**;36:549-63.

161. Jauw YWS, Huisman MC, Nayak TK, Vugts DJ, Christen R, Naegelen VM, *et al.* Assessment of target-mediated uptake with immuno-PET: analysis of a phase I clinical

trial with an anti-CD44 antibody. EJNMMI Res **2018**;8(1):6 doi 10.1186/s13550-018-0358-8.

162. Ordonez AA, Jain SK. Pathogen-Specific Bacterial Imaging in Nuclear Medicine. Semin Nucl Med **2018**;48(2):182-94 doi 10.1053/j.semnuclmed.2017.11.003.

163. Keu KV, Witney TH, Yaghoubi S, Rosenberg J, Kurien A, Magnusson R, *et al.* Reporter gene imaging of targeted T cell immunotherapy in recurrent glioma. Sci Transl Med **2017**;9(373) doi 10.1126/scitranslmed.aag2196.

164. Higashikawa K, Yagi K, Watanabe K, Kamino S, Ueda M, Hiromura M, *et al.* 64Cu-DOTA-anti-CTLA-4 mAb enabled PET visualization of CTLA-4 on the T-cell infiltrating tumor tissues. PLoS One **2014**;9(11):e109866 doi 10.1371/journal.pone.0109866.

165. Ehlerding EB, England CG, Majewski RL, Valdovinos HF, Jiang D, Liu G, *et al.* ImmunoPET Imaging of CTLA-4 Expression in Mouse Models of Non-small Cell Lung Cancer. Mol Pharm **2017**;14(5):1782-9 doi 10.1021/acs.molpharmaceut.7b00056.

166. Hettich M, Braun F, Bartholomä MD, Schirmbeck R, Niedermann G. High-Resolution PET Imaging with Therapeutic Antibody-based PD-1/PD-L1 Checkpoint Tracers. Theranostics **2016**;6(10):1629-40 doi 10.7150/thno.15253.

167. Larimer BM, Wehrenberg-Klee E, Caraballo A, Mahmood U. Quantitative CD3 PET Imaging Predicts Tumor Growth Response to Anti-CTLA-4 Therapy. J Nucl Med **2016**;57(10):1607-11 doi 10.2967/jnumed.116.173930.

168. Tavaré R, Escuin-Ordinas H, Mok S, McCracken MN, Zettlitz KA, Salazar FB, *et al.* An Effective Immuno-PET Imaging Method to Monitor CD8-Dependent Responses to Immunotherapy. Cancer Res **2016**;76(1):73-82 doi 10.1158/0008-5472.CAN-15-1707.